

**Seismic imaging based on Joint Migration Inversion
Handling missing low frequencies and horizontally propagating waves**

Masaya, Shogo

DOI

[10.4233/uuid:4b348428-50dc-4594-90f0-fc1bf90661a2](https://doi.org/10.4233/uuid:4b348428-50dc-4594-90f0-fc1bf90661a2)

Publication date

2018

Document Version

Final published version

Citation (APA)

Masaya, S. (2018). *Seismic imaging based on Joint Migration Inversion: Handling missing low frequencies and horizontally propagating waves*. [Dissertation (TU Delft), Delft University of Technology].
<https://doi.org/10.4233/uuid:4b348428-50dc-4594-90f0-fc1bf90661a2>

Important note

To cite this publication, please use the final published version (if applicable).
Please check the document version above.

Copyright

Other than for strictly personal use, it is not permitted to download, forward or distribute the text or part of it, without the consent of the author(s) and/or copyright holder(s), unless the work is under an open content license such as Creative Commons.

Takedown policy

Please contact us and provide details if you believe this document breaches copyrights.
We will remove access to the work immediately and investigate your claim.

Seismic imaging based on Joint Migration Inversion:

Handling missing low frequencies and horizontally
propagating waves

**Seismic imaging based on Joint Migration
Inversion: Handling missing low frequencies and
horizontally propagating waves**

PROEFSCHRIFT

ter verkrijging van de graad van doctor
aan de Technische Universiteit Delft,
op gezag van de Rector Magnificus Prof.dr.ir. T.H.J.J. van der Hagen,
voorzitter van het College voor Promoties,
in het openbaar te verdedigen
op donderdag 11 september 2018 om 10:00 uur

door

Shogo MASAYA

Master of Science in Fundamental Energy Science
Universiteit van Kioto, Japan
Geboren te Tokio, Japan

Dit proefschrift is goedgekeurd door de promotoren:

Dr. ir. D.J. Verschuur

en

Prof. dr. ir. N. de Jong

Samenstelling promotiecommissie:

Rector Magnificus, voorzitter

Dr. ir. D.J. Verschuur, promotor, Technische Universiteit Delft

Prof. dr. ir. N. de Jong, promotor, Technische Universiteit Delft

Onafhankelijke leden:

Prof. dr. ir. C.P.A. Wapenaar, Technische Universiteit Delft

Prof. dr. B. Rieger, Technische Universiteit Delft

Prof. dr. A. Curtis, The University of Edinburgh

Dr. K.W.A. van Dongen, Technische Universiteit Delft

Dr. ir. R.F. Hegge, Aramco Overseas Company B.V.

Copyright ©2018, by S. Masaya. All rights reserved. No part of this publication may be reproduced, stored in a retrieval system or transmitted in any form or by any means, electronic, mechanical, photocopying, recording or otherwise, without the prior written permission of the author.

Typesetting system: L^AT_EX.

Printed in The Netherlands by Gildeprint.

This thesis is dedicated to my parents.

Contents

1	Introduction	5
1.1	Seismic data analysis	5
1.2	Reflectivity estimation	7
1.2.1	Kirchhoff migration	7
1.2.2	One-way wave equation migration	8
1.2.3	Reverse time migration	8
1.2.4	Least-squares migration	9
1.3	Velocity estimation	10
1.3.1	Normal move-out velocity analysis	10
1.3.2	Migration velocity analysis	11
1.3.3	Full waveform inversion	11
1.4	Simultaneous reflectivity and velocity estimation	12
1.4.1	Migration-based traveltime formulation	12
1.4.2	Joint migration inversion	13
1.5	Challenges in seismic imaging	13
1.5.1	Low frequencies-dependent velocity estimation	13
1.5.2	Near-surface imaging	14
1.6	Thesis objectives	16
1.7	Thesis outline	17
2	Notations and review	21

2.1	Representations for reflection, transmission, and propagation	22
2.2	Joint migration inversion	25
3	Reflectivity-constrained JMI	29
3.1	Introduction	29
3.2	Algorithm	32
3.2.1	Reflectivity approximation based on velocity estimation	32
3.2.2	Objective function	34
3.2.3	Reflectivity and velocity updates	35
3.3	Numerical examples	37
3.3.1	Example 1: Lens-shaped model	37
3.3.2	Example 2: SEG/EAGE Salt model	43
3.4	Field data example	48
3.5	Discussion	53
3.5.1	Computational cost	53
3.5.2	Density variations	53
3.6	Conclusions	54
4	Land JMI without low frequency components	57
4.1	Introduction	57
4.2	Numerical examples	60
4.2.1	Example 1: Middle-East land model	60
4.2.2	Example 2: Two geobodies model	60
4.3	Surface amplitude correction via learning from synthetic models	63
4.3.1	Method	63
4.3.2	Numerical experiment	65
4.4	Field data example	70
4.4.1	Pre-processing including surface amplitude correction	70
4.4.2	Full wavefield migration	70
4.4.3	Reflectivity-constrained joint migration inversion	73
4.5	Discussion	77

4.5.1	Initial velocity dependency of velocity estimation for near-surface anomalies	77
4.5.2	Surface amplitude correction based on learning process	77
4.6	Conclusions	80
5	JMI including refracted/diving waves	81
5.1	Introduction	81
5.2	Omni-directional wavefield modeling	83
5.2.1	Omni-directional extension	83
5.2.2	Vertical and horizontal propagation in staggered grid	84
5.2.3	Angle wavefield decomposition	85
5.2.4	Amplitude scaling	89
5.2.5	Numerical examples	93
5.3	Omni-directional wavefield migration	98
5.3.1	Reflectivity update based on horizontal propagation	98
5.3.2	Numerical examples	100
5.4	Omni-directional joint migration inversion	105
5.4.1	Slowness update based on horizontal propagation	105
5.4.2	Velocity update based on horizontal reflectivity constraint	107
5.4.3	Numerical example	109
5.5	Discussion	112
5.5.1	Misfit function	112
5.5.2	Waves utilized for reflectivity and slowness update	114
5.5.3	Iteration strategy for horizontal propagation . . .	115
5.6	Conclusions	115
6	Conclusions and recommendations	117
6.1	Conclusions	117
6.2	Recommendations for further research	119
6.2.1	Reflectivity-constrained velocity estimation	119
6.2.2	JMI including more accurate physical phenomena	119
6.2.3	Machine learning	120
A	Reflectivity and velocity updates by JMI	121

A.1 Reflectivity update	121
A.2 Slowness update	123
Bibliography	127
Summary	141
Samenvatting	143
Acknowledgments	145
Curriculum Vitae	149

Introduction

1.1 Seismic data analysis

Nowadays, seismic data analysis is commonly utilized in several fields to estimate the image of the subsurface. A central step in this procedure is the process to obtain the image from seismic data, which is called seismic imaging (Fig. 1.1). In general the seismic method can employ two types of datasets: passive and active seismic wavefield measurements.

Passive seismic data is measured via receivers at the surface or in boreholes and indicates the seismic waves caused by natural earthquakes and the tremors induced by so-called hydraulic fracturing to enhance oil and gas recovery in hydrocarbon reservoirs via some permanent or long-term monitoring system. The passive seismic data have been analyzed to mainly investigate the mechanism of earthquakes and tremors, like the structure of faults and fractures for the purpose of disaster prevention and prediction.

On the other hand, active seismic data is directly acquired by using artificial acoustic sources such as airgun, dynamite, and vibroseis. The active seismic data method is commonly used in civil engineering and in the oil & gas industry (e.g. Sheriff and Geldart, 1995). In civil engineer-

ing, the used active seismic data is one of effective tools to investigate the structures of the subsurface, including the near surface and the influence on buildings. In the oil & gas industry, the analysis using active seismic data plays a key role in the exploration and production for hydrocarbons. For example, seismic data analysis can provide an image of the subsurface with a vertically/horizontally wide coverage with relatively high resolution for the subsurface compared to the analysis using other types of data such as well data, electromagnetic data, and gravity data etc. An example of such seismic image is shown in Fig 1.1. This means that seismic data analysis is usually a cost-effective approach, especially in marine exploration projects since the availability of well data is limited in the exploration stage. Moreover, seismic data is commonly used for reservoir characterization (e.g. Avseth et al., 2005) by employing so-called amplitude versus offset (AVO) analysis, especially in the production stage.

This thesis focuses on the seismic imaging of active seismic data. A fundamental problem in seismic imaging is that both the depth reflectivity and velocity distribution of the subsurface have to be predicted by only seismic events observed at the surface, which is a mathematically ill-posed problem. Therefore, the seismic imaging process consists of two key components: 1) reflectivity estimation, 2) velocity estimation.

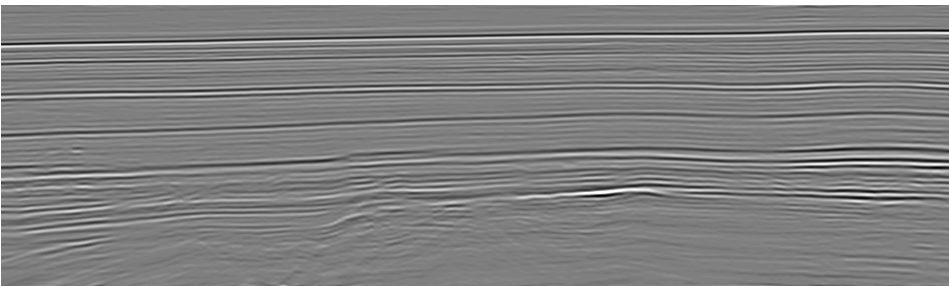


Figure 1.1: *An example of seismic imaging result, which is the estimated reflectivity in chapter 3.*

1.2 Reflectivity estimation

A key process to estimate a reflectivity model of the subsurface by seismic data is called *migration*, where this word was introduced by Hagedoorn (1954). According to well-known literature (Yilmaz, 2001), “migration moves dipping reflections to their true subsurface positions and collapses diffractions, thus increasing spatial resolution and yielding a seismic image of the subsurface”. To move the reflections to their accurate subsurface positions, knowledge regarding propagation velocities of seismic waves in the subsurface is required. Therefore, a velocity model needs to be assumed in order to estimate a reflectivity model by the seismic migration process. In this section, the major seismic migration schemes are reviewed.

■ 1.2.1 Kirchhoff migration

Kirchhoff migration is a seismic migration scheme based on the so-called Kirchhoff integral (Schneider, 1978), which is an analytical solution of the wave equation by an integral formulation in order to describe wavefield extrapolation to predict unknown propagated wavefields from known wavefields at some measurement locations. In Kirchhoff migration, travel-times of seismic waves in the subsurface are usually calculated by ray tracing (e.g. Julian and Gubbins, 1977; Aki and Richards, 1980) based on the transport and eikonal equations, which are approximations to the wave equation at a high frequency limit.

Kirchhoff migration is a migration scheme proposed about 40 years ago, but it is still used because it does not require high quality data and large computational cost compared to modern migration algorithms. However, since Kirchhoff migration is based on high-frequency approximations, the accuracy of the migration result is not guaranteed in some complex structures (e.g. Gray et al., 2001).

■ 1.2.2 One-way wave equation migration

One-way wave equation migration is a migration scheme to address the complex structure problem in the Kirchhoff migration. Although the Kirchhoff migration deals with wave propagation via calculated travel-times, one-way wave equation migration handles waveform-based propagation at each step of the wavefield-continuation process (Claerbout, 1971; Claerbout and Doherty, 1972; Gazdag, 1978; Stolt, 1978; Berkhout, 1982). While some literature simply calls this type of migration wave-equation migration (WEM) (Gazdag, 1978), the term WEM includes Kirchhoff migration in other literature, because Kirchhoff migration is also based on the wave equation. Therefore, since the definition of the term WEM is ambiguous, the term one-way WEM is used here. “One way” propagation means that the calculated propagation has a direction like upgoing and downgoing, and the upgoing and downgoing wavefields are separately calculated. On the other hand, “two way” propagation allows us to simultaneously calculate two directions, which represent the propagation with 360 degree (Wapenaar and Berkhout, 1989).

One-way WEM is usually positioned between Kirchhoff migration and so-called reverse time migration (RTM), which will be explained later on, in terms of accuracy and computational cost. The limitation of the one-way WEM is a difficulty to image structures with steep dips, due to the assumption of the one-way propagator that does not allow wavefields to travel close to 90 degree or beyond.

■ 1.2.3 Reverse time migration

RTM is a so-called two-way migration method in which wavefields are propagated through the subsurface by solving the exact wave equation without any assumption on wave propagation direction in order to potentially deal with all dip events in complex structures (Baysal et al., 1983; McMechan, 1983; Whitmore, 1983). The modeling algorithm in RTM is based on some discretization method to directly solve the wave equation such as finite difference schemes (e.g. Alterman and

Karal, 1968; Boore, 1972; Virieux, 1986), finite element schemes (e.g. Lysmer and Drake, 1972; Smith, 1975), spectral schemes (e.g. Tal-Ezer et al., 1990) and pseudo-spectral schemes (e.g. Kosloff and Baysal, 1982; Kosloff et al., 1990). RTM is capable of obtaining accurate image for complex structures when the observed data has high S/N ratio and the input velocity is accurate, but the computational cost is high. Furthermore, it suffers from low-frequency artifacts (Mulder and Plessix, 2004) or unwanted spurious reflection events during the wavefields modeling stage.

■ 1.2.4 Least-squares migration

An advanced extension for each migration scheme is least-squares migration (LSM), which is a data-driven approach via an inversion process. In LSM, the observed shot data is simulated again from the reflectivity image, given the velocity model, by a so-called demigration method, which is some forward modeling process. The residual between the observed data and the simulated data is minimized in this inverse problem, and the gradient for the reflectivity update in each iteration is calculated by the back propagation of the data residual from the receiver side and the forward propagation of the original source field. On the basis of the updated reflectivity image and the given velocity model, the demigration process is performed in the next iteration, where the simulated data is again compared to the observed data to create the new residual, etc.

Keys and Weglein (1983) originally introduced a generalized linear inversion for the so-called Born approximation (Born and Wolf, 1980), which is a scattering theory proposed in quantum mechanics, to accommodate insufficient and inaccurate data. Then, the concept of LSM was incorporated into the Kirchhoff migration process (Nemeth et al., 1999). Chavent and Plessix (1999) also proposed prestack depth migration operator to estimate true amplitudes in a least-squares manner. Later, the framework of LSM was extended to one-way wave equation migration (Kühl and Sacchi, 2003; Kaplan et al., 2010) and RTM for an acoustic assumption (Dong et al., 2012; Dai and Schuster, 2013; Wong et al., 2015). Recently, elastic extensions of least-squares RTM were

also proposed (Feng and Schuster, 2017; Duan et al., 2017).

Full wavefield migration (FWM) is a migration algorithm that can also be categorized as LSM (Berkhout and Verschuur, 2011; Berkhout, 2014b; Davydenko and Verschuur, 2017b). The forward modeling process in FWM is the so-called full wavefield modeling (FWMod) (Berkhout, 2014a), which is a reflection modeling method based on estimated reflectivity, including all higher-order scattering and transmission effects, with similarities to the Bremmer series (Bremmer, 1951) in optics.

An improvement of accuracy for each migration scheme can be expected via this data-driven inversion process, although the computational cost also increases because of the inversion process that is introduced in LSM, which requires the migration process to be carried out several times.

1.3 Velocity estimation

Since the seismic migration process assumes an input velocity model, velocity estimation is also an important component of the seismic imaging workflow. Even though we may apply an accurate migration scheme, we cannot estimate a correct image of the subsurface when the input velocity for the migration is inaccurate. The features of three commonly used velocity estimation methods are described in the following.

■ 1.3.1 Normal move-out velocity analysis

A classical method to build a velocity model is normal move-out (NMO) velocity analysis. This analysis is done by manually picking so-called semblance plots (Taner and Koehler, 1969), which are velocity analysis displays to obtain the NMO velocity function. The method is based on a horizontal layered subsurface with small velocity contrasts. Although some initial velocity models can be usually built by this NMO velocity analysis, the estimation for complex structures and high-velocity contrast mediums is challenging.

■ 1.3.2 Migration velocity analysis

Migration velocity analysis (MVA) (e.g. Al-Yahya, 1989; MacKay and Abma, 1992; Liu and Bleistein, 1995; Jervis et al., 1996) is capable of estimating the velocity distribution by improving the flatness of events in so-called common image gathers, which are the migrated images in which the contributions to the image from different sources or offsets have not yet been combined. Therefore, in each subsurface location reflection information is organized in the local offset or angle domain (Biondi and Symes, 2004; Sava and Biondi, 2004). MVA does not require subjective picking, source wavelet estimation, nor expensive computations, and MVA is a stable process to provide relatively accurate velocity models. However, it is difficult to correctly build high-resolution and high-contrast velocity models using MVA.

■ 1.3.3 Full waveform inversion

Full waveform inversion (FWI) enables us to estimate a high-resolution velocity model by using the mentioned least-squares process based on inversion for full ‘waveform’ data (presented by Tarantola, 1984). It uses the so-called diving waves in the standard FWI algorithm for seismic data, where the forward modeling is usually done via finite difference modeling of the wave equation. However, as FWI is a strongly non-linear inverse problem, the solutions tend to converge to local minima, which result into inaccurate velocity models. It is known that several conditions such as correctness of the initial velocity and presence of low frequency/wavenumber components in the observed data are crucial in avoiding the local minima in FWI (see e.g. Virieux and Operto, 2009). Several approaches have been proposed to mitigate the local minima and reduce the conditions of the initial velocity model and the frequency/wavenumber. For example, the effectiveness of a misfit criterion via Wiener filters for the observed data for FWI was demonstrated in Warner and Guasch (2016). van Leeuwen and Herrmann (2013) introduced a novel formulation for FWI based on a penalty method to reduce the local minimum problem. In the formulation, the objective function consists of a misfit term and an extra penalty term, which represents

how accurately the wavefields satisfy the wave equation. In relation to the local minima problem, reconstructing the velocity for high-contrast geobodies (e.g. salt, basalt) is still a challenge in FWI. In Esser et al. (2015, 2018), an approach was introduced based on total variation and the Hinge loss function, which is a loss function used for training classifiers in machine learning, especially so-called support vector machine algorithm, to realize the estimation for a high-contrast velocity model. This approach was expanded by the split Bregman method (Goldstein and Osher, 2009), although these approaches require the prior information for true total variation and Hinge loss of the subsurface (Qiu et al., 2016). In addition to the challenge caused by the local minima, data acquisition with long offsets is indispensable to obtain enough depth penetration because standard FWI exploits diving waves. As a next step, in recent years, reflection-based full waveform inversion (RWI or RFWI) has been presented to address this challenge (e.g. Irabor and Warner, 2016; Sun et al., 2016, 2017). It is envisioned that via conventional diving wave FWI and RWI, a high-resolution velocity image can be obtained that allows direct interpretation of the subsurface structures (Routh et al., 2017).

1.4 Simultaneous reflectivity and velocity estimation

Approaches to simultaneously estimate both reflectivity and velocity models have also been proposed by integrating these two processes.

■ 1.4.1 Migration-based traveltimes formulation

Migration-based traveltimes (MBTT) formulation was the first approach to estimate reflectivity and velocity together (Chavent et al., 1994). Since this method also exploits least-squares process by a non-linear inversion, reflectivity and velocity models are updated in each iteration by minimizing the misfit between observed data and modeled data. Plessix et al. (1999) applied the MBTT formulation to a simple ray modeling and Clément et al. (2001) extended to 2D acoustic FD modeling in order

to utilize primary reflected waves. However, high computational cost is stated as the drawback of this method in Clément et al. (2001), and it has not been commonly used.

■ 1.4.2 Joint migration inversion

Joint Migration Inversion (JMI) was also proposed as a method to simultaneously estimate both velocity and depth reflectivity distributions and to reduce the mentioned non-linearity in FWI (Berkhout, 2012, 2014c). The seismic modeling algorithm in JMI process is the FWMod described in the previous section. Since the FWMod is a reflection modeling process, including higher-order scattering and transmission effects, as mentioned, the JMI process is capable of utilizing all reflected waves, including internal multiples, for the imaging. In the data modeling procedure, the velocity model only affects the kinematics without any scattering effect in the modeling operators and the reflectivity model only deals with scattering effects. Hence, due to the involved decoupling of the parameters reflectivity and velocity, the inverse problem becomes less non-linear.

1.5 Challenges in seismic imaging

There are still several challenges in seismic imaging. In this section, two significant challenges that are discussed in this thesis are explained in relation to the previous descriptions of different imaging and velocity estimation algorithms.

■ 1.5.1 Low frequencies-dependent velocity estimation

Nowadays, diving waves-based FWI is widely used for velocity estimation. As stated, however, the presence of the low frequencies and low wavenumbers in the observed data plays a key role in the accurate velocity output. Here, the desired range of frequencies represents is usually 1-15 Hz of observed seismic data. On the other hand, since the features

in JMI are to reduce the non-linearity that is present in FWI and to exploit reflected waves, including internal multiples, such low frequencies dependency of velocity estimation can be reduced, but the presence of the low frequencies are still desired to stably build accurate velocity models in JMI.

In recent years, the technologies to acquire such low frequency components of both marine and land seismic data have been developed. In case of marine seismic data acquisition and processing, the introduction of so-called broadband streamers and the development of advanced deghosting processes (e.g. Soubaras, 2010; Wang and Peng, 2012) have improved the quality of the low frequency components used for seismic imaging and reservoir characterization. However, since accurate deghosting is still a research topic, such low frequencies cannot always be utilized.

On the other hand, low frequency sources, like so-called broadband vibroseis, have been developed for land seismic acquisition (Plessix et al., 2010; Mahrooqi et al., 2012; Reust et al., 2015). However, such low frequency sources, including also dynamite, are not exploited/mobilized in all seismic surveys, because related issues such as surface topography, permission and cost have to be taken into account in seismic surveys. Hence, performing accurate velocity estimation without such low frequencies is still a challenge in both marine and land seismic imaging.

■ 1.5.2 Near-surface imaging

There are still several large challenges aside from the mentioned low frequency problem in land seismic imaging. In general the S/N ratio of land seismic data is relatively low due to the inherent problems such as coarse acquisition specifications and surface noise picked up by the receivers. Additionally, one of the most serious challenges is that a complex near surface with strong lateral heterogeneities has a large distortive impact on seismic imaging quality.

Prior approaches have been proposed to address this near-surface problem. For instance, so-called static correction (e.g. Cox, 1999) is a clas-

sical method to correct effects of the near surface in land seismic data processing, although its assumption that the ray paths in the near-surface region are straight and oriented in the vertical direction is not applicable to a complex near surface. Shtivelman and Canning (1988) proposed a wave equation-based solution to deal with the complexity, using redatuming operators that were based on a velocity model of the subsurface. However, obtaining the velocity estimation itself is a major challenge, because no proper reflections from the near surface are usually present to carry out common velocity estimation methods, such as migration velocity analysis.

One of the approaches to avoid velocity estimation in seismic imaging is a data-driven approach for focusing seismic data to a certain reflection boundary, which was introduced by Berkhout (1997) and further exemplified by Thorbecke (1997). It was shown that this so-called common focus point (CFP)-based technology can be used to remove the imprint of complex near-surface propagation effects from seismic data (see e.g. Hindriks and Verschuur, 2001; Kelamis et al., 2002; Verschuur and El-Marhoul, 2005; Al-Ali and Verschuur, 2006; El-Marhoul et al., 2009). Nevertheless, those implementations were based on the estimation of the redatuming operators in terms of traveltimes and they did not allow a correct amplitude preservation during redatuming. Haffinger and Verschuur (2010) introduced a method to estimate near-surface redatuming operators in a full waveform manner instead of simple traveltimes, such that detailed amplitude and phase information are included. This approach was extended by Vrolijk et al. (2012) to include more than one reflector to derive these full wavefield datuming operators. However, estimating the propagation operator from one or two laterally continuous reflectors below the weathering layer did not always provide a robust solution in which all physical relations are involved. Complex transmission effects and surface/internal multiples within the near-surface region are not included in this approach.

In order to apply model-driven near-surface corrections, the near-surface velocity model has also been estimated by several approaches. For example, first arrival travel-time tomography has been widely applied for land seismic imaging, especially near-surface imaging (e.g. Zhu et al.,

1992; Zhang and Toksöz, 1998). This method is an inversion algorithm to exploit the first arrival travel-time of the observed data and enables us to stably provide velocity models, owing to the relatively low non-linearity. The problems in this tomography are that the resolution of the velocity is low and long offset data is needed to estimate the velocity at deep depth levels. Moreover, the first arrivals have to be manually picked.

In recent years, we observe an increased application of FWI mainly based on diving waves (e.g. Ravaut et al., 2004; Adamczyk et al., 2014) and/or surface waves (e.g. Ernst, 2013) applied to onshore seismic data in order to estimate the velocity of the subsurface, including the near surface. In land data a mix of many types of arrivals are measured: body P-waves, multiples, converted waves, surface waves, diving and refracted waves. Therefore, such land data application of FWI and the involved data pre-processing steps are not straightforward.

1.6 Thesis objectives

The objective of this thesis is originally motivated by improving not only marine seismic imaging but also land seismic imaging. This study aims at realizing this objective by mainly extending the methodology around the mentioned JMI methodology. This thesis presents novel methods in terms of pre-processing, seismic forward modeling, reflectivity estimation and velocity estimation:

- **Pre-processing:**

To properly apply waveform modeling-based imaging schemes to land seismic data, their pre-processing plays a key role in the final result. A surface amplitude correction framework based on learning from some synthetic model will be proposed to reduce the difference of amplitude variations between the observed data and the simulated data by the seismic modeling algorithm in the used imaging scheme.

- **Omni-directional seismic modeling:**

Since the seismic modeling process in standard FWMod is based on typical one-way propagators, refracted/diving waves are not taken into account. A seismic modeling process for refracted/diving waves and reflected waves, including internal multiples, via one-way propagators will be presented via adding a horizontal propagation process, which is called omni-directional approach.

- **Omni-directional reflectivity estimation (migration):**

As standard FWM also does not deal with refracted/diving waves, an extended migration algorithm to handle such wave modes - based on the above mentioned modeling process - will be discussed.

- **Omni-directional velocity estimation (inversion):**

A velocity inversion process will be also derived by utilizing the omni-directional seismic modeling. This means that an omni-directional extension of JMI can be implemented by calculating both the omni-directional reflectivity and velocity estimation.

- **Reflectivity-constrained velocity estimation (inversion):**

The main feature of JMI is that velocity and reflectivity are independent parameters to describe the observed seismic data. However, for accurate velocity estimation in JMI, when searching the global minimum, some coupling between reflectivity and velocity model is desired in the end. An improved velocity estimation process, based on a reflectivity constraint, to accurately solve this inverse problem will be proposed. This reflectivity constraint will be extended to horizontal direction in the omni-directional approach.

1.7 Thesis outline

This thesis consists of six chapters, where this introduction is the first one. The following chapters are:

- **Chapter 2** gives the used mathematical notations and representations for reflection, transmission, and propagation. On the basis

of the notations and representations, the algorithms of FWMod and JMI are reviewed.

- **Chapter 3** presents a reflectivity constraint for velocity estimation to optimally solve the inverse problem for active seismic imaging. This constraint is based on the fact that a velocity model can be derived from the definition of reflectivity and acoustic impedance. The constraint does not require any prior information of the subsurface and large extra computational costs, like the calculation of so-called Hessian matrices. We incorporate this constraint into the JMI algorithm and call it reflectivity-constraint joint migration inversion (RCJMI). Numerical and field data examples are given to demonstrate the validity of our proposed algorithm in case accurate initial models and the low frequency components of observed seismic data are absent.
- **Chapter 4** describes the application of RCJMI for land seismic data without the low frequency components. In the preprocessing before RCJMI is applied, a new surface amplitude correction framework based on learning from some synthetic model is proposed to reduce the difference of amplitude variations between the observed data and the simulated data by the seismic modeling in the used imaging scheme. We test RCJMI with the proposed amplitude correction framework for a land field dataset where the low frequency components less than 10 Hz are absent.
- **Chapter 5** discusses a novel seismic modeling process for refracted/diving waves and reflected waves including internal multiples via one-way propagators. This modeling process correctly incorporates refracted/diving waves and reflected waves into FWMod and deals with not only vertical propagation but also horizontal propagation to realize such waves by an omni-directional extension. On the basis of this modeling process, we present an omni-directional wavefield migration (OWM) algorithm to estimate horizontal reflectivity by mainly utilizing refracted/diving waves. Finally, we propose an omni-directional joint migration inversion (OJMI) method to simultaneously estimate reflectivity

and velocity models via vertical and horizontal propagation.

- **Chapter 6** describes the main conclusions of the thesis and gives recommendations for further research.

Notations and review

We consider a 2D seismic data with $N_r \in \mathbb{N}^+$ receivers, $N_s \in \mathbb{N}^+$ sources and $N_\omega \in \mathbb{N}^+$ frequency samples. Since a so-called staggered grid is utilized to describe the grid of the subsurface, the reflectivity model and P-wave velocity model are defined by $\mathbf{m}_r \in \mathbb{R}^{(N_z+1) \times N_x}$ and $\mathbf{m}_c \in \mathbb{R}^{>0, N_z \times N_x}$ with $N_x \in \mathbb{N}^+$ lateral samples and $N_z \in \mathbb{N}^+$ depth samples. The elements of the reflectivity and velocity model at a lateral location x and depth z are written by $r(x, z)$ and $c(x, z)$, respectively.

Let $\mathbf{P}^\pm(z_n) \in \mathbb{C}^{N_r \times N_s \times N_\omega}$ and $\mathbf{W}^\pm(z_{n\pm 1}; z_n) \in \mathbb{C}^{N_r \times N_r \times N_\omega}$ be the downgoing/upgoing pressure wavefields at depth level z_n and the downgoing/upgoing propagation operators between z_n and $z_{n\pm 1}$ in the frequency domain, respectively (Wapenaar and Berkhout, 1989). Here, the signs, $*$ ⁺ and $*$ ⁻, represent ‘downgoing’ and ‘upgoing’. Let $\mathbf{R}^\cup(z_n), \mathbf{R}^\cap(z_n) \in \mathbb{R}^{N_r \times N_r}$ be reflection operators at z_n , as illustrated in Fig. 2.1. When we consider a monochromatic wavefield with the frequency ω_f , $f = 1, 2, \dots, N_\omega$, and the source located at $x_{s,\xi}$, $\xi = 1, 2, \dots, N_s$, the downgoing/upgoing wavefields are written by $\vec{P}^\pm(z_n, x_{s,\xi}, \omega_f) \in \mathbb{C}^{N_r}$, which are the vectors in $\mathbf{P}^\pm(z_n)$. The propagation operator at the frequency ω_f is also described by $\mathbf{W}^\pm(z_{n\pm 1}; z_n, \omega_f) \in \mathbb{C}^{N_r \times N_r}$, which are the matrices in $\mathbf{W}^\pm(z_{n\pm 1}; z_n)$. For the simplification, we use the following notations (see e.g. Berkhout, 1982) for monochromatic wavefields and propagation

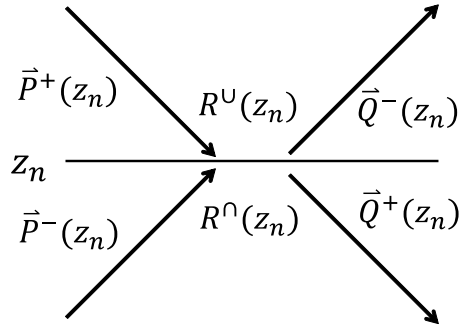


Figure 2.1: Reflected and transmitted wavefields at depth level z_n .

operators:

$$\vec{P}^\pm(z_n) \equiv \vec{P}^\pm(z_n, x_{s,\xi}, \omega_f), \quad (2.0.1)$$

$$\mathbf{W}^\pm(z_{n\pm 1}; z_n) \equiv \mathbf{W}^\pm(z_{n\pm 1}; z_n, \omega_f). \quad (2.0.2)$$

Note that although we describe and demonstrate the process for the 2D case, the method can easily be extended to the full 3D situation (such as described in Kinneking et al. (1989); Davydenko and Verschuur (2017b)).

2.1 Representations for reflection, transmission, and propagation

This subsection reviews the representation for the reflection, transmission, and propagation to introduce our discussed inverse problem. When a monochromatic downgoing wavefield $\vec{P}^+(z_n)$ at depth level z_n is reflected at a sharp discontinuity, we can write the reflected wavefield in the frequency domain by using a reflection operator $\mathbf{R}^U(z_n)$:

$$\vec{Q}^-(z_n) = \mathbf{R}^U(z_n)\vec{P}^+(z_n). \quad (2.1.3)$$

Since the upgoing wavefield does not contain only energy from the reflected wavefield but also from the transmitted wavefield in the discon-

tinuity, at depth level z_n , we can actually express:

$$\vec{Q}^-(z_n) = \mathbf{T}^-(z_n)\vec{P}^-(z_n) + \mathbf{R}^U(z_n)\vec{P}^+(z_n), \quad (2.1.4)$$

where $\vec{Q}^-(z_n) \in \mathbb{C}^{N_r}$ indicates the total upgoing wavefield moving away from the discontinuity, $\vec{P}^-(z_n)$ describes the upgoing incoming wavefield at depth level z_n from below, and $\mathbf{T}^-(z_n)$ represents a transmission operator in the discontinuity (see Fig. 2.1). The transmission operators are defined as $\mathbf{T}^\pm(z_n) \equiv \mathbf{I} + \delta\mathbf{T}^\pm(z_n)$, meaning that differential transmission operator $\delta\mathbf{T}^\pm(z_n) = 0$ if there is no contrast at z_n . Then, equation (2.1.4) is written as:

$$\vec{Q}^-(z_n) = \vec{P}^-(z_n) + \delta\mathbf{T}^-(z_n)\vec{P}^-(z_n) + \mathbf{R}^U(z_n)\vec{P}^+(z_n), \quad (2.1.5)$$

where the last two terms contain the scattered wavefields at depth level z_n for the wavefields that arrive from both sides.

In a similar way, the total downgoing wavefield $\vec{Q}^+(z_n) \in \mathbb{C}^{N_r}$ that leaves the depth level z_n can be written as a sum of transmission and reflection terms:

$$\vec{Q}^+(z_n) = \mathbf{T}^+(z_n)\vec{P}^+(z_n) + \mathbf{R}^\cap(z_n)\vec{P}^-(z_n) \quad (2.1.6)$$

$$= \vec{P}^+(z_n) + \delta\mathbf{T}^+(z_n)\vec{P}^+(z_n) + \mathbf{R}^\cap(z_n)\vec{P}^-(z_n). \quad (2.1.7)$$

Equations (2.1.4)-(2.1.7) are similar to the representation of the Bremmer series (Bremmer, 1951), which is exploited in the mentioned FW-Mod process (Berkhout and Verschuur, 2011; Berkhout, 2014a).

The wavefields $\vec{Q}^\pm(z_n)$ after the transmission and reflection at z_n propagate to the neighboring depth levels $z_{n\pm 1}$ via the wavefield extrapolation based on the Rayleigh II integral:

$$\vec{P}^\pm(z_{n\pm 1}) = \mathbf{W}^\pm(z_{n\pm 1}; z_n)\vec{Q}^\pm(z_n), \quad (2.1.8)$$

where $\mathbf{W}^+(z_{n+1}; z_n)$ and $\mathbf{W}^-(z_{n-1}; z_n)$ are the downgoing and upgoing propagation operators to propagate the wavefields to the next depth level $z_{n\pm 1}$. The elements of \mathbf{W} are written by:

$$W_{i,j}(z_m; z_n) = 2\text{sign}(z_n - z_m) \frac{\partial G}{\partial z}(x_j, z_m; x_i, z_n), \quad (2.1.9)$$

where, $G(x_j, z_m; x_i, z_n)$ represents a Green's function from the original location (x_j, z_m) to the extrapolated wavefield location at (x_i, z_n) . Within a homogeneous layer, the matrix \mathbf{W} exhibits a Toeplitz structure. This means that the one-way propagation operator in the medium (i.e. one column of \mathbf{W}) is simply defined by a phase-shift operator (Gazdag, 1978):

$$\vec{W}_j(z_m; z_n) = \mathcal{F}_x^{-1}[e^{-jk_z\Delta\tilde{z}}e^{-jk_x x_j}], \quad (2.1.10)$$

with

$$k_z = \begin{cases} \sqrt{k^2 - k_x^2}, & (|k_x| \leq |k|), \\ -j\sqrt{k_x^2 - k^2}, & (|k_x| > |k|), \end{cases} \quad (2.1.11)$$

where $\Delta\tilde{z} \equiv |z_n - z_m|$ and $k \equiv \omega/c$. \mathcal{F}_x is the spatial Fourier transform.

In the FWMod procedure, the scattering process described in equations (2.1.5) and (2.1.7) and the propagation process described in equation (2.1.8) are recursively performed at each depth. The procedure can be summarized in the following equations (Berkhout, 2014a; Staal, 2015):

[1] for the downgoing wavefields ($m = 1, 2, \dots, N_z$):

$$\begin{aligned} \vec{P}^+(z_m) &= \underline{\mathbf{W}}^+(z_m; z_0)\vec{S}^+(z_0) \\ &+ \sum_{n=0}^{m-1} \underline{\mathbf{W}}^+(z_m; z_n)\mathbf{R}^\cap(z_n)\vec{P}^-(z_n), \end{aligned} \quad (2.1.12)$$

with

$$\underline{\mathbf{W}}^+(z_m; z_n) \equiv \mathbf{W}^+(z_m; z_{m-1}) \prod_{l=m-1}^{n+1} \mathbf{T}^+(z_l)\mathbf{W}^+(z_l; z_{l-1}), \quad (2.1.13)$$

[2] for the upgoing wavefields ($m = 0, 1, \dots, N_z - 1$):

$$\begin{aligned} \vec{P}^-(z_m) &= \underline{\mathbf{W}}^-(z_m; z_M)\vec{P}^-(z_M) \\ &+ \sum_{n=m+1}^M \underline{\mathbf{W}}^-(z_m; z_n)\mathbf{R}^\cup(z_n)\vec{P}^+(z_n), \end{aligned} \quad (2.1.14)$$

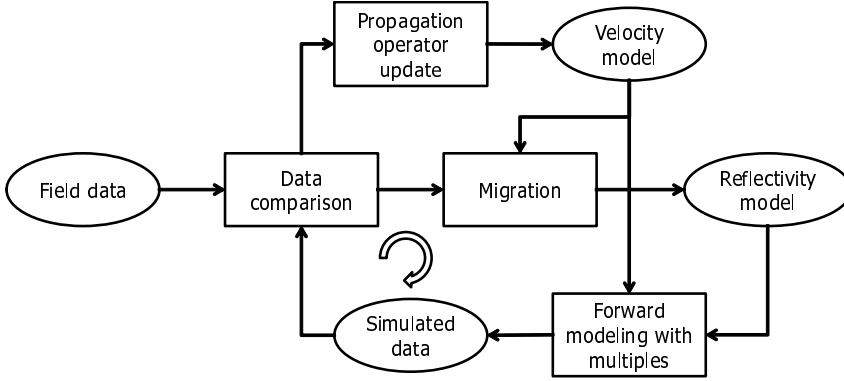


Figure 2.2: Flowchart of JMI.

with

$$\underline{\mathbf{W}}^-(z_m; z_n) \equiv \mathbf{W}^-(z_m; z_{m+1}) \prod_{l=m+1}^{n-1} \mathbf{T}^-(z_l) \mathbf{W}^-(z_l; z_{l+1}), \quad (2.1.15)$$

where $\vec{S}^+(z_0)$ is a downgoing source wavefield at the surface.

2.2 Joint migration inversion

JMI is an inversion algorithm to optimize velocity and reflectivity models of the subsurface by minimizing the residual between observed and modeled data, which takes into account the scattering and propagation process based on the mentioned FWMod process, as shown in Fig. 2.2.

In the standard implementation for JMI (Staal and Verschuur, 2013; Staal et al., 2014; Verschuur et al., 2016), the objective function, which contains the residual between the observed data and the modeled data, is defined as follows:

$$J = \frac{1}{2} \sum_{\xi}^{N_s} \sum_f^{N_{\omega}} \|\vec{P}_{obs}^-(z_0, x_{s,\xi}, \omega_f) - \vec{P}_{mod}^-(z_0, x_{s,\xi}, \omega_f)\|^2, \quad (2.2.16)$$

where $\vec{P}_{obs}^-(z_0, x_{s,\xi}, \omega_f)$ and $\vec{P}_{mod}^-(z_0, x_{s,\xi}, \omega_f)$ represent the observed shot data and forward modeled shot data, respectively. Note that this objective function takes into account multi-shots and multi-frequency components of seismic data instead of one shot and its monochromatic component.

The reflectivity and velocity update for equation (2.2.16) is solved by a gradient decent scheme, as shown in Algorithm 1. Here, ∇J_r and α_r represent the gradient and scale factor for the reflectivity update. ∇J_σ and α_σ are the gradient and scale factor for the slowness update. Furthermore, $*$ ^(k) indicates k th iteration in this inversion and $*_i$ is the roundtrip number in JMI. The detailed formulation for the update rules is described in Appendix A.

Algorithm 1 Reflectivity and velocity update process by gradient decent scheme for JMI

Input: $K \in \mathbb{N}^+$, initial guess: r^0, c^0

- 1: **for** $k = 1 \rightarrow K$ **do**
- 2: $i = 2k - 1$
- 3: Compute \vec{Q}_i^\pm by equation (2.1.5) and (2.1.7)
- 4: Compute \vec{P}_i^\pm by equation (2.1.12) and (2.1.14)
- 5: Compute ∇J_r by equation (A.1.4)
- 6: Compute α_r by equation (A.1.7)
- 7: Update $r^{(k)} = r^{(k-1)} + \alpha_r \nabla J_r$
- 8: $i = 2k$
- 9: Compute \vec{Q}_i^\pm by equation (2.1.5) and (2.1.7)
- 10: Compute \vec{P}_i^\pm by equation (2.1.12) and (2.1.14)
- 11: Compute ∇J_σ by equation (A.2.22)
- 12: Compute α_σ by equation (A.2.24)
- 13: Update $\sigma^{(k)} = \sigma^{(k-1)} + \alpha_\sigma \nabla J_\sigma$
- 14: **end for**

On the basis of the above procedure, JMI enables to automatically update reflectivity and slowness/velocity models of the subsurface in an alternating manner in each iteration. Like typically done in FWI, to improve the convergence, the JMI process is run according to a certain frequency schedule, starting with a low frequency range and expanding the range after certain number of iterations. The main feature of JMI is that forward modeling is based on the independent parameter sets, being reflectivity and propagation velocity. By decoupling those

parameters, the inversion becomes less non-linear.

A simple example for JMI is given in Fig. 2.3 and 2.4. Figure 2.3 represents a synthetic true reflectivity and velocity model. Figure 2.4 (a) and (b) indicate initial models for JMI, while Fig. 2.4 (c) and (d) illustrate the reflectivity and velocity estimated by JMI. Although it can be seen that JMI provides a plausible reflectivity and velocity model, the next chapter will discuss an algorithm to enhance the performance of JMI.

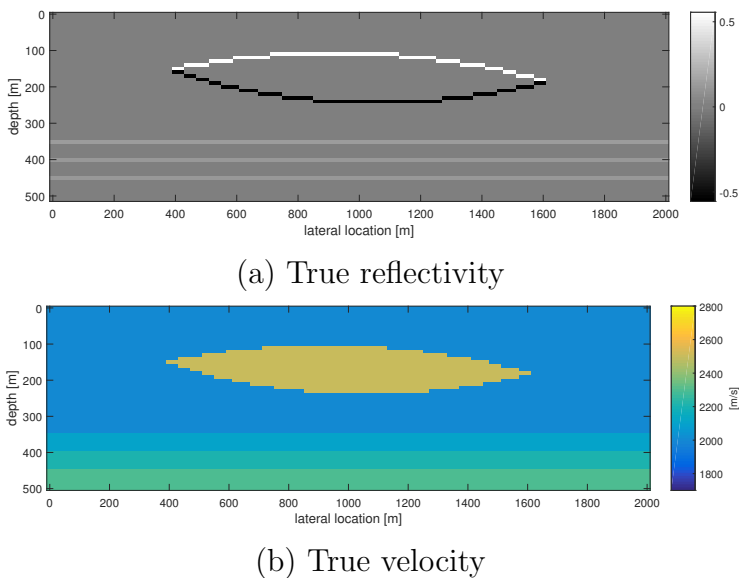
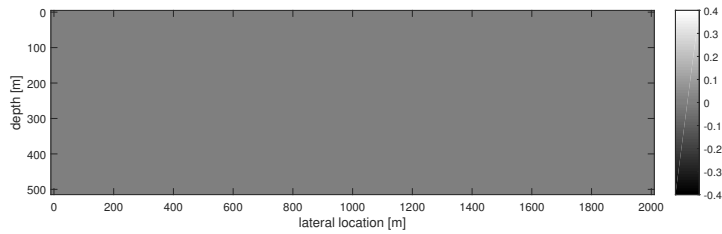
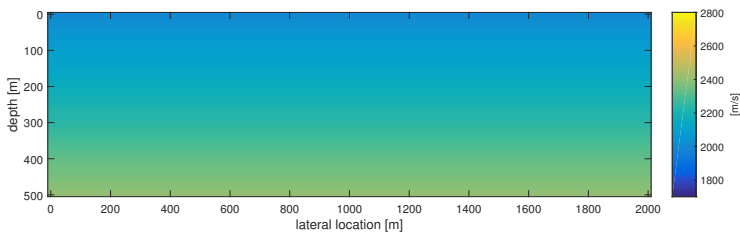


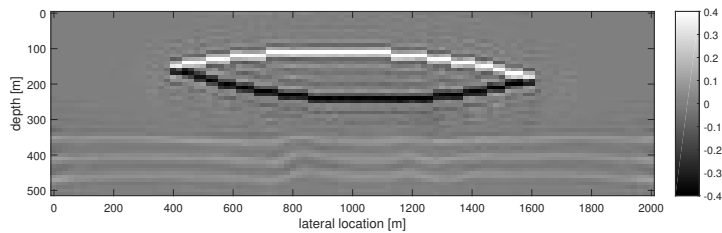
Figure 2.3: True reflectivity (a) and velocity (b) model.



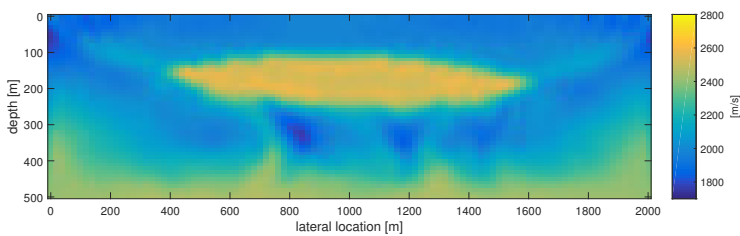
(a) Initial reflectivity



(b) Initial velocity



(c) Estimated reflectivity



(d) Estimated velocity

Figure 2.4: (a,b) Initial models for JMI and (c,d) the models estimated by JMI.

Reflectivity-constrained JMI

3.1 Introduction

A fundamental problem in active seismic imaging is that both the depth reflectivity and velocity distribution of the subsurface have to be predicted by only seismic events observed at the surface, which is a mathematically ill-posed problem. Two types of approaches have been mainly utilized for addressing this problem in the oil and gas industry. One approach consists of solving the problems in two separate steps: velocity estimation and migration. In this approach, migration provides the reflectivity image based on the typically smooth velocity model provided by a preceding velocity estimation method, like FWI (Tarantola, 1984; Virieux and Operto, 2009). Another approach is to utilize an interactive procedure between velocity and reflectivity estimation. For example, MVA (e.g. Al-Yahya, 1989; MacKay and Abma, 1992; Liu and Bleistein, 1995; Jervis et al., 1996) has been commonly used as this approach.

As mentioned in chapter 1, FWI enables us to estimate high-resolution velocity model through matching a forward modeled response with the events of observed ‘waveform’ data (presented by Tarantola, 1984). As stated, since FWI is the first process in the two steps-based approach,

migration has to be applied by using the velocity predicted by FWI.

As described in chapter 1, MVA (e.g. Al-Yahya, 1989; MacKay and Abma, 1992; Liu and Bleistein, 1995; Jervis et al., 1996) is capable of estimating the velocity distribution by improving the flatness of events in so-called common image gathers (Fig. 3.1), which are the migrated images in which the contributions to the image from different sources or offsets have not yet been combined. Therefore, in each subsurface location reflection information is organized in the local offset or angle domain (Biondi and Symes, 2004; Sava and Biondi, 2004). Although the velocity updated via MVA takes into account information on the reflectivity of the migrated image, a more advanced migration scheme, like RTM, is often applied for finally using the predicted velocity after MVA. Thus, the approach based on MVA also requires an additional migration process to give the final image as the second step.

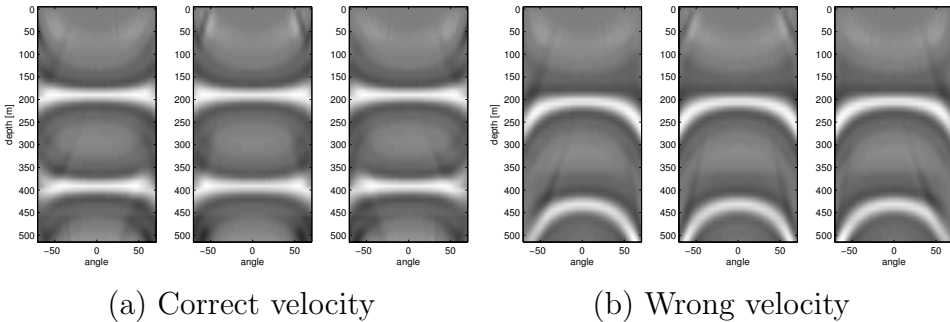


Figure 3.1: An example of angle-domain common image gathers for (a) correct velocity and (b) wrong velocity.

JMI was proposed as one of the methods to simultaneously estimate both velocity and depth reflectivity distributions and to reduce the mentioned non-linearity in FWI (Berkhout, 2012, 2014c). This means that the two steps containing velocity analysis and migration are integrated in the JMI process. As introduced in chapter 2, the seismic modeling algorithm in the JMI process is FWMod (Berkhout, 2014a; Berkhout and Verschuur, 2011), which is a reflection modeling process, including

higher-order scattering and transmission effects, with similarities to the Bremmer series in optics (Bremmer, 1951). This means that the JMI process utilizes internal multiples for the imaging, although conventional imaging methods such as MVA, standard RTM, and standard FWI, do not deal with internal multiples. In the data modeling procedure, the velocity model only affects the kinematics without any scattering effect in the modeling operators and the reflectivity model only deals with scattering effects. Hence, due to the involved decoupling of the parameters reflectivity and velocity, the inverse problem becomes less non-linear. However, for accurate inversion, when searching the global minimum, some coupling between the two types of parameters will be desired in the end. In this chapter, we discuss how we can enhance the estimated velocity model through the estimated reflectivity, such that a better solution to the inverse problem is obtained.

Several prior studies reported that reflectivity information can aid the optimization of velocity inversion. Although MVA might be also categorized in such approach, the drawback of MVA is that the resolution of the updated velocity is relatively low because MVA exploits the flatness of common image gathers instead of fitting modeled with measured data. A scheme to combine MVA with FWI was also suggested in Biondi and Almomin (2012) to improve the resolution. Incorporating the information of migration into the tomography process for velocity estimation improves the final depth image (Mathewson et al., 2012), where a dirty salt velocity was estimated via the reflectivity, which is computed by true-amplitude RTM, under a 1D assumption (Ji et al., 2011). With a similar reasoning, Maciel et al. (2015) applied nonlinear filters from the field of morphological image processing to address this challenge and to enhance the contrast of the JMI velocity solution. In order to improve the resolution of the velocity model, we also presented an initial algorithm and result (Masaya and Verschuur, 2016b) for reflectivity-constrained velocity estimation by adding a slowness-based objective function in JMI, which independently inverts reflectivity and velocity models.

In this chapter, we propose a new reflectivity-based objective function instead of the mentioned slowness-based objective function for the

reflectivity-constrained velocity estimation in JMI. The objective function per iteration is based on the difference between the estimated reflectivity from JMI and the reflectivity approximated from the estimated velocity from JMI. In addition, a sparsity constraint for the reflectivity estimation is introduced to promote the effect of the reflectivity-constrained velocity estimation. We call this algorithm Reflectivity-Constrained JMI (RCJMI) (Masaya and Verschuur, 2018a). RCJMI aims to automatically update velocity with this reflectivity constraint and also reflectivity in an alternating iteration process.

This chapter gives an algorithm for our proposed reflectivity-constrained velocity estimation in section 3.2. Next, synthetic and field data examples are presented in section 3.3 and 3.4, respectively. Then, the extension to mitigate the assumption in the proposed algorithm is mainly discussed in section 3.5. Finally, we draw conclusions in section 3.6.

3.2 Algorithm

In this section, we describe our proposed algorithm for iteratively and automatically reflectivity-constrained velocity estimation. The main idea in this algorithm is to impose a reflectivity-based constraint during the velocity estimation step to improve the accuracy of the JMI solution, as illustrated in Fig. 3.2 and 3.3. Furthermore, a sparsity constraint in the reflectivity update is introduced to further enhance the reflectivity-constrained velocity estimation.

■ 3.2.1 Reflectivity approximation based on velocity estimation

Firstly, we derive a reflectivity approximation formulated from the estimated velocity. When waves are normally incident to the boundary between depth level z_n and z_{n+1} , the reflection equation for $n = 0, \dots, M-2$ can be described by:

$$r(x, z_{n+1}) = \frac{\rho(x, z_{n+1})c(x, z_{n+1}) - \rho(x, z_n)c(x, z_n)}{\rho(x, z_{n+1})c(x, z_{n+1}) + \rho(x, z_n)c(x, z_n)}, \quad (3.2.1)$$

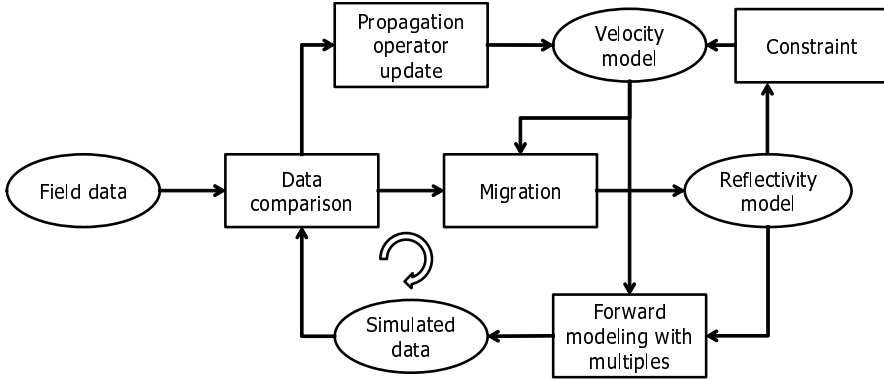


Figure 3.2: Overview of RCJMI, where the estimated image also constrains the velocity update.

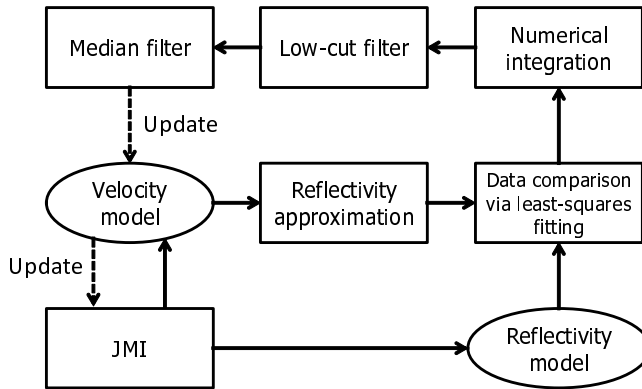


Figure 3.3: The scheme for the velocity update with a reflectivity-based constraint in each iteration of RCJMI. Note that the block “JMI” refers to the process shown in Fig. 2.2.

where c and ρ represent the velocity and density model of the subsurface. Next, we assume for our constraint calculation that the density model ρ is constant because in general the density variation of the subsurface is relatively small compared to the velocity variation. Then, the

reflectivity is approximately calculated by:

$$r(x, z_{n+1}) \simeq \frac{c(x, z_{n+1}) - c(x, z_n)}{c(x, z_{n+1}) + c(x, z_n)}. \quad (3.2.2)$$

We additionally assume that the horizontal variation of velocity models is much smaller than the vertical variation. Then, a numerical approximation can be obtained from equation (3.2.2):

$$r(x, z_{n+1}) \sim \frac{\Delta c}{\Delta z} \times \text{const.}, \quad (3.2.3)$$

where $\Delta c \equiv c(x, z_{n+1}) - c(x, z_n)$ and $\Delta z \equiv z_{n+1} - z_n$. Equation (3.2.3) means a relationship between reflectivity and velocity. Therefore, an estimated reflectivity r_{constr} derived from the velocity model, which does not include the scale of the correct reflectivity, can be defined by:

$$r_{constr} \equiv \frac{\partial c}{\partial z}. \quad (3.2.4)$$

■ 3.2.2 Objective function

An objective function for our proposed RCJMI is defined by the mentioned reflectivity approximation based on the estimated velocity, i.e. r_{constr} , and is given as:

$$\begin{aligned} J &= \frac{1}{2} \sum_{\xi}^{N_s} \sum_f^{N_{\omega}} \|P_{obs}^-(z_0, x_{s,\xi}, \omega_f) - P_{mod}^-(z_0, x_{s,\xi}, \omega_f)\|^2 \\ &+ \lambda_2 \|r(x, z) - \Lambda r_{constr}(x, z)\|_2^2 \\ &+ \frac{\lambda_3}{2} \sum_x \sum_z \ln\{1 + \kappa^{-2} r^2(x, z)\}, \end{aligned} \quad (3.2.5)$$

where $\lambda_2, \lambda_3 \in \mathbb{R}^+$ represent the weight parameters for the second and third terms, respectively. $\Lambda \in \mathbb{R}^+$ represents a scale factor between $r(x, z)$ and $r_{constr}(x, z)$ that also takes care of the difference in units and the fact that density variations were neglected. $\kappa \in \mathbb{R}^+$ indicates

a parameter controlling the sparseness of the reflectivity. We express separately the three terms in the RHS of equation (3.2.5):

$$J_1 \equiv \frac{1}{2} \sum_{\xi}^{N_s} \sum_f^{N_{\omega}} \|P_{obs}^-(z_0, x_{s,\xi}, \omega_f) - P_{mod}^-(z_0, x_{s,\xi}, \omega_f)\|^2, \quad (3.2.6)$$

$$J_2 \equiv \lambda_2 \|r(x, z) - \Lambda r_{constr}(x, z)\|_2^2, \quad (3.2.7)$$

$$J_3 \equiv \frac{\lambda_3}{2} \sum_x \sum_z \ln\{1 + \kappa^{-2} r^2(x, z)\}, \quad (3.2.8)$$

where J_1 is the standard misfit term that is also described in equation (2.2.16). J_2 is a term of the reflectivity constraint to minimize the residual between the reflectivity calculated by JMI and the reflectivity approximated by the estimated velocity from JMI. J_3 is an optional term to enhance the sparseness of the reflectivity (Sacchi et al., 1998). As for the weight parameter (λ_2) and sparsity parameter (λ_3) in RCJMI, the optimum values are determined via several parameter tests in each example. Note that if λ_2 is chosen too large, velocity updates will be calculated almost exclusively from the integrated reflectivity values. On the other hand, if λ_2 and λ_3 are chosen too small, the velocity and reflectivity updates will be mainly determined by the data misfit term.

■ 3.2.3 Reflectivity and velocity updates

As stated previously, the update procedure in JMI consists of the reflectivity and slowness/velocity updates, which are derived from the gradient descent scheme. In RCJMI, the standard misfit function described by J_1 of equation (3.2.6) and the sparsity function described by J_3 of equation (3.2.8) are used for the reflectivity update. On the other hand, the velocity update in RCJMI is based on the standard misfit function shown in J_1 of equation (3.2.6) and the reflectivity-constraint function expressed by J_2 of equation (3.2.7).

The gradient of J_3 for the reflectivity update is simply calculated by:

$$\nabla J_{3,r}(x, z) = \lambda_3 \frac{r(x, z)}{\kappa^2 + r^2(x, z)}. \quad (3.2.9)$$

Therefore, the following reflectivity update for RCJMI is given:

$$r^{(k+1)}(x, z) = r^{(k)}(x, z) + \alpha_r(\nabla J_{1,r}(x, z) + \nabla J_{3,r}(x, z)). \quad (3.2.10)$$

As for the velocity update in RCJMI, since the approximated reflectivity $r_{constr}(x, z)$ does not have a correct scale, the reflectivity residual $r_{res}(x, z)$ between $r(x, z)$ and $r_{constr}(x, z)$ is computed via least-squares fitting in the first step (see Fig. 3.3):

$$r_{res}(x, z) \equiv r(x, z) - \Lambda r_{constr}(x, z), \quad (3.2.11)$$

$$\Lambda = \arg \min_{\Lambda} \|r(x, z) - \Lambda r_{constr}(x, z)\|_2^2. \quad (3.2.12)$$

To obtain the gradient of J_2 for the velocity update, we take the numerical integral of the reflectivity residual $r_{res}(x, z)$ along z :

$$\nabla J_{2,c}(x, z) = \lambda_2 \int_{z_0}^z r_{res}(x, z') dz'. \quad (3.2.13)$$

We apply a low-cut filter and a horizontal median filter to the gradient $\nabla J_{2,c}(x, z)$. The low-cut filter applied to the gradient $\nabla J_{2,c}(x, z)$ along z is used to provide a sharp velocity update as the intention of this penalty term is to provide more detail to the estimated velocity. After the application of the low-cut filter, a horizontal median filter for the gradient is performed to remove the outliers, which can generate artifacts.

A scale factor for the velocity update of this term is given by:

$$\alpha_{c2} = \frac{\sum_x \sum_z |\int_{z_0}^z r_{res}(x, z') dz'|^2}{\sum_x \sum_z |\int_{z_0}^z r(x, z') dz'|^2}. \quad (3.2.14)$$

Therefore, we can update the velocity model as follows:

$$c^{(k+1)}(x, z) = \frac{1}{\sigma^{(k)}(x, z) + \alpha_{\sigma 1} \nabla J_{1,\sigma}(x, z)} + \alpha_{c2} \nabla J_{2,c}(x, z), \quad (3.2.15)$$

where $\nabla J_{1,\sigma}$ and $\alpha_{\sigma 1}$ are the gradient and scale factor of the slowness $\sigma (= 1/c)$ in standard JMI, which correspond to ∇J_{σ} of equation (A.2.22) and α_{σ} of equation (A.2.24) in Appendix A. The reflectivity and velocity update procedure in RCJMI is summarized in Algorithm 2.

Algorithm 2 Reflectivity and velocity update process in RCJMI

Input: $K \in \mathbb{N}^+$, initial guess: r^0, c^0

```

1: for  $k = 1 \rightarrow K$  do
2:    $i = 2k - 1$ 
3:   Compute  $\vec{Q}_i^\pm$  by equation (2.1.5) and (2.1.7)
4:   Compute  $\vec{P}_i^\pm$  by equation (2.1.12) and (2.1.14)
5:   Compute  $\nabla J_{1,r}$  by equation (A.1.4)
6:   Compute  $\nabla J_{3,r}$  by equation (3.2.9)
7:   Compute  $\alpha_r$  by equation (A.1.7)
8:   Update  $r^{(k)} = r^{(k-1)} + \alpha_r(\nabla J_{1,r} + \nabla J_{3,r})$ 
9:    $i = 2k$ 
10:  Compute  $\vec{Q}_i^\pm$  by equation (2.1.5) and (2.1.7)
11:  Compute  $\vec{P}_i^\pm$  by equation (2.1.12) and (2.1.14)
12:  Compute  $\nabla J_{1,\sigma}$  by equation (A.2.22)
13:  Compute  $\nabla J_{2,c}$  by equation (3.2.13)
14:  Apply low-cut filter and median filter to  $\nabla J_{2,c}$ 
15:  Compute  $\alpha_{\sigma 1}$  by equation (A.2.24)
16:  Compute  $\alpha_{c2}$  by equation (3.2.14)
17:  Update  $c^{(k)} = 1/(\sigma^{(k-1)} + \alpha_{\sigma 1}\nabla J_{1,\sigma} + \alpha_{c2}\nabla J_{2,c})$ 
18:  Compute  $\sigma^{(k)} = 1/c^{(k)}$ 
19: end for

```

3.3 Numerical examples

This section provides two synthetic data examples and one field data example to evaluate the effectiveness of RCJMI in comparison with standard JMI. Shot data for the synthetic examples is generated by FWMod with a Ricker source wavelet centered at 20 Hz in order to correctly examine the effect of our proposed constraints using the so-called 'inverse crime'. Up to the 5th order of multiples are included in the synthetic data. The acquisition in the synthetic examples assumes to use fixed receivers at the top of the depth level ($z=0$).

■ 3.3.1 Example 1: Lens-shaped model

The first example is a 2D model containing a lens-shaped anomaly, shown in Fig. 3.4 (a) and (b). The model consists of the high-velocity region with a lens shape and three horizontal reflectors under the region. The receiver and source intervals are 20 m and 80 m, respectively.

Three frequency schedules, as shown in Table 3.1-3.3, for the iteration

Table 3.1: *The frequency schedule I for JMI and RCJMI in the first example.*

Order	Frequency (Hz)	No. of iterations
1	5-10	12
2	5-20	12
3	5-30	10
4	5-40	106
		Total 140

Table 3.2: *The frequency schedule II for JMI and RCJMI in the first example.*

Order	Frequency (Hz)	No. of iterations
1	5-10	5
2	5-20	15
3	5-30	15
4	5-40	105
		Total 140

Table 3.3: *The frequency schedule III for JMI and RCJMI in the first example.*

Order	Frequency (Hz)	No. of iterations
1	10-15	5
2	10-23	15
3	10-32	15
4	10-40	105
		Total 140

of the inversions are tested to investigate the frequency dependence with the same conditions aside from the schedule. The maximum offset in the data used for the inversion is 2000 m. Figure 3.4 (c) and (d) show the initial velocity and reflectivity models for the inversions. The parameters $\lambda_2=15$, $\lambda_3=5.0 \times 10^{-7}$, and $\kappa=2.5 \times 10^{-2}$ are used for RCJMI.

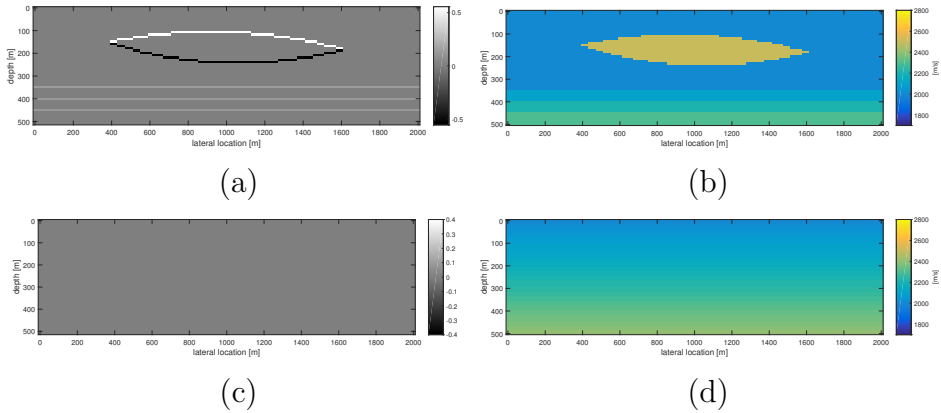


Figure 3.4: True and initial models in the first example. (a) True reflectivity. (b) True velocity. (c) Initial reflectivity. (d) Initial velocity.

Figure 3.5 (a)-(h) represent the results of JMI and RCJMI with frequency schedule I. It can be seen that RCJMI accurately inverts a velocity field and, as a result, the reflectivity image is also correctly migrated (see Fig. 3.5 (g) and (h)). On the other hand, Fig. 3.6 (a)-(h) and Fig. 3.7 (a)-(d) indicate the results of JMI and RCJMI with frequency schedule II and III, respectively. As shown in Fig. 3.5 (b) and (f), the velocity profiles given by JMI apparently includes the artifacts beneath the high velocity region, while these are almost absent in Fig. 3.6 (b), (f) and Fig. 3.7 (b). This means that the accuracy of the models estimated by JMI strongly depends on each frequency schedule. However, RCJMI is capable of providing highly accurate velocity and reflectivity models, as illustrated in Fig. 3.8.

To quantitatively evaluate the accuracy of the velocity estimation for JMI and RCJMI, the following velocity error c_{error} is defined:

$$c_{error} \equiv \frac{\sum_x \sum_z |c_{true}(x, z) - c_{est}(x, z)|}{\sum_x \sum_z c_{true}(x, z)}, \quad (3.3.16)$$

where c_{true} and c_{est} are the true velocity and the velocity estimated by the inversions. Figure 3.9 shows the iteration dependence of the velocity

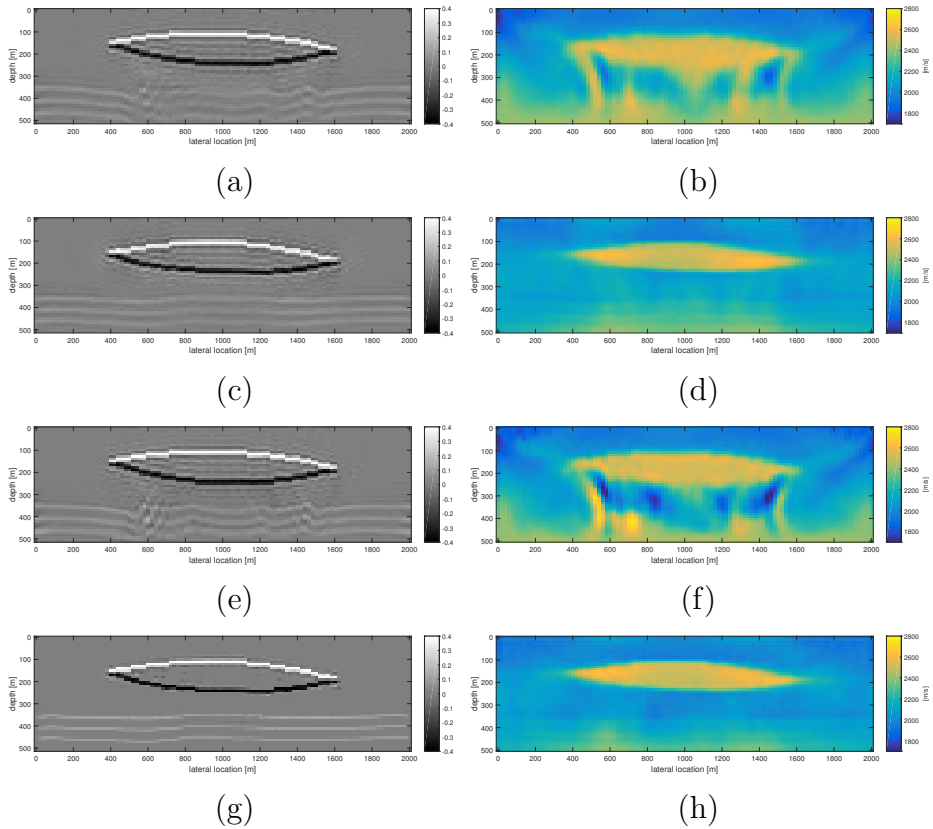


Figure 3.5: Reflectivity and velocity models in the first example with frequency schedule I (5-40 Hz). (a) JMI reflectivity after 65 iterations. (b) JMI velocity after 65 iterations. (c) RCJMI reflectivity after 65 iterations. (d) RCJMI velocity after 65 iterations. (e) JMI reflectivity after 130 iterations. (f) JMI velocity after 130 iterations. (g) RCJMI reflectivity after 130 iterations. (h) RCJMI velocity after 130 iterations. It can be seen that RCJMI stably provides accurate velocity models, while the velocity models estimated by JMI include artifacts.

error c_{error} for JMI and RCJMI using frequency schedule I, II, and III. It is clear that the performance of RCJMI is not sensitive to the frequency schedule, although the solutions inverted by JMI relatively converge to local minima. Note again that we are dealing with a so-called 'inverse

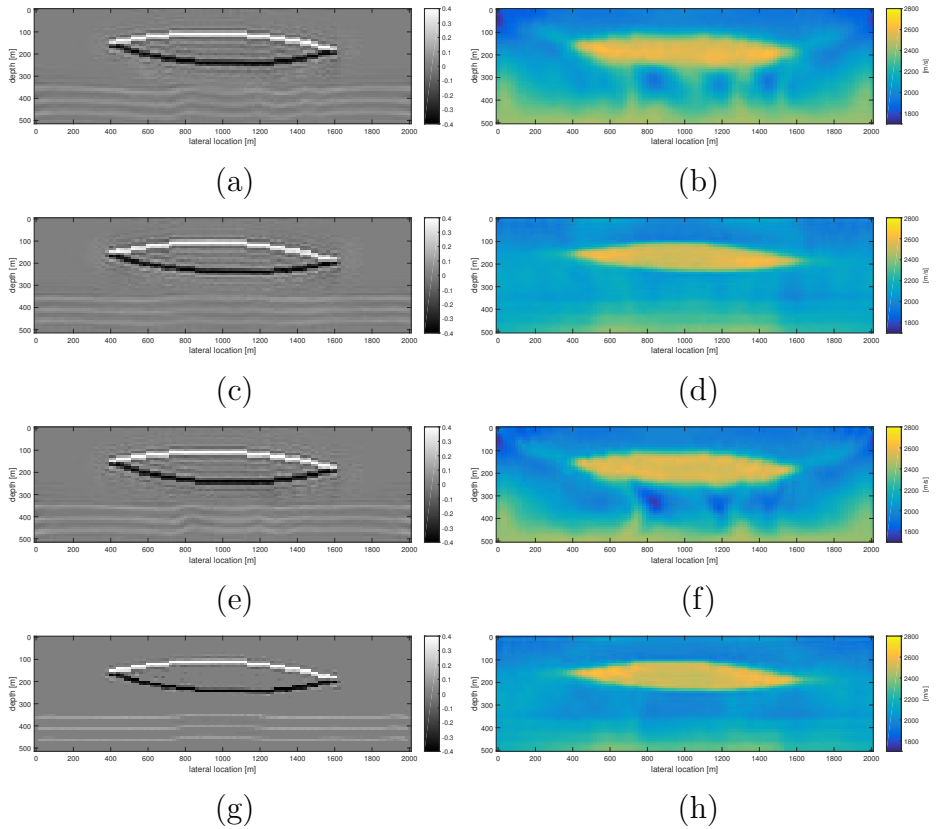


Figure 3.6: *Estimated reflectivity and velocity models for the first example with frequency schedule II (5-40 Hz). (a) JMI reflectivity after 65 iterations. (b) JMI velocity after 65 iterations. (c) RCJMI reflectivity after 65 iterations. (d) RCJMI velocity after 65 iterations. (e) JMI reflectivity after 130 iterations. (f) JMI velocity after 130 iterations. (g) RCJMI reflectivity after 130 iterations. (h) RCJMI velocity after 130 iterations. Note that with this frequency schedule JMI results are better, although the final RCJMI results are similar to that of schedule I (Fig. 3.5)*

crime’, where the same FWMod is used to obtain the shot data. Thus, in theory a perfect inversion result could be obtained, so any imperfection is due to the used inversion algorithm.

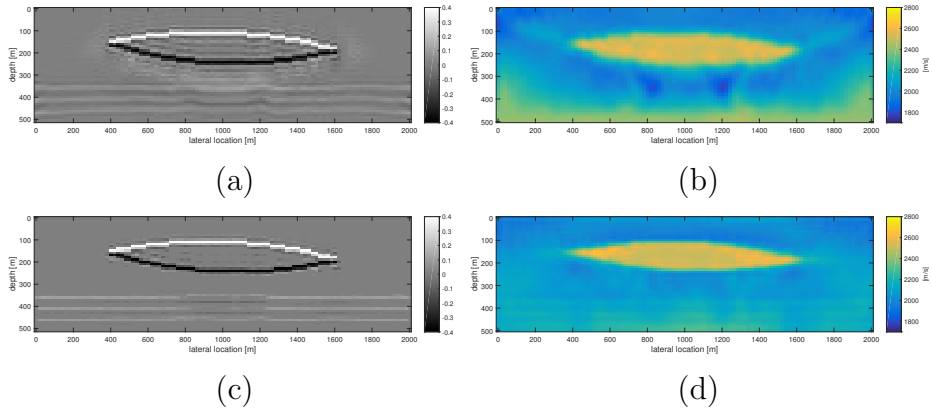


Figure 3.7: Estimated reflectivity and velocity models for the first example with frequency schedule III (10-40 Hz). (a) JMI reflectivity after 130 iterations. (b) JMI velocity after 130 iterations. (c) RCJMI reflectivity after 130 iterations. (d) RCJMI velocity after 130 iterations. As shown in (c) and (d), accurate reflectivity and velocity can be reconstructed by RCJMI even if the low frequency components smaller than 10 Hz are absent.

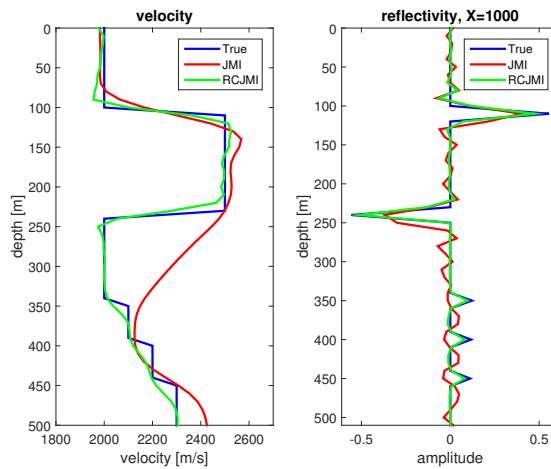


Figure 3.8: Comparison of the performance after 130 iterations between JMI and RCJMI with frequency schedule I (5-40 Hz) at lateral location $x = 1000$ m.

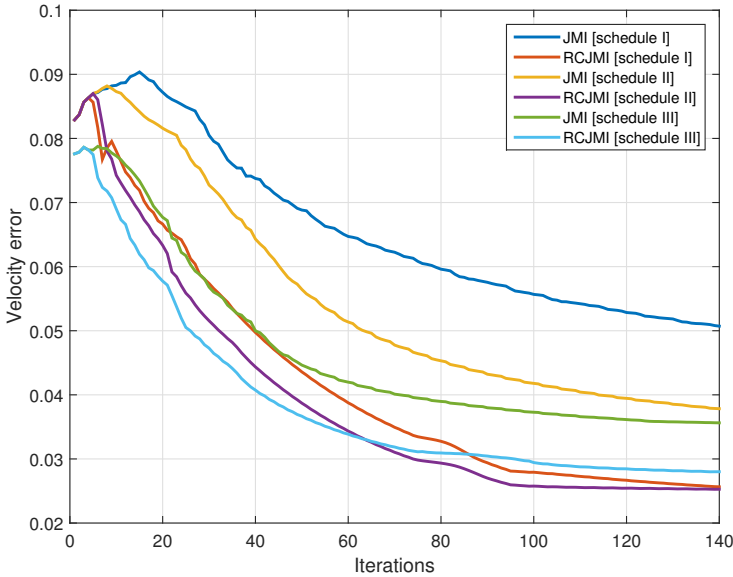


Figure 3.9: The velocity error c_{error} between the true velocity model and the estimated model from JMI and RCJMI with the frequency schedule I (5-40 Hz), II (5-40 Hz), and III (10-40 Hz). These results demonstrate that the solutions of RCJMI relatively converge to global minima (see red, purple, blue lines).

■ 3.3.2 Example 2: SEG/EAGE Salt model

As a more complex and realistic example, a 2D subset of the SEG/EAGE Salt model is used. Rescaling and horizontal resampling for this model are applied in order to reduce computation time. The model contains a salt body, which has high velocity, shown in Fig. 3.10 (a) and (b). The receiver and source intervals are 10 m and 40 m, respectively.

The frequency schedule I, II, and III, described in Table 3.4-3.6, are used for the inversions in this example in order to investigate the contribution of the low frequency components, which are crucial for standard FWI. Table 3.4 shows that the used frequency bands of seismic data for the inversion consists of 4 cycles: 1a-3a, 4b-6b, 7c-9c, and 10d-13d. This

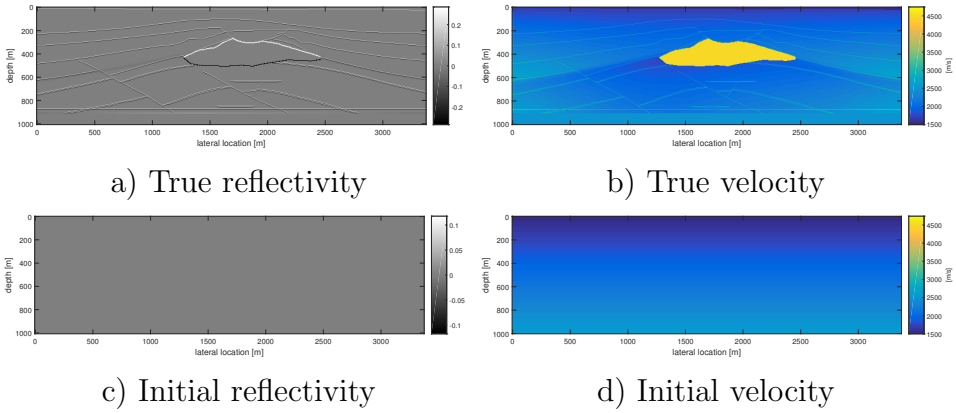


Figure 3.10: True and initial models in the second example. (a) True reflectivity. (b) True velocity. (c) Initial reflectivity. (d) Initial velocity.

Table 3.4: The frequency schedule I for JMI and RCJMI in the SEG/EAGE salt model example.

Order	Frequency (Hz)	No. of iterations
1a	5-10	10
2a	5-25	10
3a	5-40	10
4b	5-10	10
5b	5-25	10
6b	5-40	10
7c	5-10	10
8c	5-25	10
9c	5-40	10
10d	5-10	12
11d	5-20	12
12d	5-30	10
13d	5-40	56
		Total 180

Table 3.5: *The frequency schedule II for RCJMI in the SEG/EAGE salt model example.*

Order	Frequency (Hz)	No. of iterations
1a	7-11	10
2a	7-25.5	10
3a	7-40	10
4b	7-11	10
5b	7-25.5	10
6b	7-40	10
7c	7-11	10
8c	7-25.5	10
9c	7-40	10
10d	7-11	12
11d	7-20.6	12
12d	7-30.3	10
13d	7-40	56
		Total 180

Table 3.6: *The frequency schedule III for RCJMI in the SEG/EAGE salt model example.*

Order	Frequency (Hz)	No. of iterations
1a	10-14	10
2a	10-27	10
3a	10-40	10
4b	10-14	10
5b	10-27	10
6b	10-40	10
7c	10-14	10
8c	10-27	10
9c	10-40	10
10d	10-14	12
11d	10-22.7	12
12d	10-31.3	10
13d	10-40	56
		Total 180

procedure is effective to estimate high velocity contrasts like salt bodies by both JMI and RCJMI. The maximum offset used for the inversion is 3370 m. Figure 3.10 (c) and (d) show the initial velocity and reflectivity models for JMI and RCJMI, which do not include any information about the salt body. The parameter $\lambda_2=10$ is used for RCJMI. The sparse term is not exploited in this example ($\lambda_3=0$).

We show the results of JMI using frequency schedule I after 60 iterations in Fig. 3.11 (a) and (b) and after 180 iterations in Fig. 3.11 (e) and (f). The RCJMI results with frequency schedule I are illustrated in Fig. 3.11 (c), (d), (g), and (h) and the RCJMI results using the frequency schedule II, and III are shown in Fig. 3.12. Figure 3.13 represents the iteration dependency of the velocity error c_{error} for JMI and RCJMI.

It can be observed that after 180 iterations JMI does not reconstruct the correct shape of the salt body in the velocity estimation (see Fig. 3.11 (f)). However, RCJMI gives the accurate shape of the salt body owing to its reflectivity-constrained velocity estimation in an early iteration stage (see Fig. 3.11 (h)). As a result, the reflectivity image is clear (see Fig. 3.11 (g)), although the depth of the imaged reflectivity below the salt body is slightly inaccurate due to the overestimated velocity under the salt body. As shown in Fig. 3.12 and 3.13, both the velocity and reflectivity distributions are effectively estimated without accurate initial models and low frequency components of the observed seismic data. A close inspection of Fig. 3.13 shows that the results without the low frequency components up to 10Hz, surprisingly enough, show an improved performance in terms of the velocity estimation in RCJMI.

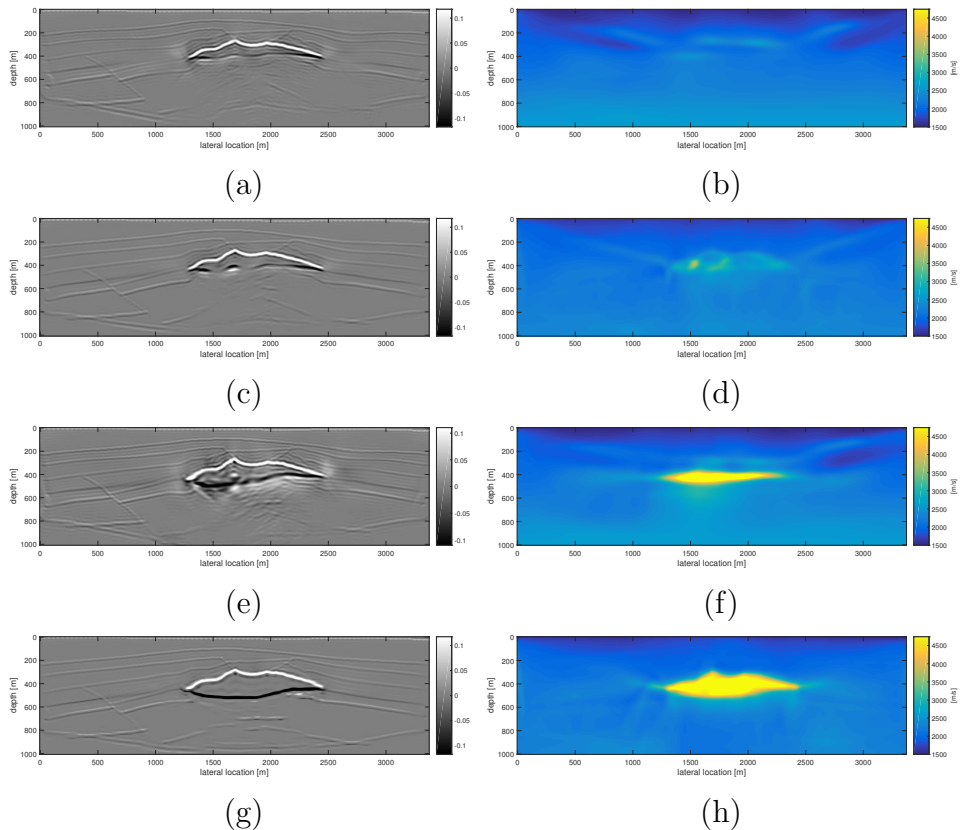


Figure 3.11: Reflectivity and velocity models in the second example with frequency schedule I (5-40 Hz). (a) JMI reflectivity after 60 iterations. (b) JMI velocity after 60 iterations. (c) RCJMI reflectivity after 60 iterations. (d) RCJMI velocity after 60 iterations. (e) JMI reflectivity after 180 iterations. (f) JMI velocity after 180 iterations. (g) RCJMI reflectivity after 180 iterations. (h) RCJMI velocity after 180 iterations.

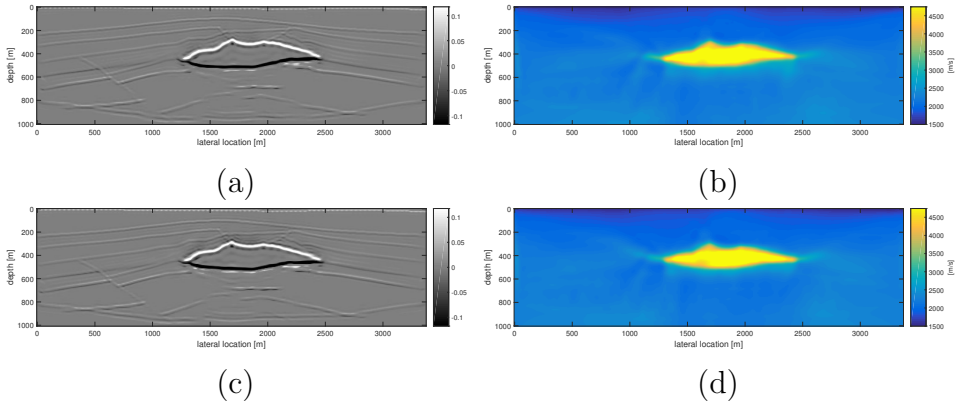


Figure 3.12: RCJMI reflectivity and velocity models after 180 iterations with frequency schedule II (7-40 Hz) and III (10-40 Hz). (a) RCJMI reflectivity with frequency schedule II (7-40 Hz). (b) RCJMI velocity with frequency schedule II (7-40 Hz). (c) RCJMI reflectivity with frequency schedule III (10-40 Hz). (d) RCJMI velocity with frequency schedule III (10-40 Hz).

3.4 Field data example

Finally, we test our proposed method for a 2D field data provided by Statoil. The data was acquired by a streamer survey in the North Sea, in the Vøring area, offshore Norway. The receiver and source intervals used in our process are 25 m and 50 m, respectively. The direct wave and the surface-related multiples have been removed, and receiver deghosting was applied.

The source wavelet used for JMI and RCJMI is estimated from the surface-related multiples using the so-called estimation of primaries by sparse inversion (EPSI) process (van Groenestijn and Verschuur, 2009). As shown in Table 3.7 and 3.8, 5-40 Hz and 7-40 Hz of the seismic data are prepared for JMI and RCJMI, respectively because it was demonstrated that RCJMI is not sensitive to the existence of low frequency components in the above synthetic examples. The maximum offset used

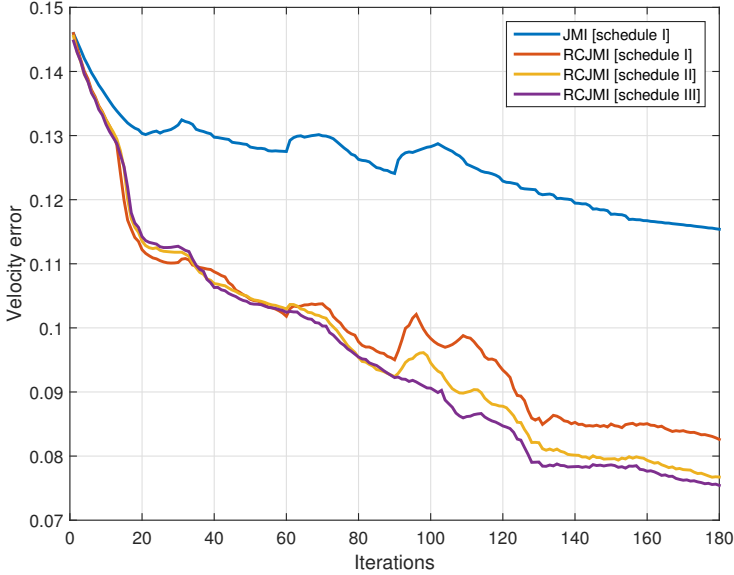


Figure 3.13: The velocity error c_{error} between the true velocity model and the estimated model from JMI and RCJMI using frequency schedule I (5-40 Hz), II (7-40 Hz), and III (10-40 Hz). Compared with JMI, RCJMI remarkably reduces the velocity error independently of the existence of low frequency components.

for the inversion is 2500 m. As the initial velocity model, a simple 1D velocity function shown in Fig. 3.14 (b) has been chosen. The parameter $\lambda_2=2$ is used for RCJMI. The sparsity term is not exploited in this example ($\lambda_3=0$).

Figure 3.14 (c) and (d) show the reflectivity and velocity estimated by JMI after 85 iterations and Fig. 3.14 (e) and (f) illustrate the migrated reflectivity and reconstructed velocity after 85 RCJMI iterations. To compare the detail of the estimated velocity and reflectivity models, we show the models in the depth levels 1500-2400 m in Fig. 3.15. As illustrated in Fig. 3.15 (a) and (b), the velocity reconstructed by RCJMI has high resolution and matches the structure of the estimated reflectivity well, although the lateral variation in the high velocity layer produced by JMI may be somewhat unlikely in the light of the estimated reflectivity.

Table 3.7: *The frequency schedule for JMI in the field data example.*

Order	Frequency (Hz)	No. of iterations
1a	5-10	10
2a	5-20	10
3a	5-30	10
4a	5-40	5
5b	5-20	10
6b	5-30	10
7b	5-40	5
8c	5-20	10
9c	5-30	10
10c	5-40	5
		Total 85

Table 3.8: *The frequency schedule for RCJMI in the field data example.*

Order	Frequency (Hz)	No. of iterations
1a	7-11	10
2a	7-20.6	10
3a	7-30.3	10
4a	7-40	5
5b	7-20.6	10
6b	7-30.3	10
7b	7-40	5
8c	7-20.6	10
9c	7-30.3	10
10c	7-40	5
		Total 85

tivity (see the part of the lateral locations 2000-3000 m and the depth levels 1700-2000 m in Fig. 3.15 (c)). Note that the difference of reflectivity estimated by between JMI and RCJMI is not large because the velocity variation in this example is relatively small.

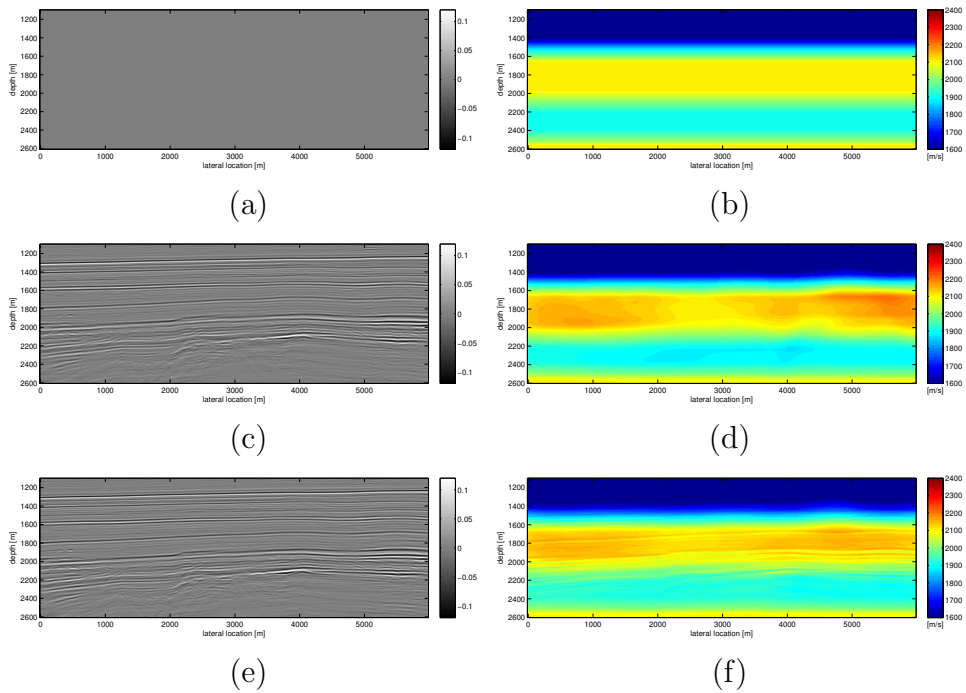
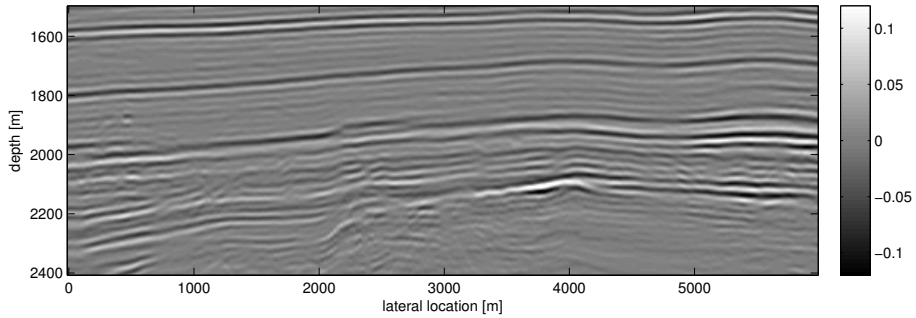
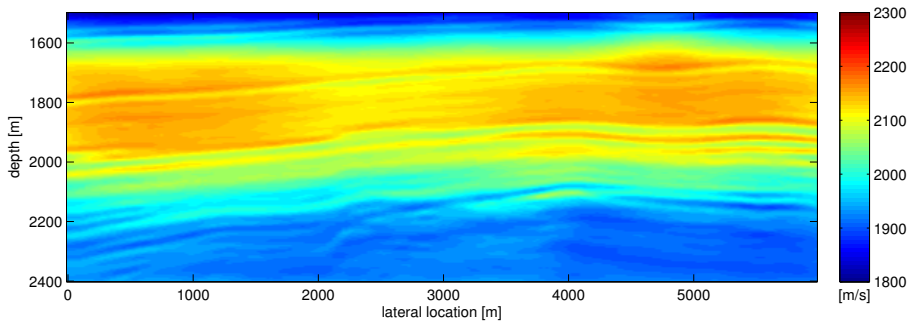


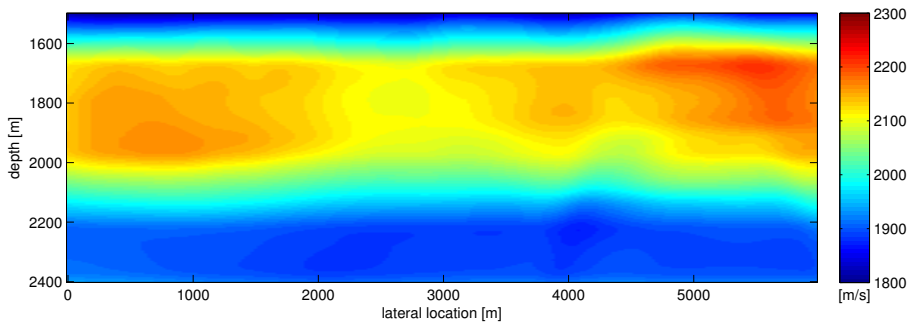
Figure 3.14: *Estimated reflectivity and velocity models in the field data example. (a) Initial reflectivity. (b) Initial velocity. (c) Reflectivity after 85 JMI iterations (5-40 Hz). (d) Velocity after 85 JMI iterations (5-40 Hz). (e) Reflectivity after 85 RCJMI iterations (7-40 Hz). (f) Velocity after 85 RCJMI iterations (7-40 Hz).*



(a)



(b)



(c)

Figure 3.15: Estimated reflectivity and velocity models for depth levels 1500-2400 m. (a) Reflectivity after 85 RCJMI iterations (7-40 Hz). (b) Velocity after 85 RCJMI iterations (7-40 Hz). (c) Velocity after 85 JMI iterations (5-40 Hz). It is found that the RCJMI velocity has a better correspondence to its reflectivity.

3.5 Discussion

■ 3.5.1 Computational cost

The extra computational cost of our proposed constraint is small. When the computational time of JMI and RCJMI for 10 iterations in the first example with the 2D lens-shaped model is measured, the increase of the computational time by RCJMI is 1.0 % per iteration on average. Therefore, this constraint does not require large extra computational cost.

■ 3.5.2 Density variations

Our proposed algorithm assumes that for the constraint calculation the density of the subsurface is constant, as stated in equation (3.2.2). Since density variations are generally smaller than velocity variations, this assumption would be realistic. However, density variations can be simply included in the constraint if a well-known empirical relation, so-called Gardner's relation (Gardner et al., 1974), in rock physics is used, which is given by:

$$\rho(x, z) = Ac(x, z)^B, \quad (3.5.17)$$

where $A, B \in \mathbb{R}^+$ represent the parameters for fitting. If velocity c and density ρ are measured in m/s and g/cm^3 , respectively, the observation that taking $A = 0.31$ and $B = 0.25$ gives a good fit for typical sediments is reported in Gardner et al. (1974). A modified reflectivity can be represented by the following equation instead of equation (3.2.1):

$$\begin{aligned} r(x, z_{n+1}) &= \frac{Ac(x, z_{n+1})^{B+1} - Ac(x, z_n)^{B+1}}{Ac(x, z_{n+1})^{B+1} + Ac(x, z_n)^{B+1}} \\ &= \frac{c(x, z_{n+1})^{B+1} - c(x, z_n)^{B+1}}{c(x, z_{n+1})^{B+1} + c(x, z_n)^{B+1}}. \end{aligned} \quad (3.5.18)$$

Here, using $\zeta(x, z) \equiv c(x, z)^{B+1}$, we can derive an approximation:

$$r(x, z_{n+1}) \sim \frac{\Delta\zeta}{\Delta z} \times \text{const.}, \quad (3.5.19)$$

where $\Delta\zeta \equiv \zeta(x, z_{n+1}) - \zeta(x, z_n)$. Since this equation (3.5.19) has a similarity with equation (3.2.3), a similar constraint can be formulated by defining $r_{constr}(x, z_{n+1}) \equiv \partial\zeta/\partial z$ and $r_{res}(x, z) \equiv r(x, z) - \Lambda r_{constr}(x, z)$. The gradient for velocity update described in equation (3.2.13) is replaced by:

$$\nabla J_{2,c}(x, z) = \lambda_2 [\zeta_{res}(x, z)]^{1/(B+1)}, \quad (3.5.20)$$

with

$$\zeta_{res}(x, z) \equiv \int_{z_0}^z r_{res}(x, z') dz'. \quad (3.5.21)$$

Hence, this extension of the proposed constraint is capable of dealing with density variations by giving a parameter B . Note again that since Gardner's relation is an empirical relation, this extension does not take account of any physics theory. Finally, note that this relation is only used in the constraint for updating the velocity; the forward modeling process within JMI does not rely on this assumption, as it will use the reflectivity directly obtained from the seismic data.

3.6 Conclusions

We propose an algorithm for reflectivity-constrained velocity estimation to improve its accuracy through a novel velocity update process utilizing the inverted reflectivity in each iteration. This algorithm does not require any prior information of the subsurface and large extra computational costs, such as the calculation of so-called Hessian matrices.

The numerical and field data examples demonstrate that the proposed reflectivity-constrained Joint Migration Inversion algorithm enables us to largely improve the automatic velocity estimation, even in the case of high-velocity contrasts, without accurate initial models, although the final velocity model is not perfect yet probably due to the typical velocity-depth ambiguities. The reflectivity distributions are also improved owing the accurate velocity. Moreover, the experiments showed that the performance of the algorithm was not sensitive to the existence

of the used low frequency components of observed data and to the used frequency schedule for the inversion.

Land JMI without low frequency components

4.1 Introduction

Waveform modeling-based imaging schemes such as FWI and least-squares RTM are commonly used to accurately estimate high-resolution velocity and reflectivity model of the subsurface. In recent years, land data application of FWI has increased for the purpose of hydrocarbon exploration and production (e.g. Plessix et al., 2010; Sedova et al., 2017) and crustal-scale investigations (e.g. Ravaut et al., 2004; Smithyman and Clowes, 2013). However, it is known that FWI has several limitations to predict accurate velocity models (see e.g. Virieux and Operto, 2009). Since the aim of FWI is solving a strongly non-linear optimization problem, the solutions tend to converge to local minima. To mitigate the local minima in FWI, past studies have suggested several requirements such as correctness of the initial velocity and presence of low frequency components of the observed seismic data to prevent the so-called cycle skips caused by the non-linearity (Virieux and Operto, 2009).

To avoid the cycle skip problem, the existence of low frequency components, like the range of 1-10 Hz, in seismic data plays a key role in

FWI. In recent years, we observe an increased acquisition of such low frequency range for land data by using so-called broadband vibroseis (Plessix et al., 2010; Mahrooqi et al., 2012; Reust et al., 2015) in order to improve the application of FWI to land data. The report that FWI was successfully applied to land data by using conventional vibroseis appears to be fairly limited (Adamczyk et al., 2015).

However, broadband vibroseis and dynamite, which also enables us to generate source wavelets with broadband frequency ranges including low frequency components, are not exploited in all survey areas. In general, as broadband vibroseis requires a heavy weight to produce the low frequency components of seismic waves, the broadband vibroseis tends to be huge, which means that the area where the vibroseis can be mobilized is limited. On the other hand, nowadays dynamite for seismic acquisition is often prohibited or limited in certain areas. Moreover, the cost of the seismic acquisition to utilize dynamite is relatively expensive compared to the use of vibroseis, because the production rate of dynamite-based acquisition is relatively low.

In addition to the above frequency problem of FWI, standard FWI requires long offsets to be measured to build the velocity at deep levels because diving/refracted waves are mainly utilized, although it was recently reported that not only diving/refracted waves but also reflected waves are exploited through several processing steps in case high quality land data is measured (Sedova et al., 2017). The acquisition with such long offsets makes the acquisition area limited, due to natural and artificial obstacles such as mountains, rivers, jungle and urban buildings, and the acquisition cost expensive.

We have proposed approaches based on JMI to address the above problems on land seismic imaging including near-surface imaging and shown synthetic data examples (Masaya and Verschuur, 2016a, 2017a). As discussed in previous chapters, JMI is an inversion algorithm to simultaneously estimate velocity and reflectivity models by utilizing reflected waves including internal multiples (Berkhout, 2012; Staal and Verschuur, 2012, 2013; Berkhout, 2014b). Since the non-linearity in JMI is relatively small, the cycle skip problem on the velocity estimation can be reduced. To further mitigate the cycle skip issue and

estimate more accurate velocity models, recently RCJMI was proposed (Masaya and Verschuur, 2018a), which imposes a reflectivity constraint for velocity estimation in the objective function for JMI. The constraint is based on the velocity model derived from the definition of reflectivity and acoustic impedance. Then, we demonstrated that the algorithm is not sensitive to the existence of the low frequency components of marine seismic data (see also the previous chapter).

In this chapter, we apply RCJMI to a land dataset without low frequency components. To properly apply the waveform modeling-based imaging scheme to land data, some surface amplitude correction is needed to mitigate source and receiver response sensitivity. Since the source and receiver response sensitivity depends on the near-surface condition, the source size, the coupling of sources and receivers, etc., it is difficult to accurately estimate the correction for the sensitivities, although several approaches under their assumptions have been proposed to deal with this problem (e.g. Taner and Koehler, 1981; van Vossen et al., 2006; Maurer et al., 2012). Moreover, when 2D waveform modeling-based algorithm is applied to 2D seismic data, an additional amplitude correction is required because real data always experiences 3D propagation. Approximate 3D to 2D conversion techniques have been presented to correct this amplitude effect in prior studies (e.g. Williamson and Pratt, 1995).

For this amplitude variation problem, we propose a novel surface amplitude correction framework (Masaya and Verschuur, 2018b) via learning from synthetic models in order to deal with source/receiver response sensitivity and adjust the amplitude of field data to make it suitable for the modeling algorithm in our imaging scheme. This framework utilizes the amplitude spectrum of the modeled data produced from some synthetic models. Synthetic and field data examples are shown to discuss the effectiveness of RCJMI and the proposed correction framework.

This chapter first gives the numerical examples of RCJMI to investigate the sensitivity to low frequency components of synthetic land data in section 4.2. Next, the proposed surface amplitude correction is discussed in section 4.3. Then, a field data example is shown in section 4.4. Finally, we draw discussion and conclusions on the basis of our results

in section 4.5 and 4.6, respectively.

4.2 Numerical examples

The synthetic land examples are given to test the performance of RCJMI without low frequency components of seismic data. The acquisition in the examples assumes to use fixed receivers at the top of the depth level z_0 .

■ 4.2.1 Example 1: Middle-East land model

The first example is a 2D model reflecting a geology with high-velocity contrasts in the Middle East, as shown in Fig. 4.1 (a) and (b). The receiver and source intervals are 20 m and 80 m, respectively. Shot data for this example is generated by FWMod with a Ricker source wavelet centered at 20 Hz. Up to the 5th order of internal multiples are included in the synthetic data. The maximum offset in the data used for RCJMI is 6780 m. Figure 4.1 (c) and (d) show the initial velocity and reflectivity models for the inversions. The initial velocity model is a rough 1D model, which values are quite different from the values of the true velocity. Figure 4.1 (e)-(f) show the results after 135 RCJMI iterations with 5-40 Hz and Fig 4.1 (g)-(h) is the results after 225 RCJMI iterations with 7-40 Hz. It can be seen that RCJMI with 7-40 Hz provides velocity and reflectivity models that are almost the same as the results obtained by the inversion with 5-40Hz, although the computation with 7-40 Hz requires additional iterations in this example.

■ 4.2.2 Example 2: Two geobodies model

The second example is a 2D model including two geobodies, as shown in Fig. 4.2 (a) and (b). This model assumes that there is some high velocity anomaly like volcanic rock in the near surface. The receiver and source intervals are 20 m and 40 m, respectively. Shot data for this example is generated by acoustic FD modeling with a Ricker source

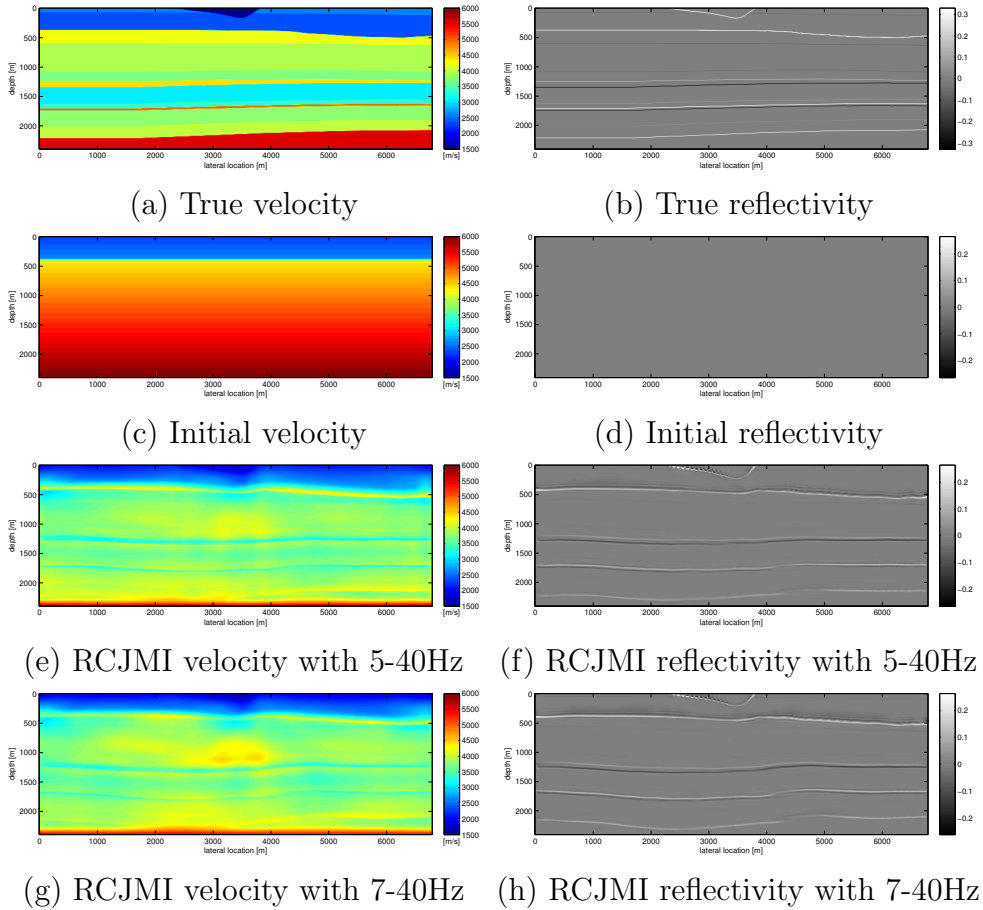


Figure 4.1: Reflectivity and velocity models in the example of the Middle-East model. (e)-(f) and (g)-(h) the results after 135 and 225 iterations RCJMI iterations, respectively.

wavelet centered at 20 Hz in order to avoid the so-called inverse crime in this example. The major differences between the FD modeling and FWMod, which is exploited in RCJMI, are the presence of AVO effects and refracted waves. FWMod as embedded in JMI currently does

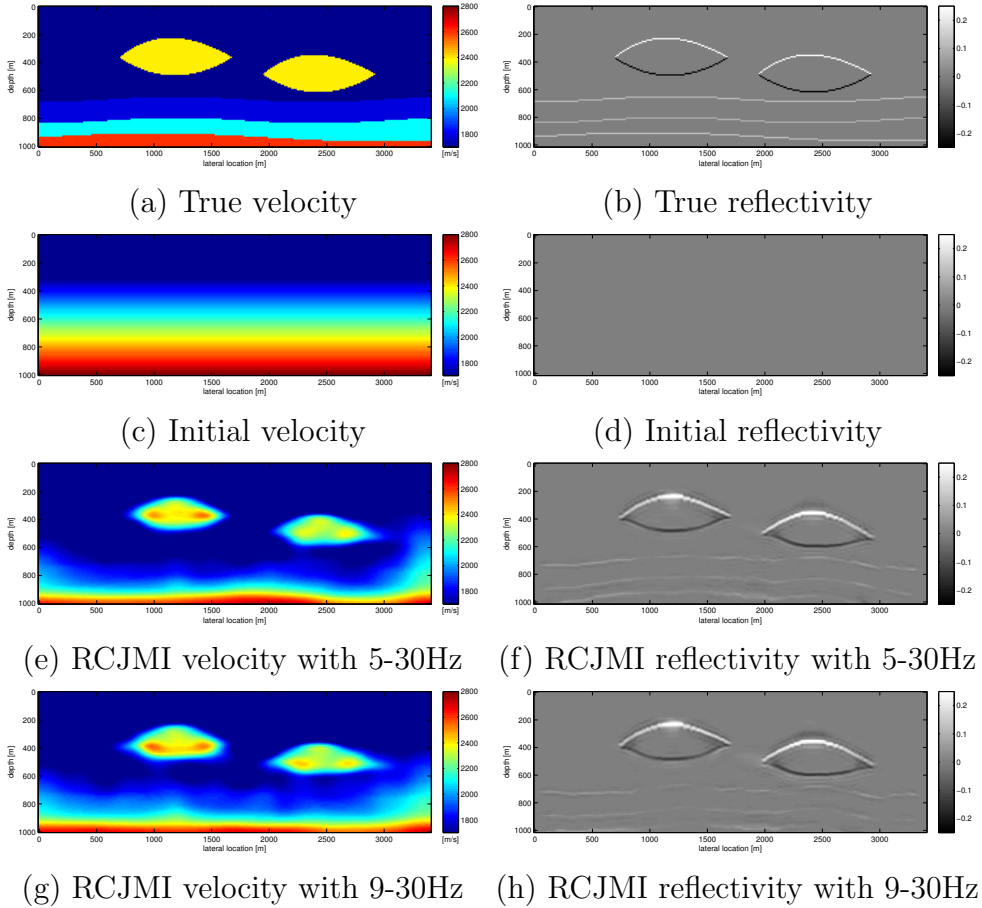


Figure 4.2: Reflectivity and velocity models in the example of the two geobodies model. (e)-(h) represent the results after 150 iterations.

not take into account the AVO effects and does not produce refracted waves, while the FD modeling handles the effects and refracted waves. To address these issues in the pre-processing before RCJMI, an offset limitation and an FK filter are imposed. The maximum offset in the data used for the inversion is 2000 m. The FK filter is applied to

suppress the influence of diving waves generated by the FD modeling. Figure 4.2 (c) and (d) show the initial velocity and reflectivity models for RCJMI. Figure 4.2 (e)-(h) represent the results after 150 RCJMI iterations with 5-30 Hz and 9-30 Hz. It can be seen that RCJMI with 9-30 Hz enables us to invert the accurate geobodies, even though the low frequency components less than 9 Hz are absent.

4.3 Surface amplitude correction via learning from synthetic models

This section describes a new surface amplitude correction framework to properly apply JMI to land seismic data and gives a numerical example to test the validity. As mentioned in the introduction, the aim of this amplitude correction is to reduce the influence of the amplitude variations caused by source/receiver response sensitivity, the difference of the features between the observed data and the simulated data by the used imaging scheme, and 3D propagation effects if some 2D modeling algorithm in the imaging scheme is applied to 2D seismic data. To correct such amplitude variations, an amplitude correction framework based on a learning process from some synthetic models is introduced.

■ 4.3.1 Method

In our proposed framework to estimate surface amplitudes, a synthetic model of the subsurface needs to be prepared to run a seismic modeling process and obtain simulated shot data, as shown in Fig. 4.3. Furthermore, source wavelets for the seismic modeling have to be estimated from the field data. The monochromatic wavefields measured in the field data $\vec{P}^-(z_0, x_{s,\xi}, \omega_f) \in \mathbb{C}^{N_r}$ is described by:

$$\vec{P}^-(z_0, x_{s,\xi}, \omega_f) \equiv [P^-(x_{r,1}, z_0, x_{s,\xi}, \omega_f), \dots, P^-(x_{r,N_r}, z_0, x_{s,\xi}, \omega_f)]^T, \quad (4.3.1)$$

where $x_{r,i}$ represents the receiver location at the i th receiver. Then, synthetic shot data $\vec{P}_{synt}^-(z_0, x_{s,\xi}, \omega_f) \in \mathbb{C}^{N_r}$ is generated by the seis-

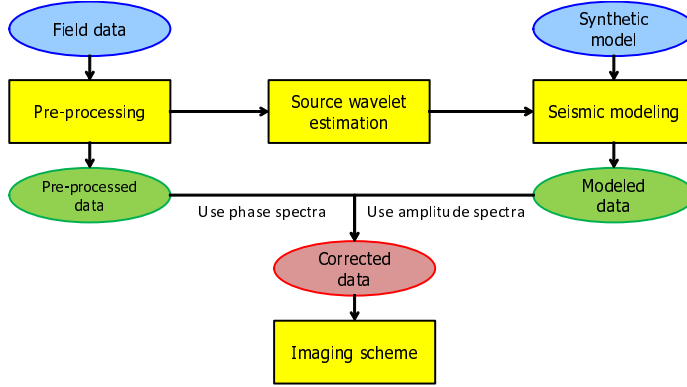


Figure 4.3: Workflow surface amplitude correction framework via learning from synthetic models.

mic modeling, the estimated source wavelets, and the synthetic model. Finally, combining the phase spectrum of the field data with the amplitude spectrum of the synthetic data, we obtain the corrected data $\vec{P}_{corr}^-(z_0, x_{s,\xi}, \omega_f) \in \mathbb{C}^{N_r}$:

$$P_{corr}^-(x_{r,i}, z_0, x_{s,\xi}, \omega_f) = |P_{synt}^-(x_{r,i}, z_0, x_{s,\xi}, \omega_f)| e^{j \arg[P^-(x_{r,i}, z_0, x_{s,\xi}, \omega_f)]}, \quad (4.3.2)$$

where $i = 1, 2, \dots, N_r$. This process means that the amplitude spectra obtained from the synthetic model are copied in each trace for the pre-processed field data. This amplitude correction framework has two major advantages. First, the amplitude variations caused by receiver response sensitivities can be completely eliminated by exploiting the amplitude spectra of the modeled data in this approach. If the amplitude spectra for the source wavelets are equalized, source response sensitivity is also mitigated in this procedure. Secondly, this framework enables us to fit the amplitude of real data to the used imaging scheme, because the same seismic modeling algorithm for the used imaging scheme can be utilized in the workflow. A disadvantage of this method is the uncertainty of the synthetic training models. This means that we have to prepare some plausible models for training to estimate amplitude spectra.

Since 2D RCJMI and so-called full wavefield migration (FWM) (Berkhout and Verschuur, 2011; Davydenko and Verschuur, 2017b), which is a migration algorithm based on FWMod for a fixed input velocity, are applied as an imaging scheme in this chapter, FWMod is used as the seismic modeling process in the workflow for the amplitude correction. Note that other modeling methods like FD modeling can be theoretically replaced in the workflow in the light of used imaging/inversion schemes (e.g. RTM or FWI).

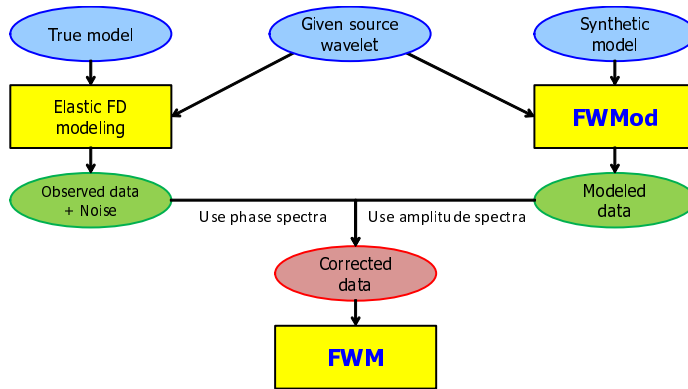


Figure 4.4: Workflow of our proposed the amplitude correction for the numerical example.

■ 4.3.2 Numerical experiment

A subset of the Middle-East land model used in the previous section is employed in this numerical example to test the proposed amplitude correction framework (Fig. 4.4), shown in Fig. 4.5 (a)-(d). In addition to the synthetic model for image estimation, three synthetic models for training are prepared to examine the dependency of training models for the proposed amplitude correction. As illustrated in Fig. 4.5 (e)-(h), the training model A and B are 1D layered models whose velocity values are different from the true P-wave velocity values (Fig. 4.5 (a)). The training model C (Fig. 4.5 (i) and (j)) is a 2D model with lateral

variations. Here, all synthetic reflectivity models are calculated by the given velocity models and the density models, which are computed by so-called Gardner's relation (Gardner et al., 1974). The receiver and source interval is 20 m and 80 m in this example, respectively.

To produce synthetic shot data for the true model (Fig. 4.5 (a)-(c)), we use 2D elastic FD modeling, which is different from FWMod. Note again that one of the differences between the elastic FD modeling and the standard FWMod that we use here is the existence of AVO effects, refracted waves, surface waves and converted waves. Furthermore, random noise with SNR=-10 dB is added in the generated synthetic data for the reason of imposing a realistic assumption of onshore seismic data. In order to investigate the influence for the difference of seismic modeling algorithms, the same source wavelets as true source wavelets are used to run seismic modeling for training in this example (see Fig. 4.4). Note that the pre-processing except the proposed amplitude correction is not applied for the elastic FD data. We perform FWM for a true velocity shown in Fig. 4.6 (a). The frequency range of 10-40 Hz and full offset of 7 km in the seismic data are used for the migration.

We show four migration results (Fig. 4.6 (b)-(e)) after 8 iterations: 1) FWM without any correction (Fig. 4.6 (b)) FWM with the proposed correction by training model A (Fig. 4.5 (c) and (f)) FWM with the proposed correction by training model B (Fig. 4.5 (g) and (h)) FWM with the proposed correction by training model C (Fig. 4.5 (i) and (j)). It can be seen that the migration result without the amplitude correction (Fig. 4.6 (b)) includes strong artifacts, especially in the near-surface region including the weathering layer, which are caused by strong random noise on the shot data and the mentioned difference of modeling algorithms between elastic FD modeling and FWMod. However, the improvement of the image around the weathering layer can be observed in the migration results with training model A, B and C (Fig. 4.6 (c), (d) and (e)), owing to the proposed amplitude correction, although there is a large difference of velocity values between the true P-wave velocity (Fig. 4.6 (a)) and the training velocity models A and B. On the other hands, the artifacts caused by the learning process for training model C with lateral variations seems to be slightly strong (Fig. 4.6 (e)), although

the velocity values are relatively accurate. Therefore, it is found that simple 1D training models seem to be more suitable for this example, and the difference of velocity values and the number of reflection layers in the training models does not have large influence on the final migration result in this example.

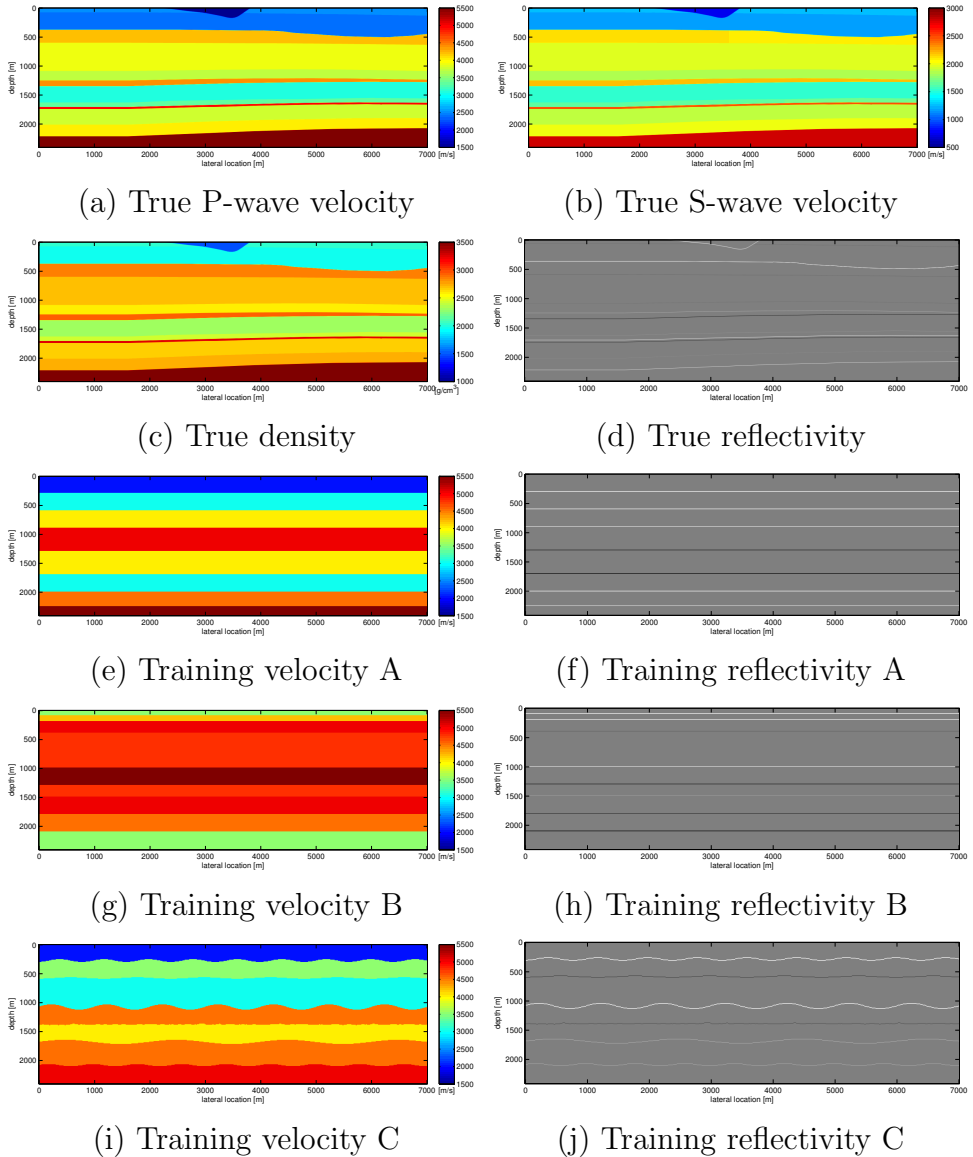
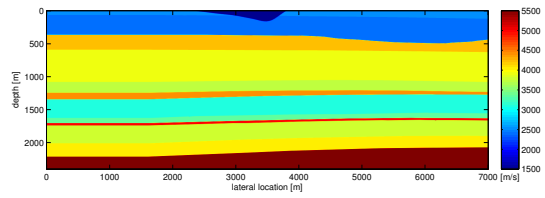
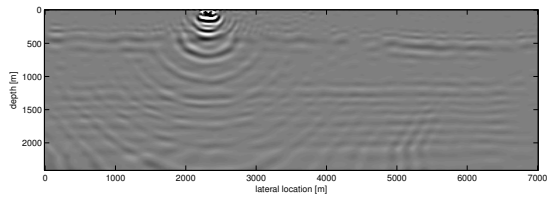


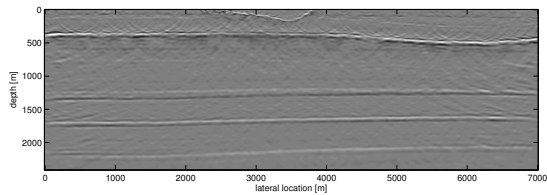
Figure 4.5: True models and training models in the example of the Middle-East model.



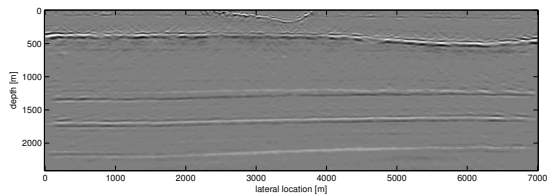
(a) Input velocity for migration



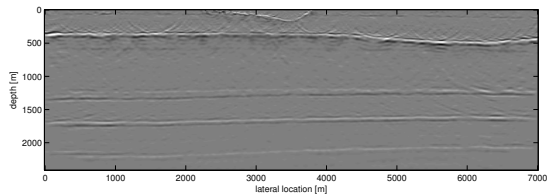
(b) Migration result without correction



(c) Migration result with training model A



(d) Migration result with training model B



(e) Migration result with training model C

Figure 4.6: Input velocity and results for FWM using different training datasets in the example of the Middle-East model.

4.4 Field data example

As a field data example, we use a 2D land seismic data provided by Saudi Aramco, which was used in an EAGE workshop on Near-Surface in 2005 (see e.g. Al-Ali and Verschuur, 2006). This data was acquired by a symmetric split receiver spread with a group interval of 30 m for both sources and receivers in Saudi Arabia. The 2D seismic line is a crooked line with a large difference in elevations (about maximum 140 m). A subset of the seismic line with relatively small elevations variations (about maximum 10 m) is chosen to neglect the elevation issue in this test. Vibroseis with a minimum frequency 10 Hz was employed for this seismic line. The feature of the subsurface in this survey is large and complex velocity variations.

■ 4.4.1 Pre-processing including surface amplitude correction

In the pre-processing, first, an FK filter is applied to suppress the surface/diving waves on the observed data (Fig. 4.7 (a)). Next, automatic gain control is employed to enhance the continuities of seismic events in the shot gathers and a mute is applied to remove artifacts caused by the AGC. Then, curvelet denoising is utilized to remove the rest of the surface waves. The source wavelets are simply estimated by taking the average amplitude spectrum of the pre-processed data and assigning a zero phase wavelet to it. Considering the results in the previous numerical example, we make two simple 1D layered models for training (Fig. 4.8). A synthetic shot dataset for the proposed amplitude correction is generated by FWMod with the estimated source wavelet, as illustrated in Fig. 4.9. The corrected shot gathers by training models A and B are illustrated in Fig. 4.7 (b) and (c), respectively.

■ 4.4.2 Full wavefield migration

First, we test FWM for this pre-processed and corrected field data. The frequency range of 10-60 Hz and a maximum offset of 3.27 km in the seismic data are used for FWM. We use the input velocity (Fig. 4.10

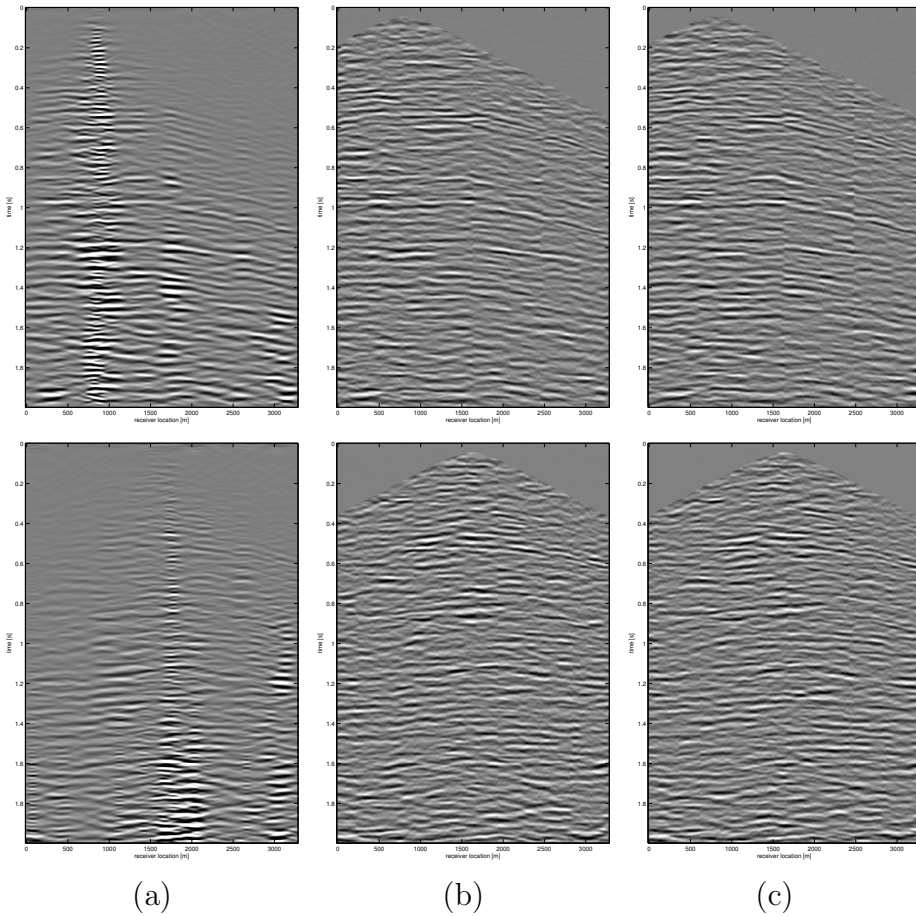


Figure 4.7: The comparison of the shot gathers after FK filter, the proposed amplitude correction with training model A and B in the field data example: (a) After FK filter, (b) After amplitude correction with training model A, (c) After amplitude correction with training model B.

(a)), which was obtained from the tomographic inversion in a prior study (Al-Ali and Verschuur, 2006), for FWM. The FWM result without any amplitude correction is shown in Fig. 4.10 (b), while Fig. 4.10 (c) and (d) represent the migration results via the proposed amplitude correc-

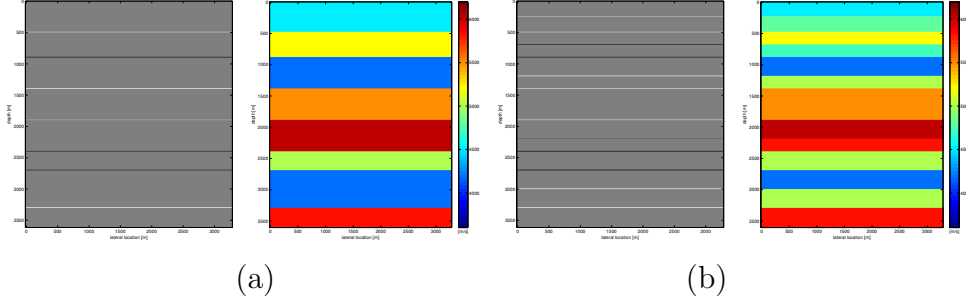


Figure 4.8: Training models in the field data example: (a) Training reflectivity and velocity A , (b) Training reflectivity and velocity B .

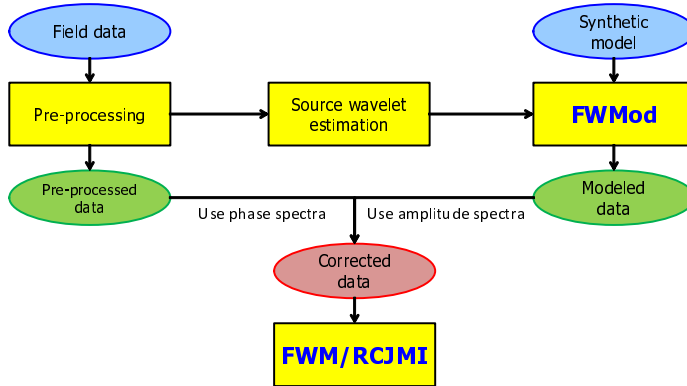


Figure 4.9: Workflow of our proposed amplitude correction for the field example.

tion with training model A and B , respectively. The same iteration number of 8 for FWM are applied in their computations. It can be seen that the corrected data by the proposed method provides better horizontal continuity of reflectivity (see Fig. 4.10 (c) and (d)), while several features of the seismic events shown in Fig. 4.10 (b) are preserved in

the results with the proposed method.

■ 4.4.3 Reflectivity-constrained joint migration inversion

Next, we perform RCJMI for the pre-processed and corrected field data to estimate both reflectivity and velocity model. For comparison, an initial velocity for FWM and RCJMI and the result of FWM without any amplitude correction are shown again in Fig. 4.11 (a) and (b). Figure 4.11 (c) and (d) illustrate the velocity and reflectivity models reconstructed after RCJMI without amplitude correction and Fig. 4.11 (e) and (f) show the velocity and reflectivity estimated by RCJMI with the amplitude correction by training model A. The number of iterations is 180 for both RCJMI results. Compared to the FWM reflectivity model, the RCJMI reflectivity models have better horizontal continuity, owing to the updated velocity via RCJMI. Furthermore, the proposed amplitude correction also provides the improved reflectivity image especially at shallow depth 100-700 m in the RCJMI results (Fig. 4.11 (d) and (f)). It can be seen that the artifacts around lateral location 2500-3000 m and depth 1500-2000 m in Fig. 4.11 (d) are reduced in the RCJMI reflectivity with the amplitude correction (Fig. 4.11 (f)).

Angle-domain common image gathers (de Bruin et al., 1990; Sava and Biondi, 2004) are generated at lateral location 500 m, 1000 m, 1500 m, 2000 m, 2500 m, and 3000 m in order to evaluate the accuracy of the velocity inverted by RCJMI with the amplitude correction, as shown in Fig. 4.12. The common image gathers are made with the shot data before the proposed amplitude correction process. Note that the flatness in the common image gathers approximately represents accurate velocity, although the gathers also include the artifacts caused by the low SN ratio of the original shot gathers. It can be seen that the flatness in the common image gathers generated by the RCJMI velocity has improved at almost all levels, especially at depth 2300 m and 2800 m. Therefore, it is found that RCJMI successfully updates the velocity model, even though the original field data does not include the low frequency components less than 10 Hz, which is generally critical for FWI. However, since the validity of the estimated velocity at the near

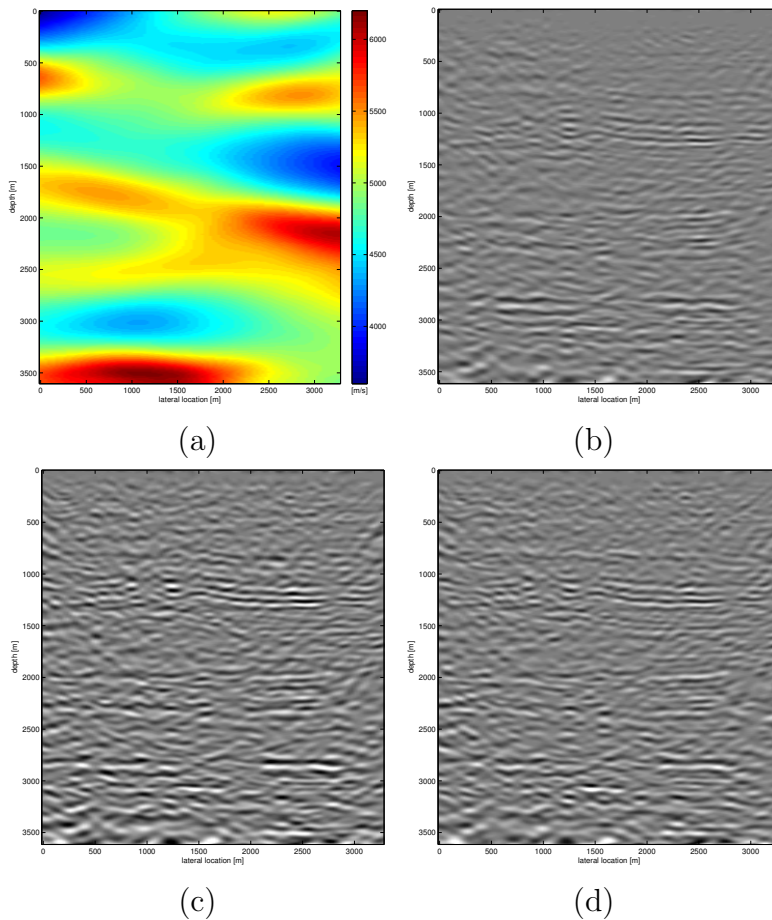


Figure 4.10: Input velocity and results for FWM in the field data example: (a) Input velocity A for FWM, (b) Migration result without correction, (c) Migration result with training model A , (d) Migration result with training model B .

surface (around 0-300 m) cannot be evaluated by this common image gathers due to the poor quality of the gathers, we discuss this point in the next section.

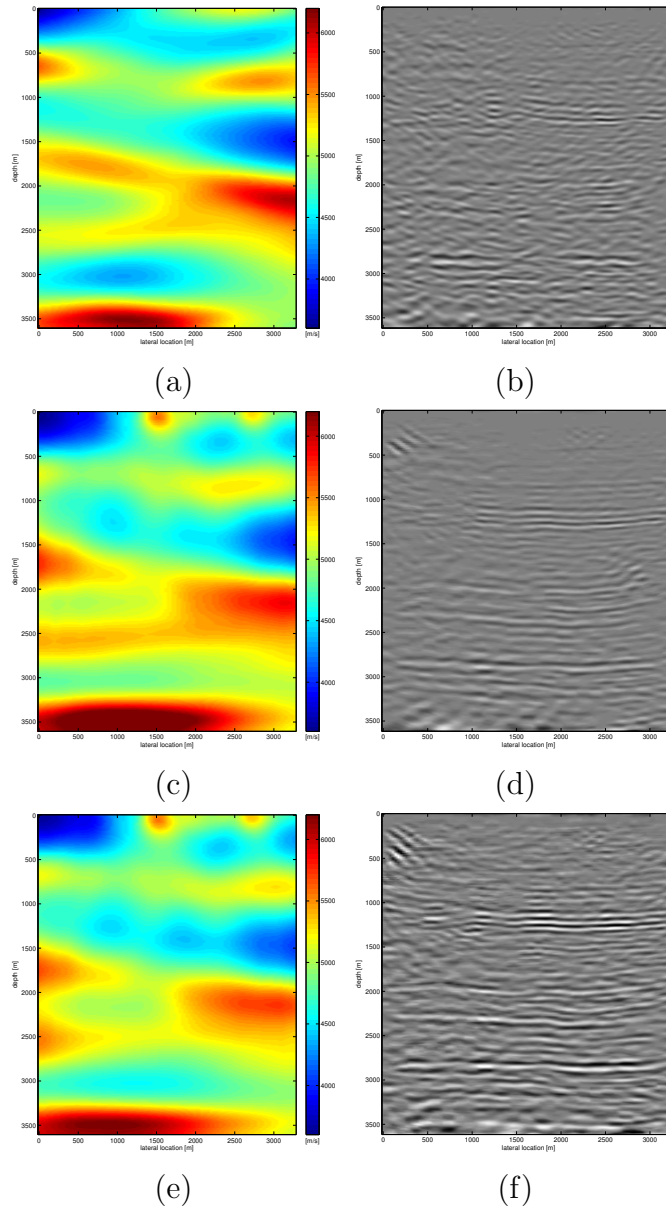
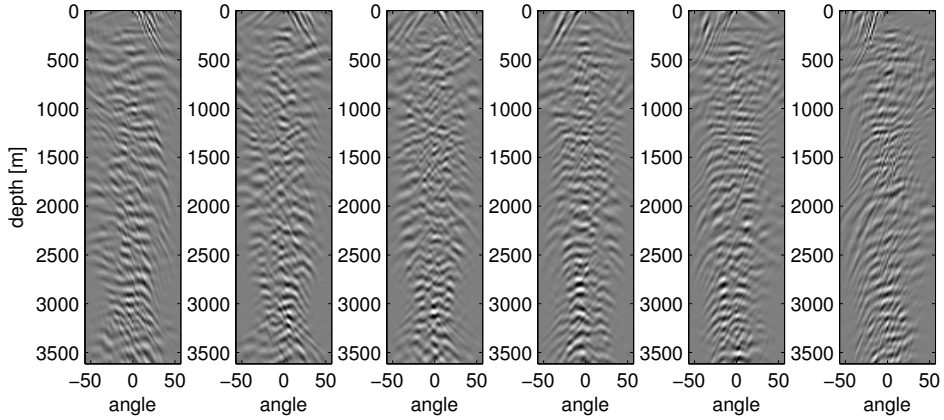
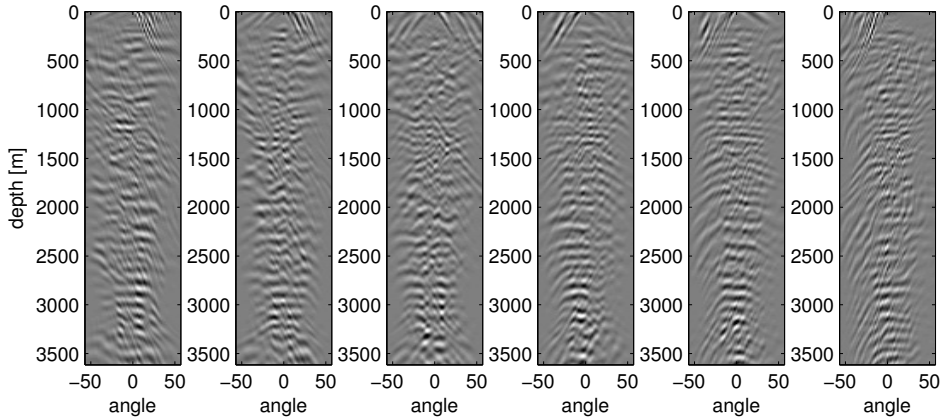


Figure 4.11: Input velocity and RCJMI results for the field data example: (a) Input velocity A for FWM and RCJMI, (b) FWM reflectivity without correction, (c) RCJMI velocity without correction, (d) RCJMI reflectivity without correction, (e) RCJMI velocity with training model A , (f) RCJMI reflectivity with training model A .



(a) Input velocity for RCJMI



(b) RCJMI velocity with training model A

Figure 4.12: The comparison of angle-domain common image gathers obtained with (a) the input velocity and (b) the RCJMI velocity. The lateral locations are 500 m, 1000 m, 1500 m, 2000 m, 2500 m, and 3000 m, respectively.

4.5 Discussion

■ 4.5.1 Initial velocity dependency of velocity estimation for near-surface anomalies

We investigate the validity of the estimated velocity by RCJMI at very shallow level of 0-300 m in the field data example. Another input velocity (B) model is prepared to examine the initial velocity dependency of the velocity estimation, as shown in Fig. 4.13 (a). This input velocity B is made from the original input velocity (A) through strong smoothing. Figure 4.13 (b)-(d) represent the FWM reflectivity without any amplitude correction, the RCJMI velocity with the proposed correction via training model A and the RCJMI reflectivity with the proposed correction via training model A, respectively. The number of iterations for the FWM and RCJMI is 8 and 180, which are the same values as in the previous results. The improvement of the reflectivity inverted by RCJMI can be also seen in the case of this input velocity B.

Figure 4.14 focuses on the comparison between input velocity models (A and B) and the estimated velocity models at the near-surface level of 0-500 m. It can be seen that the inverted velocity model from input velocity B (Fig. 4.14 (b)) also gives the same high and low velocity anomalies (see Fig. 4.14 (d)) as that from the input velocity velocity A, although the land data quality is poor compared to standard marine seismic data and low frequency components are absent. Hence, this estimated velocity anomalies at the near surface would be plausible, and they largely contribute to the improved image at the deeper levels.

■ 4.5.2 Surface amplitude correction based on learning process

The results of the shown synthetic and field data examples demonstrate that the proposed surface amplitude correction process can be a pragmatic approach for at least FWM and RCJMI. While the approach corrects the common amplitude variations for source/receiver response sensitivities and 3D propagation effects in the employed 2D

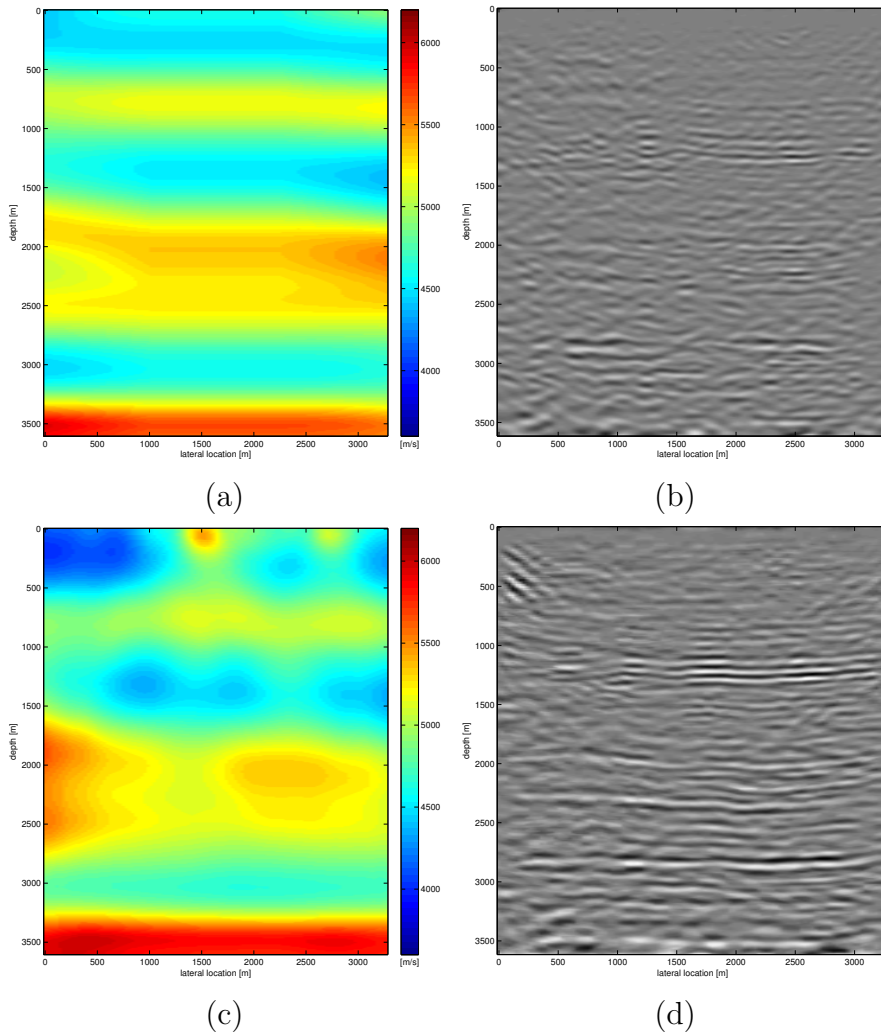


Figure 4.13: *Input velocity B and the results of FWM and RCJMI for the velocity: (a) Input velocity B for FWM and RCJMI, (b) FWM reflectivity without correction, (c) RCJMI velocity with training model A , (d) RCJMI reflectivity with training model A .*

seismic modeling process, it can suppress the influence of the intrinsic

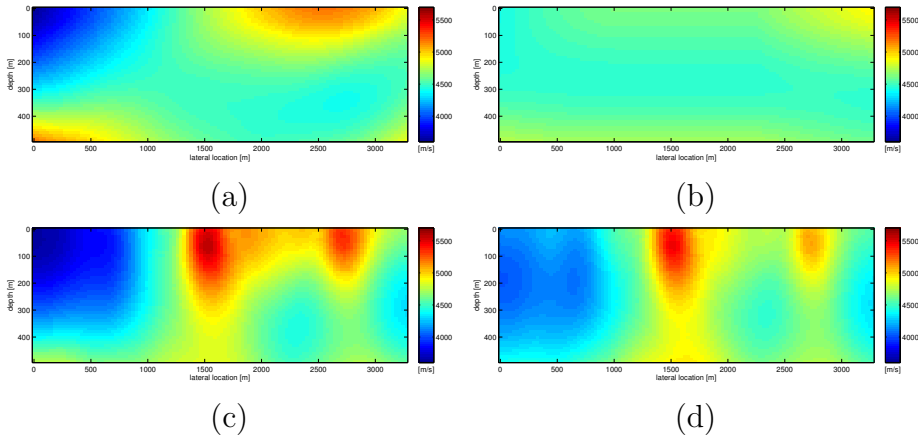


Figure 4.14: *Input velocity models and the estimated velocity models by RCJMI at depth 0-500 m: (a) Input velocity A for RCJMI, (b) Input velocity B for RCJMI, (c) RCJMI velocity for input velocity A, (d) RCJMI velocity for input velocity B. The amplitude corrected data by training model A is used for RCJMI.*

problems in the seismic modeling of the used imaging scheme. This feature to fit the observed data to the employed seismic modeling process is a significant point in the approach, because we might avoid to employ complex seismic modeling algorithms, which usually contribute to the high non-linearity in the inversion process. As a result, the reflectivity image estimated by the amplitude-corrected data could be helpful to enhance the effect of the reflectivity-constrained velocity estimation in RCJMI.

However, since this approach has a dependency on training models, we need to further investigate the way to make and choose the training models. If we have some well log in the seismic acquisition area, establishing a training model based on the well log might be a good option. Furthermore, we envision a ‘self re-training’ method that utilizes the reflectivity and velocity estimated by the used imaging/inversion scheme to construct training models.

4.6 Conclusions

We discuss the application of RCJMI for land synthetic and field data without the low frequency components. In the pre-processing, a novel surface amplitude correction framework based on learning from some synthetic model is proposed to reduce the difference of amplitude variations between the observed data and the simulated data by the seismic modeling in the used imaging scheme. The results for synthetic and field data examples demonstrated that RCJMI is capable of effectively estimating reflectivity and velocity models, even though the low frequency components of the observed data are absent and the data amplitudes are not fully consistent with the employed modeling method.

JMI including refracted/diving waves

5.1 Introduction

Seismic imaging is a significant technology to predict the image of the subsurface in several fields such as hydrocarbon exploration/production and civil engineering. One of the challenges in seismic imaging is the velocity estimation for the subsurface, especially complex structures with sharp contrasts. FWI is a commonly used inversion algorithm to provide high resolution velocity models through minimizing the residual between observed data and simulated data, which is computed by a suitable seismic forward modeling process. However, the solutions for FWI tend to converge to local minima (see e.g. Virieux and Operto, 2009) due to the non-linearity of the inverse problem, although recently studies have been reported to mitigate the local minima (e.g. Warner and Guasch, 2016; van Leeuwen and Herrmann, 2016).

JMI was proposed as one of the methods to reduce the non-linearity in FWI (Berkhout, 2012, see also chapter 2 and 3 of this thesis). JMI enables us to simultaneously estimate both velocity and reflectivity models by exploiting reflected waves including internal multiples and transmis-

sion effects. The seismic modeling algorithm in the JMI process is the FWMod (Berkhout and Verschuur, 2011; Berkhout, 2014a), which is a reflection modeling algorithm, including higher-order scattering and transmission effects, with similarities to the Bremmer series (Bremmer, 1951) in optics. Since a typical one-way propagation operator is utilized in standard FWMod, the propagation for very steep angles is challenging. Refractions and diving waves are also not taken into account in the standard FWMod process.

To address the dip limitation in FWMod, Davydenko and Verschuur (2013) introduced an imaging method based on so-called duplex waves, which describe propagation paths with a double reflection involving a reflecting base boundary and a near-vertical feature (Marmalyevskyy et al., 2005). Furthermore, the modeling was omni-directionally extended by an orthogonal wave extrapolation (as presented by Jia and Wu, 2009) to realize diving waves (Davydenko et al., 2014). In the orthogonal wave extrapolation, the wavefields are reconstructed by not only vertical wave extrapolation but also horizontal wave extrapolation. In this prior approach (Davydenko et al., 2014), however, the direction of orthogonal components in the scattered wavefields is not optimally handled.

Masaya and Verschuur (2017b) proposed a seismic modeling method based on an omni-directional approach to correctly deal with the direction and amplitude of the scattered wavefields and accurately generate refracted waves and diving waves, as well as reflected waves. In this method, vertical reflectivity, horizontal reflectivity, and velocity model grids are defined by their own coordinate positions in a so-called staggered grid fashion. Introducing a concept of intermediate propagation (e.g. down-rightgoing, up-leftgoing etc) between the horizontal and vertical reflectivity grid in the coordinate system of the orthogonal staggered grid enables us to correctly deal with the direction of the scattered wavefields from the physics of view. Since the amplitude scale of vertical and horizontal propagation is approximately corrected by using a forward modeling, internal multiples can be also generated in this modeling. However, this modeling method had still challenges to extend to reflectivity and velocity estimation. The major problem is that the use of the forward modeling-based scaling scheme causes a large increase in

the computational cost.

In this chapter, we discuss an improved seismic modeling method and present an omni-directional wavefield migration (OWM) and an omni-directional joint migration inversion (OJMI) algorithm based on this new forward modeling method. The amplitude scaling process is simplified in this modeling process by calculating the amplitude scale of horizontally propagated wavefields from that of vertically propagated wavefields in order to reduce the computational cost and enhance the accuracy of modeling. In addition to deriving a reflectivity and velocity update rule based on the horizontal propagation, horizontal reflectivity-constrained velocity estimation is also formulated in OJMI.

First, this chapter describes the proposed wavefield modeling method in section 5.2. Next, as an extension of this modeling process to migration, the OWM algorithm is discussed in section 5.3. Then, in order to extend to OJMI algorithm, the velocity estimation based on horizontal propagation and reflectivity constraint is stated in section 5.4. Finally, we draw discussion and conclusions in section 5.5 and 5.6.

5.2 Omni-directional wavefield modeling

■ 5.2.1 Omni-directional extension

In the omni-directional extension (Davydenko et al., 2014) of FW-Mod, not only vertical propagation but also horizontal propagation is calculated, as shown in Fig. 5.1 (b). Reflection operators $\mathbf{R}^\cap(x_m)$, $\mathbf{R}^\cup(x_m) \in \mathbb{R}^{N_z \times N_z}$ and transmission operators $\mathbf{T}^\pm(x_m) \in \mathbb{R}^{N_z \times N_z}$ are also defined in the horizontal propagation direction, indicated by argument x_m . However, as the reflectivity and velocity model in the omni-directional approach of Davydenko et al. (2014) was defined by the same grid, the direction and amplitude of the scattered wavefields cannot be correctly taken into account.

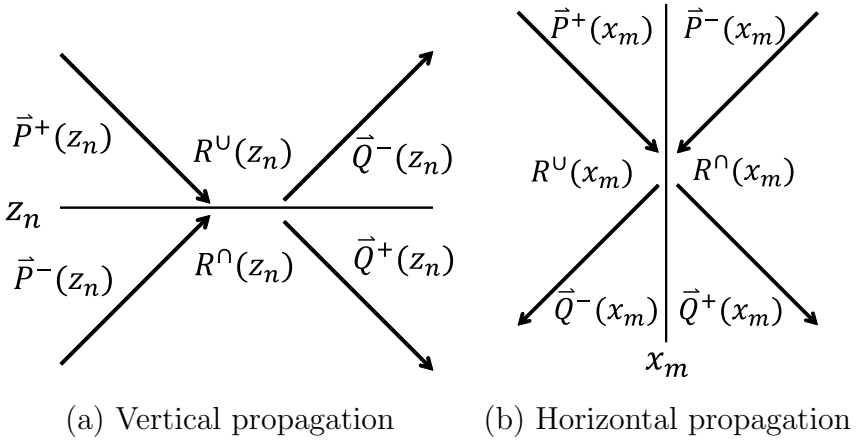


Figure 5.1: Propagation for omni-directional wavefields.

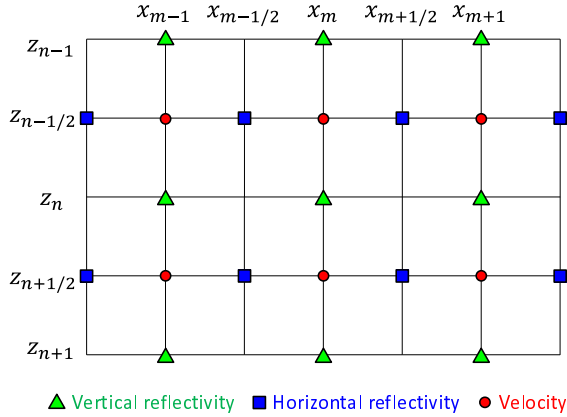


Figure 5.2: Orthogonal staggered grid.

■ 5.2.2 Vertical and horizontal propagation in staggered grid

In order to accurately address the direction and amplitude of the scattered wavefields, the orthogonal staggered grid illustrated in Fig. 5.2 is introduced in our proposed seismic modeling with an omni-directional

approach. The positions of the vertical reflectivity model $\mathbf{m}_r \in \mathbb{R}^{N_z \times (N_r+1)}$, the horizontal reflectivity model $\mathbf{m}_{hr} \in \mathbb{R}^{(N_z+1) \times N_r}$ and the velocity model $\mathbf{m}_c \in \mathbb{R}^{N_z \times N_r}$ are separately defined in this grid, which enables us to compute the intermediate propagation between the horizontal and the vertical reflectivity grid. Therefore, instead of equation (2.1.4) and (2.1.6) we can newly describe the following representation for the wavefields in the orthogonal staggered grid in FWMod:

$$\begin{aligned} \vec{Q}_v^+(z_n) &= \mathbf{T}^+(z_n)(\vec{P}_v^+(z_n) + \vec{P}_{right}^+(z_n) + \vec{P}_{left}^+(z_n)) \\ &+ \mathbf{R}^\cap(z_n)(\vec{P}_v^-(z_n) + \vec{P}_{right}^-(z_n) + \vec{P}_{left}^-(z_n)), \end{aligned} \quad (5.2.1)$$

$$\begin{aligned} \vec{Q}_v^-(z_n) &= \mathbf{T}^-(z_n)(\vec{P}_v^-(z_n) + \vec{P}_{right}^-(z_n) + \vec{P}_{left}^-(z_n)) \\ &+ \mathbf{R}^\cup(z_n)(\vec{P}_v^+(z_n) + \vec{P}_{right}^+(z_n) + \vec{P}_{left}^+(z_n)), \end{aligned} \quad (5.2.2)$$

$$\begin{aligned} \vec{Q}_h^+(x_m) &= \mathbf{T}^+(x_m)(\vec{P}_h^+(x_m) + \vec{P}_{down}^+(x_m)) \\ &+ \mathbf{R}^\cap(x_m)(\vec{P}_h^-(x_m) + \vec{P}_{down}^-(x_m)), \end{aligned} \quad (5.2.3)$$

$$\begin{aligned} \vec{Q}_h^-(x_m) &= \mathbf{T}^-(x_m)(\vec{P}_h^-(x_m) + \vec{P}_{down}^-(x_m)) \\ &+ \mathbf{R}^\cup(x_m)(\vec{P}_h^+(x_m) + \vec{P}_{down}^+(x_m)), \end{aligned} \quad (5.2.4)$$

where the meaning of each wavefields \vec{P}_*^\pm is shown in Fig. 5.3 and 5.4. The wavefields $\vec{Q}_h^\pm(x_m) \in \mathbb{C}^{N_z \times N_z}$ after the transmission and reflection at x_m propagate to the neighboring horizontal location $x_{m\pm 1}$ via the horizontal wave extrapolation, similar to the case of vertical wave extrapolation described in equation (2.1.8):

$$\vec{P}_h^\pm(x_{m\pm 1}) = \mathbf{W}^\pm(x_{m\pm 1}; x_m) \vec{Q}_h^\pm(x_m). \quad (5.2.5)$$

As illustrated in Fig. 5.3 and 5.4, in addition to downgoing, upgoing, rightgoing and leftgoing wavefield, 8 types of wavefields are calculated with a limited angle range, like down-rightgoing and left-upgoing wavefield. Computing the total 12 types of wavefields allows us to correctly handle the direction of the scattered wavefields.

■ 5.2.3 Angle wavefield decomposition

An angle wavefield decomposition process is introduced to realize the mentioned wavefields with limited angles. We employ an approach based

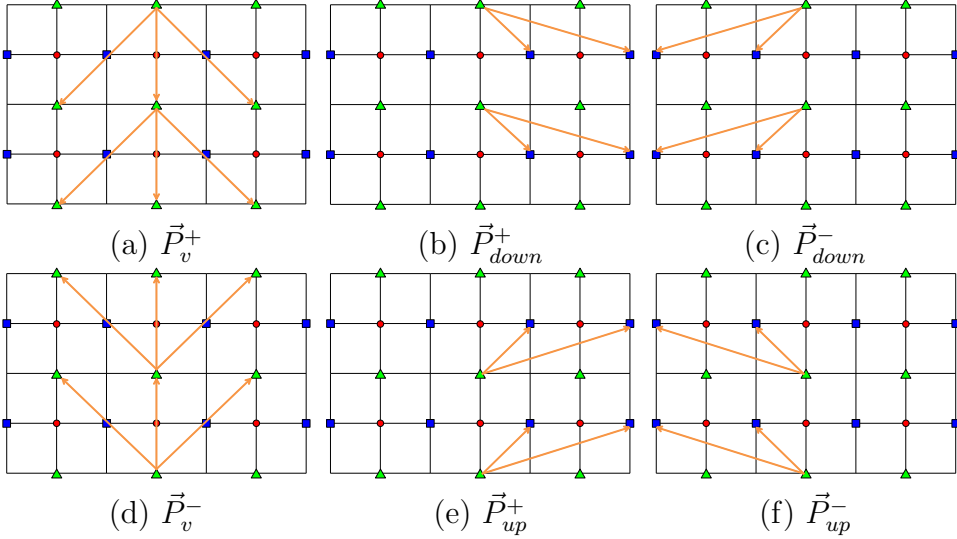


Figure 5.3: Definition of vertically propagated wavefields in the proposed modeling. (a) Vertically downgoing wavefields \vec{P}_v^+ . (b) Vertically down-rightgoing wavefields \vec{P}_{down}^+ . (c) Vertically down-leftgoing wavefields \vec{P}_{down}^- . (d) Vertically upgoing wavefields \vec{P}_v^- . (e) Vertically up-rightgoing wavefields \vec{P}_{up}^+ . (f) Vertically up-leftgoing wavefields \vec{P}_{up}^- .

on Poynting vectors (Yoon and Marfurt, 2004), which is capable of determining the angle of the propagated wavefields by the spatial first derivatives and the temporal first derivatives for the pressure wavefields in the space-time domain.

The x and z components of the Poynting vector for pressure wavefield $p(x, z, t)$ at a grid (x, z) are defined by:

$$Y_x(x, z, t; p) \equiv -\frac{\partial p(x, z, t)}{\partial t} \frac{\partial p(x, z, t)}{\partial x} \left[\left| \frac{\partial p(x, z, t)}{\partial t} \frac{\partial p(x, z, t)}{\partial x} \right| + \epsilon \right]^{-1}, \quad (5.2.6)$$

$$Y_z(x, z, t; p) \equiv -\frac{\partial p(x, z, t)}{\partial t} \frac{\partial p(x, z, t)}{\partial z} \left[\left| \frac{\partial p(x, z, t)}{\partial t} \frac{\partial p(x, z, t)}{\partial z} \right| + \epsilon \right]^{-1}, \quad (5.2.7)$$

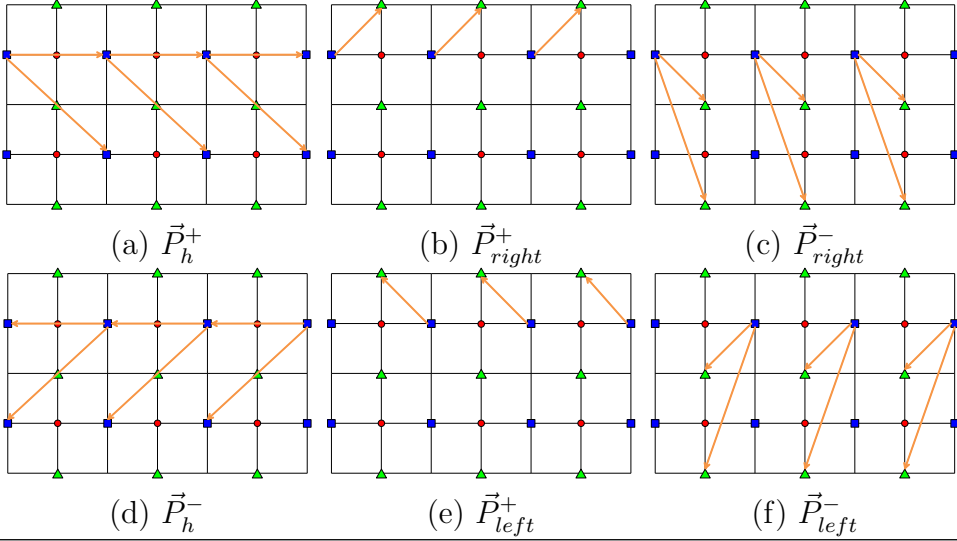


Figure 5.4: Definition of horizontally propagated wavefields in the proposed modeling. (a) Horizontally rightgoing wavefields \vec{P}_h^+ . (b) Horizontally right-downgoing wavefields \vec{P}_{right}^+ . (c) Horizontally right-upgoing wavefields \vec{P}_{right}^- . (d) Horizontally leftgoing wavefields \vec{P}_h^- . (e) Horizontally left-downgoing wavefields \vec{P}_{left}^+ . (f) Horizontally left-upgoing wavefields \vec{P}_{left}^- .

where $\epsilon(\sim 0)$ represents a stability parameter. On the basis of the components of the Poynting vector Y_x and Y_z , the down-rightgoing, down-leftgoing, up-rightgoing, and up-leftgoing wavefields are described by:

$$p_{down}^+(x, z, t) = \begin{cases} Y_x(x, z, t; p_v^+) p_v^+(x, z, t) & \text{for } Y_x(x, z, t; p_v^+) > 0 \\ 0 & \text{for } Y_x(x, z, t; p_v^+) \leq 0, \end{cases} \quad (5.2.8)$$

$$p_{down}^-(x, z, t) = \begin{cases} -Y_x(x, z, t; p_v^+) p_v^+(x, z, t) & \text{for } Y_x(x, z, t; p_v^+) < 0 \\ 0 & \text{for } Y_x(x, z, t; p_v^+) \geq 0, \end{cases} \quad (5.2.9)$$

$$p_{up}^+(x, z, t) = \begin{cases} Y_x(x, z, t; p_v^-)p_v^-(x, z, t) & \text{for } Y_x(x, z, t; p_v^-) > 0 \\ 0 & \text{for } Y_x(x, z, t; p_v^-) \leq 0, \end{cases} \quad (5.2.10)$$

$$p_{up}^-(x, z, t) = \begin{cases} -Y_x(x, z, t; p_v^-)p_v^-(x, z, t) & \text{for } Y_x(x, z, t; p_v^-) < 0 \\ 0 & \text{for } Y_x(x, z, t; p_v^-) \geq 0, \end{cases} \quad (5.2.11)$$

The right-downgoing, right-upgoing, left-downgoing, and left-upgoing wavefields are also expressed by:

$$p_{right}^+(x, z, t) = \begin{cases} Y_z(x, z, t; p_h^+)p_h^+(x, z, t) & \text{for } Y_z(x, z, t; p_h^+) > 0 \\ 0 & \text{for } Y_z(x, z, t; p_h^+) \leq 0, \end{cases} \quad (5.2.12)$$

$$p_{right}^-(x, z, t) = \begin{cases} -Y_z(x, z, t; p_h^+)p_h^+(x, z, t) & \text{for } Y_z(x, z, t; p_h^+) < 0 \\ 0 & \text{for } Y_z(x, z, t; p_h^+) \geq 0, \end{cases} \quad (5.2.13)$$

$$p_{left}^+(x, z, t) = \begin{cases} Y_z(x, z, t; p_h^-)p_h^-(x, z, t) & \text{for } Y_z(x, z, t; p_h^-) > 0 \\ 0 & \text{for } Y_z(x, z, t; p_h^-) \leq 0, \end{cases} \quad (5.2.14)$$

$$p_{left}^-(x, z, t) = \begin{cases} -Y_z(x, z, t; p_h^-)p_h^-(x, z, t) & \text{for } Y_z(x, z, t; p_h^-) < 0 \\ 0 & \text{for } Y_z(x, z, t; p_h^-) \geq 0, \end{cases} \quad (5.2.15)$$

These representations give angle-based separated wavefields, as shown for the example in Fig. 5.5.

Note that each propagation with limited angle of 90 degrees instead of around 180 degrees for downgoing, upgoing, rightgoing, and leftgoing wavefields is computed in order to minimize the overlap of waves between the vertical and the horizontal propagation. However, the overlap is not completely avoided in this process.

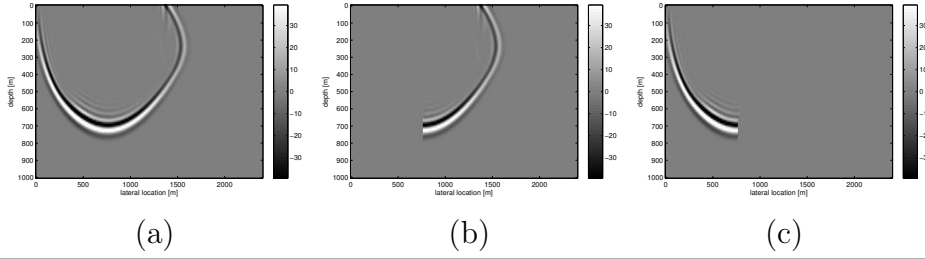


Figure 5.5: An example of the angle wavefield decomposition by Poynting vectors: (a) Original wavefield, (b) Separated wavefield with right direction, (c) Separated wavefield with left direction.

■ 5.2.4 Amplitude scaling

Some amplitude scaling is required to conserve the energy of the wavefields generated by vertical and horizontal propagation because there is a difference of amplitude scale between vertically and horizontally propagated wavefields, due to separately defining the vertical and horizontal reflectivity grid.

An approximate scaling process to correct the amplitude of horizontally propagated wavefields from vertically propagated wavefields is utilized to address this problem, as illustrated in Fig. 5.6. Let $\mathbf{P}_h^\pm \in \mathbb{C}^{N_z \times (N_r+1) \times N_\omega}$ be rightgoing and leftgoing wavefields on the horizontal reflectivity grid in the frequency domain, and $\mathbf{P}_v^+ \in \mathbb{C}^{(N_z+1) \times N_r \times N_\omega}$ be downgoing wavefields on the vertical reflectivity grid in the frequency domain. The amplitude scaling for horizontally propagated wavefields is described by:

$$\mathbf{P}_h^\pm \leftarrow \frac{\sqrt{\frac{1}{N_z+1} \frac{1}{N_r} \frac{1}{N_\omega} \sum^{N_z+1} \sum^{N_r} \sum^{N_\omega} (\mathbf{P}_v^+)^2}}{\sqrt{\frac{1}{N_z} \frac{1}{N_r+1} \frac{1}{N_\omega} \sum^{N_z} \sum^{N_r+1} \sum^{N_\omega} (\mathbf{P}_h^\pm)^2}} \mathbf{P}_h^\pm, \quad (5.2.16)$$

where indicates that the root-mean-square value of the amplitude spectra for rightgoing and leftgoing wavefields is scaled by that for downgoing wavefields \mathbf{P}_v^+ at every depth, spatial location and frequency. This

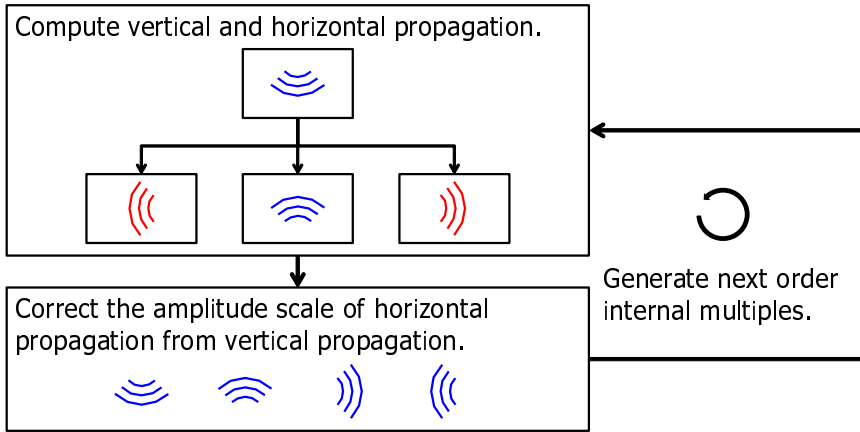


Figure 5.6: Schematic workflow for the scaling in the proposed modeling process. Note that the difference in color for propagation represents the difference of the amplitude scale.

process is an approximation to fit the amplitude scale of rightgoing and leftgoing wavefields to downgoing wavefields. Finally, the procedure to calculate the wavefields in the proposed modeling process is summarized in algorithm 3-6. Note that the angle wavefield decomposition is applied in the time domain, because a median filter for the components of the Poynting vectors is employed in the time domain in order to enhance the accuracy of the wave decomposition for the practical implementation.

Algorithm 3 Calculation for downgoing wavefields in the proposed modeling method.

Input: $[\vec{P}_v^-(z_0), \dots, \vec{P}_v^-(z_{N_z})]$, $[\vec{P}_{right}^\pm(z_0), \dots, \vec{P}_{right}^\pm(z_{N_z})]$, $[\vec{P}_{left}^\pm(z_0), \dots, \vec{P}_{left}^\pm(z_{N_z})]$,
 $[\mathbf{T}^+(z_0), \dots, \mathbf{T}^+(z_{N_z})]$, $[\mathbf{R}^\cap(z_0), \dots, \mathbf{R}^\cap(z_{N_z})]$, $[\mathbf{W}^+(z_1; z_0), \dots, \mathbf{W}^+(z_{N_z}; z_{N_z-1})]$,
 $[\mathbf{W}^+(z_{\frac{1}{2}}; z_0), \dots, \mathbf{W}^+(z_{N_z-\frac{1}{2}}; z_{N_z-1})]$, $\vec{S}^+(z_0)$

Output: $[\vec{P}_v^+(z_0), \dots, \vec{P}_v^+(z_{N_z})]$, $[\vec{P}_{down}^\pm(z_{\frac{1}{2}}), \dots, \vec{P}_{down}^\pm(z_{N_z-\frac{1}{2}})]$

- 1: $\vec{P}_v^+(z_0) = 0$
- 2: **for** $n = 0 \rightarrow N_z - 1$ **do**
- 3: $\vec{P}_{vert}^-(z_n) = \vec{P}_v^-(z_n) + \vec{P}_{right}^-(z_n) + \vec{P}_{left}^-(z_n)$
- 4: **if** $n = 0$ **then**
- 5: $\vec{Q}_v^+(z_n) = \vec{S}^+(z_0) + \mathbf{T}^+(z_n)(\vec{P}_v^+(z_n) + \vec{P}_{right}^+(z_n) + \vec{P}_{left}^+(z_n)) + \mathbf{R}^\cap(z_n)\vec{P}_{vert}^-(z_n)$
- 6: **else**
- 7: $\vec{Q}_v^+(z_n) = \mathbf{T}^+(z_n)(\vec{P}_v^+(z_n) + \vec{P}_{right}^+(z_n) + \vec{P}_{left}^+(z_n)) + \mathbf{R}^\cap(z_n)\vec{P}_{vert}^-(z_n)$
- 8: **end if**
- 9: $\vec{P}_v^+(z_{n+1}) = \mathbf{W}^+(z_{n+1}; z_n)\vec{Q}_v^+(z_n)$
- 10: $\vec{P}_v^+(z_{n+\frac{1}{2}}) = \mathbf{W}^+(z_{n+\frac{1}{2}}; z_n)\vec{Q}_v^+(z_n)$
- 11: **end for**
- 12: $\mathbf{p}_v^+ \leftarrow$ IFFT $[\mathbf{P}_v^+]$, where $\mathbf{P}_v^+ \equiv [\vec{P}_v^+(z_{\frac{1}{2}}), \vec{P}_v^+(z_{1+\frac{1}{2}}), \dots, \vec{P}_v^+(z_{N_z-\frac{1}{2}})]$
- 13: $\mathbf{p}_{down}^\pm \leftarrow$ AngleDecomposition $[\mathbf{p}_v^+]$ by eq. (5.2.8) and (5.2.9)
- 14: $\mathbf{P}_{down}^\pm \leftarrow$ FFT $[\mathbf{p}_{down}^\pm]$, where $\mathbf{P}_{down}^\pm \equiv [\vec{P}_{down}^\pm(z_{\frac{1}{2}}), \vec{P}_{down}^\pm(z_{1+\frac{1}{2}}), \dots, \vec{P}_{down}^\pm(z_{N_z-\frac{1}{2}})]$

Algorithm 4 Calculation for upgoing wavefields in the proposed modeling method.

Input: $[\vec{P}_v^+(z_0), \dots, \vec{P}_v^+(z_{N_z})]$, $[\vec{P}_{right}^\pm(z_0), \dots, \vec{P}_{right}^\pm(z_{N_z})]$, $[\vec{P}_{left}^\pm(z_0), \dots, \vec{P}_{left}^\pm(z_{N_z})]$,
 $[\mathbf{T}^-(z_0), \dots, \mathbf{T}^-(z_{N_z})]$, $[\mathbf{R}^\cup(z_0), \dots, \mathbf{R}^\cup(z_{N_z})]$, $[\mathbf{W}^-(z_0; z_1), \dots, \mathbf{W}^-(z_{N_z-1}; z_{N_z})]$,
 $[\mathbf{W}^-(z_{\frac{1}{2}}; z_1), \dots, \mathbf{W}^-(z_{N_z-\frac{1}{2}}; z_{N_z})]$

Output: $[\vec{P}_v^-(z_0), \dots, \vec{P}_v^-(z_{N_z})]$, $[\vec{P}_{up}^\pm(z_{\frac{1}{2}}), \dots, \vec{P}_{up}^\pm(z_{N_z-\frac{1}{2}})]$

- 1: $\vec{P}_v^-(z_{N_z}) = 0$
- 2: **for** $n = N_z \rightarrow 1$ **do**
- 3: $\vec{P}_{vert}^+(z_n) = \vec{P}_v^+(z_n) + \vec{P}_{right}^+(z_n) + \vec{P}_{left}^+(z_n)$
- 4: $\vec{Q}_v^-(z_n) = \mathbf{T}^-(z_n)(\vec{P}_v^-(z_n) + \vec{P}_{right}^-(z_n) + \vec{P}_{left}^-(z_n)) + \mathbf{R}^\cup(z_n)\vec{P}_{vert}^+(z_n)$
- 5: $\vec{P}_v^-(z_{n-1}) = \mathbf{W}^-(z_{n-1}; z_n)\vec{Q}_v^-(z_n)$
- 6: $\vec{P}_v^-(z_{n-\frac{1}{2}}) = \mathbf{W}^-(z_{n-\frac{1}{2}}; z_n)\vec{Q}_v^-(z_n)$
- 7: **end for**
- 8: $\mathbf{p}_v^- \leftarrow$ IFFT $[\mathbf{P}_v^-]$, where $\mathbf{P}_v^- \equiv [\vec{P}_v^-(z_{\frac{1}{2}}), \vec{P}_v^-(z_{1+\frac{1}{2}}), \dots, \vec{P}_v^-(z_{N_z-\frac{1}{2}})]$
- 9: $\mathbf{p}_{up}^\pm \leftarrow$ AngleDecomposition $[\mathbf{p}_v^-]$ by eq. (5.2.10) and (5.2.11)
- 10: $\mathbf{P}_{up}^\pm \leftarrow$ FFT $[\mathbf{p}_{up}^\pm]$, where $\mathbf{P}_{up}^\pm \equiv [\vec{P}_{up}^\pm(z_{\frac{1}{2}}), \vec{P}_{up}^\pm(z_{1+\frac{1}{2}}), \dots, \vec{P}_{up}^\pm(z_{N_z-\frac{1}{2}})]$

Algorithm 5 Calculation for rightgoing wavefields in the proposed modeling method.

Input: $[\vec{P}_h^-(x_0), \dots, \vec{P}_h^-(x_{N_r})]$, $[\vec{P}_{down}^\pm(x_0), \dots, \vec{P}_{down}^\pm(x_{N_r})]$, $[\mathbf{T}^+(x_0), \dots, \mathbf{T}^+(x_{N_r})]$,
 $[\mathbf{R}^\cap(x_0), \dots, \mathbf{R}^\cap(x_{N_r})]$, $[\mathbf{W}^+(x_0; x_1), \dots, \mathbf{W}^+(x_{N_r-1}; x_{N_r})]$, $[\mathbf{W}^+(x_{\frac{1}{2}}; x_1), \dots,$
 $\mathbf{W}^+(x_{N_r-\frac{1}{2}}; x_{N_r-1})]$

Output: $[\vec{P}_h^+(x_0), \dots, \vec{P}_h^+(x_{N_r})]$, $[\vec{P}_{right}^\pm(x_{\frac{1}{2}}), \dots, \vec{P}_{right}^\pm(x_{N_r-\frac{1}{2}})]$

- 1: $\vec{P}_h^+(x_0) = 0$
 - 2: **for** $m = 0 \rightarrow N_r - 1$ **do**
 - 3: $\vec{P}_{hori}^-(x_m) = \vec{P}_h^-(x_m) + \vec{P}_{down}^-(x_m)$
 - 4: $\vec{Q}_h^+(x_m) = \mathbf{T}^+(x_m)(\vec{P}_h^+(x_m) + \vec{P}_{down}^+(x_m)) + \mathbf{R}^\cap(x_m)\vec{P}_{hori}^-(x_m)$
 - 5: $\vec{P}_h^+(x_{m+1}) = \mathbf{W}^+(x_{m+1}; x_m)\vec{Q}_h^+(x_m)$
 - 6: $\vec{P}_h^+(x_{m+\frac{1}{2}}) = \mathbf{W}^+(x_{m+\frac{1}{2}}; x_m)\vec{Q}_h^+(x_m)$
 - 7: **end for**
 - 8: $\mathbf{P}_h^+ \leftarrow \text{AmplitudeScaling} [\mathbf{P}_h^+]$ by eq. (5.2.16)
 - 9: $\mathbf{p}_h^+ \leftarrow \text{IFFT} [\mathbf{P}_h^+]$, where $\mathbf{P}_h^+ \equiv [\vec{P}_h^+(x_{\frac{1}{2}}), \vec{P}_h^+(x_{1+\frac{1}{2}}), \dots, \vec{P}_h^+(x_{N_r-\frac{1}{2}})]$
 - 10: $\mathbf{p}_{right}^\pm \leftarrow \text{AngleDecomposition} [\mathbf{p}_h^+]$ by eq. (5.2.12) and (5.2.13)
 - 11: $\mathbf{P}_{right}^\pm \leftarrow \text{FFT} [\mathbf{p}_{right}^\pm]$, where $\mathbf{P}_{right}^\pm \equiv [\vec{P}_{right}^\pm(x_{\frac{1}{2}}), \vec{P}_{right}^\pm(x_{1+\frac{1}{2}}), \dots, \vec{P}_{right}^\pm(x_{N_r-\frac{1}{2}})]$
-

Algorithm 6 Calculation for leftgoing wavefields in the proposed modeling method.

Input: $[\vec{P}_h^+(x_0), \dots, \vec{P}_h^+(x_{N_r})]$, $[\vec{P}_{down}^\pm(x_0), \dots, \vec{P}_{down}^\pm(x_{N_r})]$, $[\mathbf{T}^-(x_0), \dots, \mathbf{T}^-(x_{N_r})]$,
 $[\mathbf{R}^\cup(x_0), \dots, \mathbf{R}^\cup(x_{N_r})]$, $[\mathbf{W}^-(x_0; x_1), \dots, \mathbf{W}^-(x_{N_r-1}; x_{N_r})]$, $[\mathbf{W}^-(x_{\frac{1}{2}}; x_1), \dots,$
 $\mathbf{W}^-(x_{N_r-\frac{1}{2}}; x_{N_r})]$

Output: $[\vec{P}_h^-(x_0), \dots, \vec{P}_h^-(x_{N_r})]$, $[\vec{P}_{left}^\pm(x_{\frac{1}{2}}), \dots, \vec{P}_{left}^\pm(x_{N_r-\frac{1}{2}})]$

- 1: $\vec{P}_h^-(x_{N_r}) = 0$
 - 2: **for** $m = N_r \rightarrow 1$ **do**
 - 3: $\vec{P}_{hori}^+(x_m) = \vec{P}_h^+(x_m) + \vec{P}_{down}^+(x_m)$
 - 4: $\vec{Q}_h^-(x_m) = \mathbf{T}^-(x_m)(\vec{P}_h^-(x_m) + \vec{P}_{down}^-(x_m)) + \mathbf{R}^\cup(x_m)\vec{P}_{hori}^+(x_m)$
 - 5: $\vec{P}_h^-(x_{m-1}) = \mathbf{W}^-(x_{m-1}; x_m)\vec{Q}_h^-(x_m)$
 - 6: $\vec{P}_h^-(x_{m-\frac{1}{2}}) = \mathbf{W}^-(x_{m-\frac{1}{2}}; x_m)\vec{Q}_h^-(x_m)$
 - 7: **end for**
 - 8: $\mathbf{P}_h^- \leftarrow \text{AmplitudeScaling} [\mathbf{P}_h^-]$ by eq. (5.2.16)
 - 9: $\mathbf{p}_h^- \leftarrow \text{IFFT} [\mathbf{P}_h^-]$, where $\mathbf{P}_h^- \equiv [\vec{P}_h^-(x_{\frac{1}{2}}), \vec{P}_h^-(x_{1+\frac{1}{2}}), \dots, \vec{P}_h^-(x_{N_r-\frac{1}{2}})]$
 - 10: $\mathbf{p}_{left}^\pm \leftarrow \text{AngleDecomposition} [\mathbf{p}_h^-]$ by eq. (5.2.14) and (5.2.15)
 - 11: $\mathbf{P}_{left}^\pm \leftarrow \text{FFT} [\mathbf{p}_{left}^\pm]$, where $\mathbf{P}_{left}^\pm \equiv [\vec{P}_{left}^\pm(x_{\frac{1}{2}}), \vec{P}_{left}^\pm(x_{1+\frac{1}{2}}), \dots, \vec{P}_{left}^\pm(x_{N_r-\frac{1}{2}})]$
-

■ 5.2.5 Numerical examples

We evaluate the performance of our proposed modeling through two numerical examples.

Example 1: Smooth variation model

The first example is a 2D model including a smoothed high-velocity and high-density anomaly at shallow depth, as shown in Fig. 5.7. The aim of this example is to investigate the propagation of diving waves. The grid size of the velocity, vertical reflectivity and horizontal reflectivity is 10m. Synthetic shot data is generated by acoustic FD modeling, conventional FWMod, and our proposed omnidirectional modeling process to compare their results. The data is modeled using a Ricker wavelet centered at 20 Hz. The acoustic FD modeling algorithm is 2nd order in time and 4th order in space (staggered grid). FWMod and the proposed modeling compute only primaries in the synthetic data in order to focus on the propagation of diving waves.

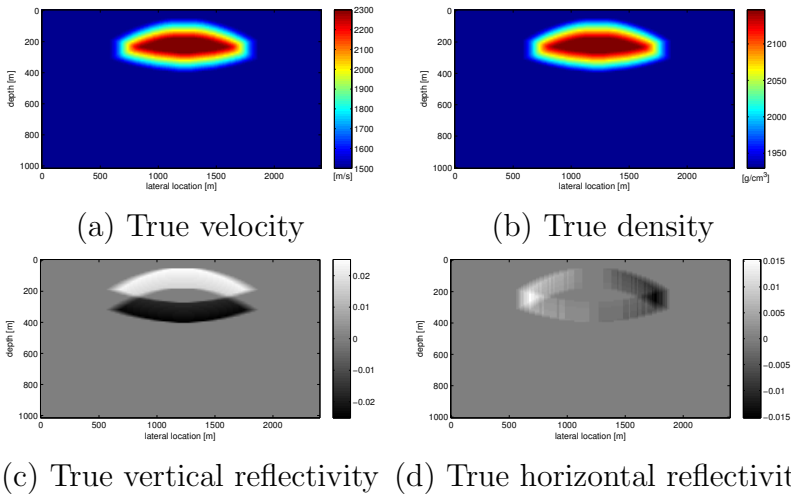


Figure 5.7: True velocity, density, and reflectivity models in the first example.

The snapshots of the propagated wavefields generated by each seismic modeling method are shown in Fig. 5.8. In Fig. 5.8 (c), diving waves are visible in the propagated wavefields produced by the proposed modeling (lower row), although conventional FWMod (middle row) does not handle the diving waves.

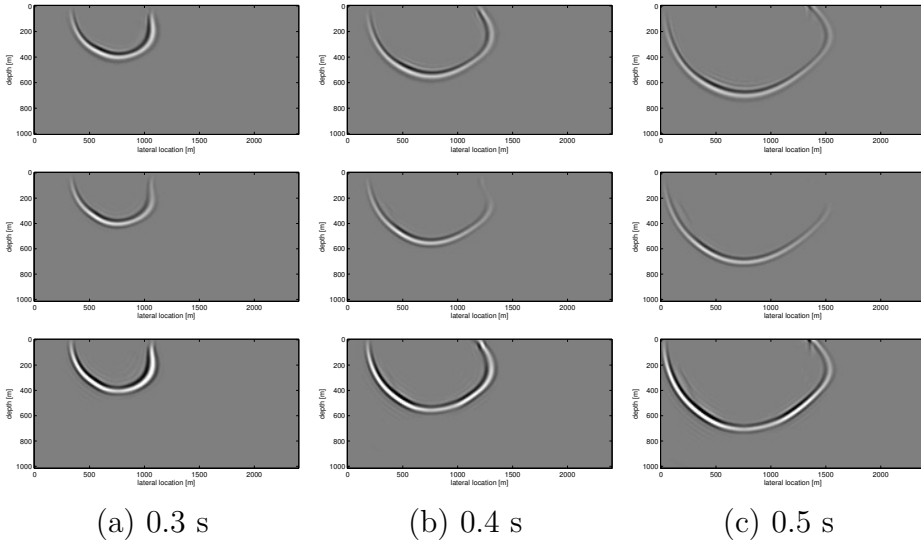


Figure 5.8: The comparison of snapshots generated by FD modeling (top row), conventional FWMod (middle row), and the proposed modeling (lower row) at 0.3 s, 0.4 s, and 0.5 s in the first example. The source is located at lateral location 700 m. The wavefields in the proposed modeling represent the total wavefields in the vertical reflectivity grid.

Example 2: Near-surface model including a weathering layer

The second example is a more realistic 2D model including a low velocity layer at the near surface, as shown in Fig. 5.9. The grid size of the velocity, vertical reflectivity and horizontal reflectivity is 10m. The synthetic data is also modeled using a Ricker wavelet centered at 20 Hz. The FD modeling employs the same algorithm as the first example.

FWMod and the proposed modeling compute up to the 5th order of internal multiples in the synthetic data.

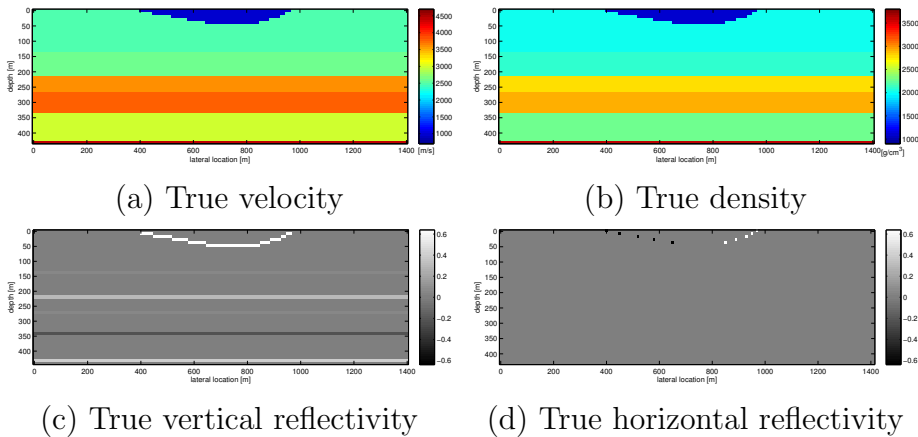


Figure 5.9: True velocity, density, and reflectivity models in the second example.

The snapshots of the propagated wavefields generated by each seismic modeling method are shown in Fig. 5.10. We can observe the propagated diving/refracted waves produced by our proposed method via comparison with the wavefields by the FD modeling and FWMod (see Fig. 5.10 (c) and (d)).

The shot gathers obtained by the FD modeling, FWMod and the proposed modeling are shown in Fig. 5.11 (a), (b) and (c), respectively. It can be seen that while conventional FWMod generates only reflected waves, including internal multiples (see Fig. 5.11 (b)), diving waves are realized in the shot data produced by the proposed modeling (see Fig. 5.11 (c)), although the direct waves are distorted by the amplitude scaling process for the horizontally propagated wavefields.

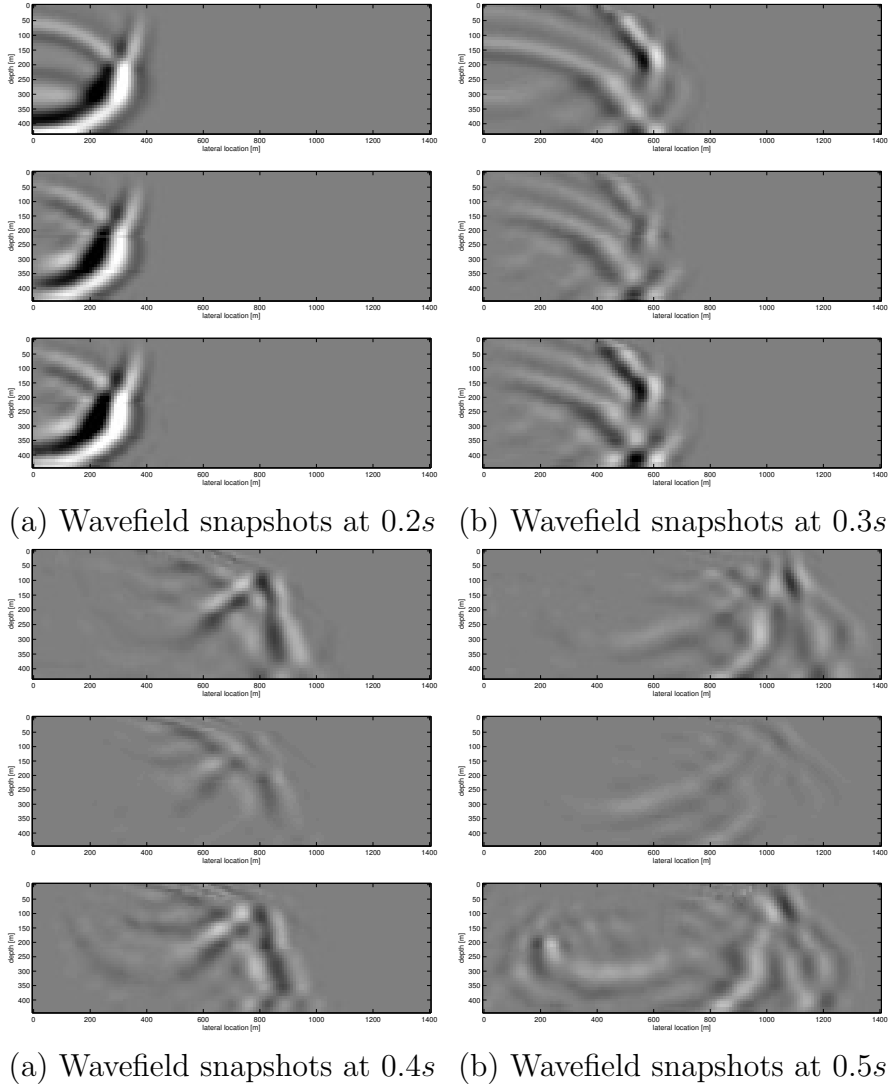
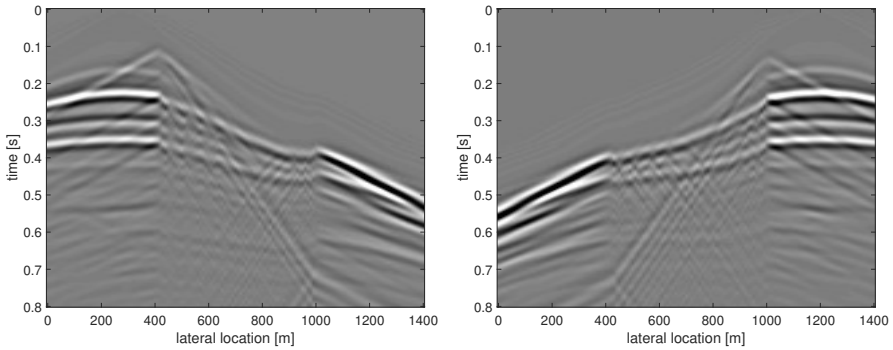
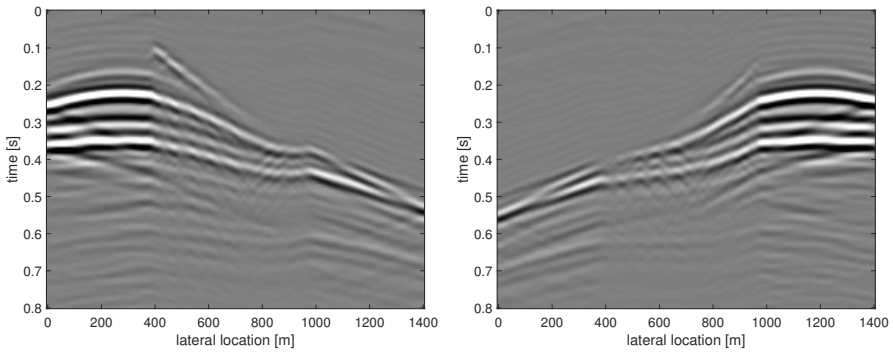


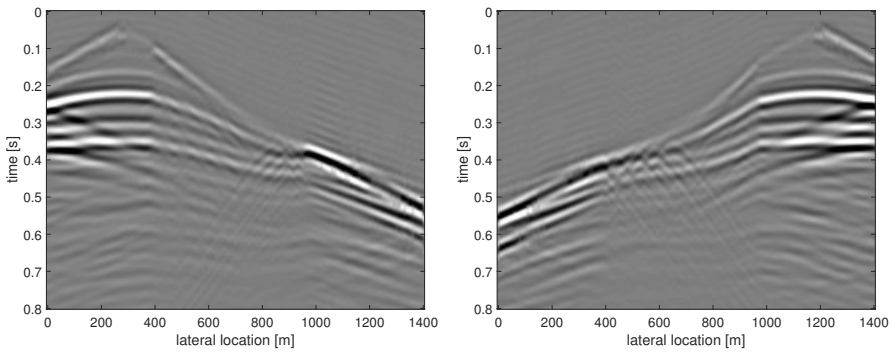
Figure 5.10: The comparison of snapshots generated by FD modeling (upper image), conventional FWMod (middle image), and the proposed modeling (lower image) at 0.2 s, 0.3 s, 0.4 s, and 0.5 s in the second example. The source is located at lateral location 0 m. The wavefields in the proposed modeling represent the total wavefields in the vertical reflectivity grid.



(a) FD modeling



(b) FWMod



(c) Proposed modeling

Figure 5.11: Comparison of shot gathers in the second example, with the source at $x = 280$ m (left column) and $x = 1190$ m (right column).

5.3 Omni-directional wavefield migration

This section describes an imaging condition for OWM algorithm based on the horizontal wavefield modeling process, discussed in the previous section. Then, we define a scaling factor for the horizontal reflectivity gradient calculated by the imaging condition. Finally, an initial numerical example for this migration is shown.

■ 5.3.1 Reflectivity update based on horizontal propagation

First, the residual between observed and modeled data at the surface is calculated to derive an imaging condition to update reflectivity models. We minimize the following residual based on least-squares fitting in the time domain:

$$\Delta p(x, t) \equiv p_{obs}^-(x, t) - \beta(x)p_v^-(x, t) - \gamma(x)(p_{right}^-(x, t) + p_{left}^-(x, t)), \quad (5.3.17)$$

with

$$\beta(x) = \arg \min_{\beta} \|p_{obs}^-(x, t) - \beta(x)p_v^-(x, t) - \gamma(x)(p_{right}^-(x, t) + p_{left}^-(x, t))\|_2^2, \quad (5.3.18)$$

$$\gamma(x) = \arg \min_{\gamma} \|p_{obs}^-(x, t) - \beta(x)p_v^-(x, t) - \gamma(x)(p_{right}^-(x, t) + p_{left}^-(x, t))\|_2^2, \quad (5.3.19)$$

where $p_{obs}^-(x, t)$ represents an observed data in the time domain, and $p_v^-(x, t)$, $p_{right}^-(x, t)$, and $p_{left}^-(x, t)$ are simulated upgoing, right-upgoing, and left-upgoing wavefields at the surface in the time domain, respectively. Then, a residual in the frequency domain $\vec{\eta} \in \mathbb{C}^{N_r}$ is represented from the residual in the time domain $\Delta p(x, t)$ via the Fourier transform:

$$\vec{\eta} \equiv \vec{\eta}(z_0, x_{s,\xi}, \omega_f) = [\eta(x_{\frac{1}{2}}), \dots, \eta(x_{N_r - \frac{1}{2}})]. \quad (5.3.20)$$

Using the residual $\vec{\eta}(z_0)$, we derive an imaging condition to calculate the gradient for vertical and horizontal reflectivity. The calculation

of the vertical reflectivity gradient and its scaling is the same as the standard FWM (Berkhout and Verschuur, 2011; Berkhout, 2014b). In FWM, the vertical gradient is derived from two types of correlations: 1) a correlation between the forward propagated downgoing wavefield and the back propagated upgoing wavefield, 2) a correlation between the forward propagated upgoing wavefield and the back propagated downgoing wavefield.

On the basis of a similar formulation, we can derive a horizontal reflectivity gradient by calculating two types of correlations: 1) a correlation between the forward propagated rightgoing wavefield $\vec{P}_h^+(x_m)$ and the back propagated leftgoing wavefield $\vec{B}_h^-(x_m)$, 2) a correlation between the forward propagated leftgoing wavefield $\vec{P}_h^-(x_m)$ and the back propagated rightgoing wavefield $\vec{B}_h^+(x_m)$.

The back propagated leftgoing wavefield $\vec{B}_h^-(x_{m+1})$ and the back propagated rightgoing wavefield $\vec{B}_h^+(x_m)$ are calculated by ($m = 0, 1, \dots, N_r - 1$):

$$\begin{aligned} \vec{B}_h^-(x_{m+1}) &= \mathbf{W}^-(x_{m+1}; x_{m+\frac{1}{2}})^H \vec{\zeta}(x_{m+\frac{1}{2}}) \\ &+ \mathbf{W}^-(x_{m+1}; x_m)^H \mathbf{T}^-(x_m)^H \vec{B}_h^-(x_m), \end{aligned} \quad (5.3.21)$$

$$\begin{aligned} \vec{B}_h^+(x_m) &= \mathbf{W}^+(x_m; x_{m+\frac{1}{2}})^H \vec{\zeta}(x_{m+\frac{1}{2}}) \\ &+ \mathbf{W}^+(x_m; x_{m+1})^H \mathbf{T}^+(x_{m+1})^H \vec{B}_h^+(x_{m+1}), \end{aligned} \quad (5.3.22)$$

where $\vec{\zeta}(x_{m+\frac{1}{2}}) = [\eta(x_{m+\frac{1}{2}}), 0, \dots, 0]^T \in \mathbb{C}^{N_z}$ is a vector including the residual in the frequency domain. The first term of the RHS in equations (5.3.21) and (5.3.22) represents the back propagated wavefield from the vertical reflectivity grid points at the surface to the horizontal reflectivity grid points. The second term of RHS in equations (5.3.21) and (5.3.22) indicates the back propagated wavefield from the horizontal reflectivity grid points to the horizontal reflectivity grid points. Therefore, the calculation of the horizontal reflectivity gradient in OWM is summarized in algorithm 7.

Scaling for the calculated horizontal reflectivity gradient is not a straightforward process because there is a difference of amplitude scale between vertically propagated wavefields and horizontally propagated wavefields,

Algorithm 7 Calculation of the horizontal gradient for OWM.

Input: $\vec{\eta}(z_0)$, $\vec{P}_h^\pm(x_m)$, $\mathbf{T}^\pm(x_m)$, ($m = 0, 1, \dots, N_r$), $\mathbf{W}^+(x_{m+1}; x_m)$, $\mathbf{W}^+(x_{m+\frac{1}{2}}; x_m)$,
 ($m = 0, 1, \dots, N_r - 1$), $\mathbf{W}^-(x_{m-1}; x_m)$, $\mathbf{W}^-(x_{m-\frac{1}{2}}; x_m)$, ($m = 1, 2, \dots, N_r$)

Output: $[\nabla \vec{J}_{r,h}(x_0), \dots, \nabla \vec{J}_{r,h}(x_{N_r})]$

- 1: $\vec{B}_h^-(x_0) = 0$, $\vec{B}_h^+(x_{N_r}) = 0$, $\nabla \vec{J}_{r,h}(x_0) = 0$, $\nabla \vec{J}_{r,h}(x_{N_r}) = 0$
 - 2: **for** $m = 0 \rightarrow N_r - 1$ **do**
 - 3: $\vec{\zeta}(x_{m+\frac{1}{2}}) = [\eta(x_{m+\frac{1}{2}}), 0, \dots, 0]^T \in \mathbb{C}^{N_z}$, where $\vec{\eta} \equiv [\eta(x_{\frac{1}{2}}), \dots, \eta(x_{N_r-\frac{1}{2}})]$
 - 4: $\vec{B}_h^-(x_{m+1}) = \mathbf{W}^-(x_{m+1}; x_{m+\frac{1}{2}})^H \vec{\zeta}(x_{m+\frac{1}{2}}) + \mathbf{W}^-(x_{m+1}; x_m)^H \mathbf{T}^-(x_m)^H \vec{B}_h^-(x_m)$
 - 5: $\nabla \vec{J}_{r,h}(x_{m+1}) = \sum^{N_s} \sum^{N_\omega} \Re\{\vec{B}_h^-(x_{m+1}) \circ [\vec{P}_h^+(x_{m+1})]^*\}$
 - 6: **end for**
 - 7: **for** $m = N_r - 1 \rightarrow 0$ **do**
 - 8: $\vec{B}_h^+(x_m) = \mathbf{W}^+(x_m; x_{m+\frac{1}{2}})^H \vec{\zeta}(x_{m+\frac{1}{2}}) + \mathbf{W}^+(x_m; x_{m+1})^H \mathbf{T}^+(x_{m+1})^H \vec{B}_h^+(x_{m+1})$
 - 9: $\nabla \vec{J}_{r,h}(x_m) \leftarrow \nabla \vec{J}_{r,h}(x_m) + \sum^{N_s} \sum^{N_\omega} \Re\{\vec{B}_h^+(x_m) \circ [\vec{P}_h^-(x_m)]^*\}$
 - 10: **end for**
-

as discussed in the previous modeling part. We approximately determine a scaling factor for the horizontal reflectivity gradient $\nabla J_{r,h}$ from the vertical reflectivity gradient $\nabla J_{r,v}$ and its scaling factor $\alpha_{r,v}$. Let $\nabla J_{r,v}(x, z)$ and $\nabla J_{r,h}(x, z)$ be the vertical and horizontal reflectivity gradient at grid point (x, z) , respectively. Then, we define the following update rule for the horizontal reflectivity model r_h :

$$r_h(x, z) \leftarrow r_h(x, z) + \frac{\max_{x,z} |\alpha_{r,v} \nabla J_{r,v,xz}|}{\max_{x,z} |\nabla J_{r,h,xz}|} \nabla J_{r,h}(x, z), \quad (5.3.23)$$

where $\nabla J_{r,v,xz}$ and $\nabla J_{r,h,xz}$ represent the components of the matrix which consists of $\nabla J_{r,v}(x, z)$ and $\nabla J_{r,h}(x, z)$, respectively.

■ 5.3.2 Numerical examples

Two numerical examples are given to show the performance of OWM.

Example 1: Salt flank-shaped model

The first example is a 2D model including a salt flank-shaped anomaly with a high velocity, as shown in Fig. 5.12 (a)-(d). Acoustic FD modeling is used to generate synthetic shot data. The lateral and depth grid size of this model for migration are 20 m and 10 m, respectively.

For the utilized migration mode schedule, only vertical imaging, which represents standard FWM, is applied in the first 12 iterations, and then horizontal imaging is added from the 13th to the last 20th iteration, as shown in table 5.1. This is because running both vertical and horizontal imaging in an initial iteration stage causes computational instability in our experience. The true velocity (Fig. 5.12 (a)) is used as the input velocity for the migration. Full offset of 3.0 km in the measured seismic shot data is utilized for OWM.

Figure 5.12 (e) and (f) show the results of the vertical and horizontal reflectivity image by OWM, respectively. The estimated horizontal reflectivity realizes the lateral reflectivity variation that cannot be reconstructed by vertical imaging (Fig. 5.12 (f)).

Table 5.1: *The migration mode schedule.*

Iterations	Migration mode
1st-12th	Vertical imaging mode
13th-20th	Vertical imaging mode + Horizontal imaging mode

Example 2: Lens-shaped model

The second example is a 2D model including a lens-shaped anomaly with a high velocity, as shown in Fig. 5.13. We perform acoustic FD modeling to generate a synthetic shot dataset (Fig. 5.15 (a)).

The utilized migration mode schedule for this example is illustrated in table 5.2. The true velocity (Fig. 5.13 (a)) is used as the input velocity for the migration. Full offset of the shot data is employed for OWM. In addition to the original shot dataset, we prepare an inner muted shot dataset (Fig. 5.15 (b)) to reduce the influence of reflected waves and investigate the validity of the OWM by utilizing refracted/diving waves.

Figure 5.14 (a) and (b) show the results of OWM for the original shot data, respectively. It is found that the estimated horizontal reflectivity shows an outline of the anomaly (Fig. 5.14 (b)), while the vertical reflectivity estimation also provides an image of the anomaly (Fig. 5.14

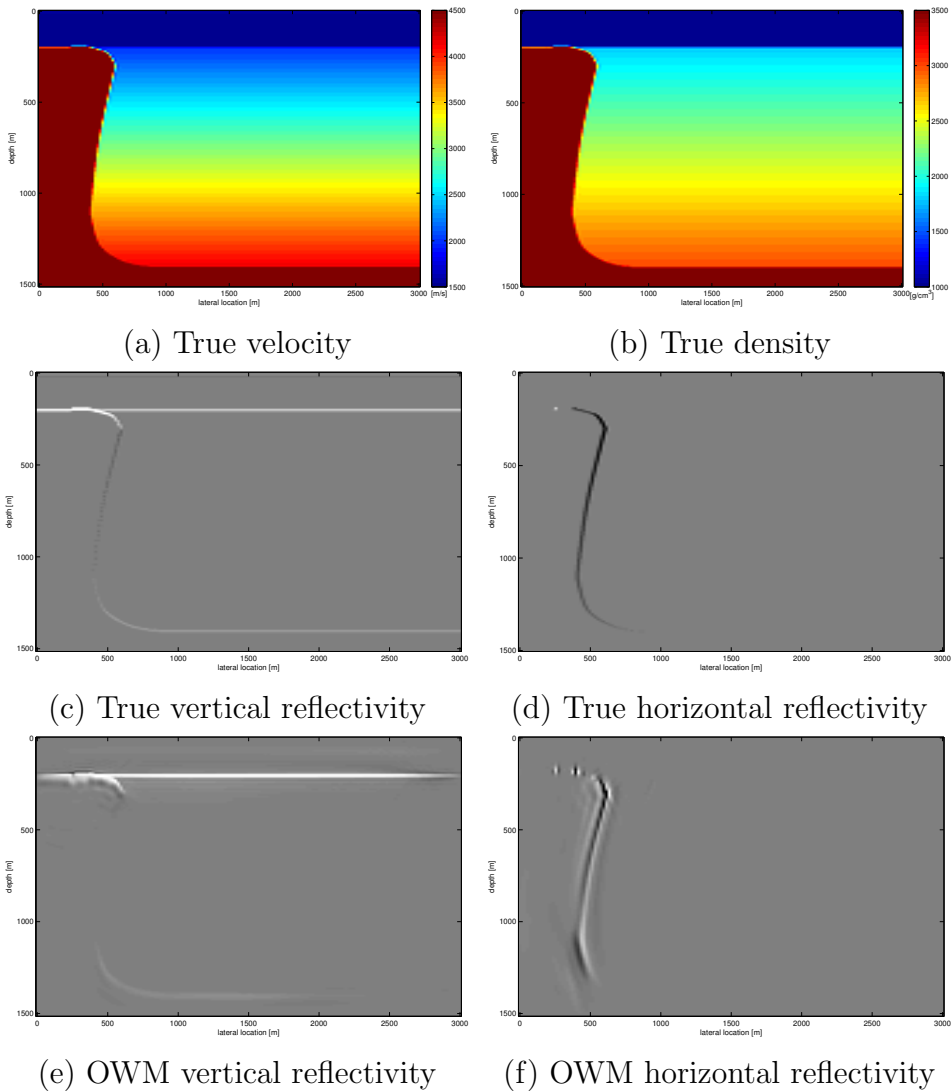


Figure 5.12: True velocity (a), density (b) and reflectivity models (c,d) for the OWM test and the estimated reflectivity models (e,f).

(a)). For the limited shot data by the inner mute, the shape of the anomaly is reconstructed in the horizontal image shown in Fig. 5.14 (d), while the vertical reflectivity image (Fig. 5.14 (c)) is affected, as

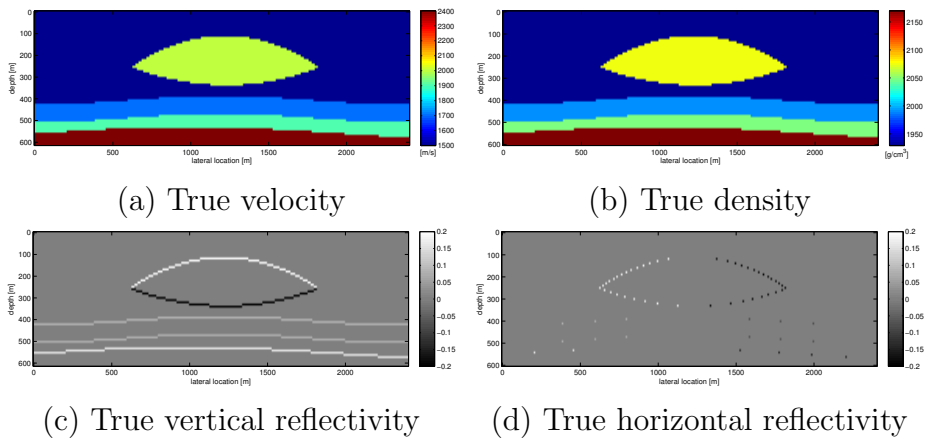


Figure 5.13: True velocity, density and reflectivity models for OWM.

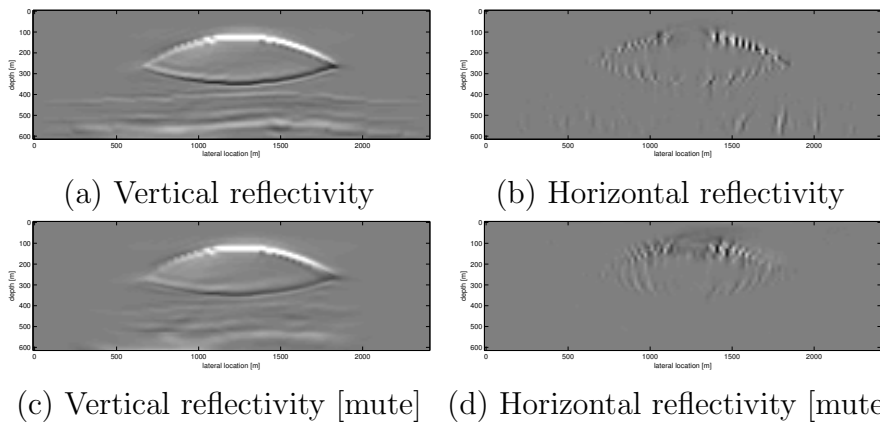
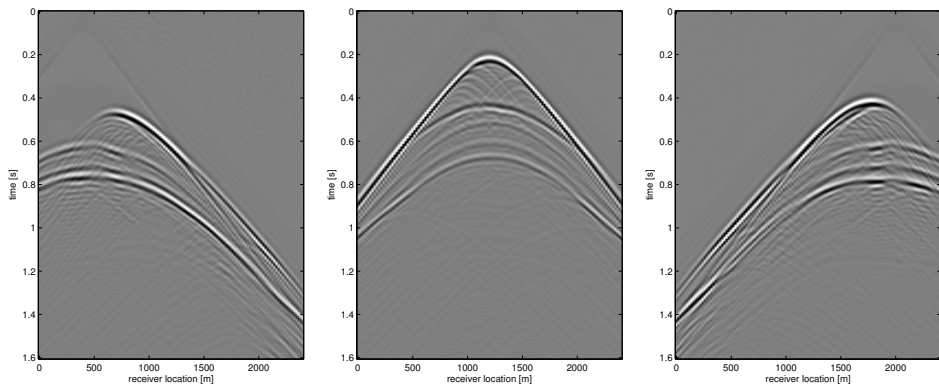


Figure 5.14: Vertical and horizontal wavefield imaging results after 14 iterations for the original shot data (a, b) and the inner-muted data (c, d).

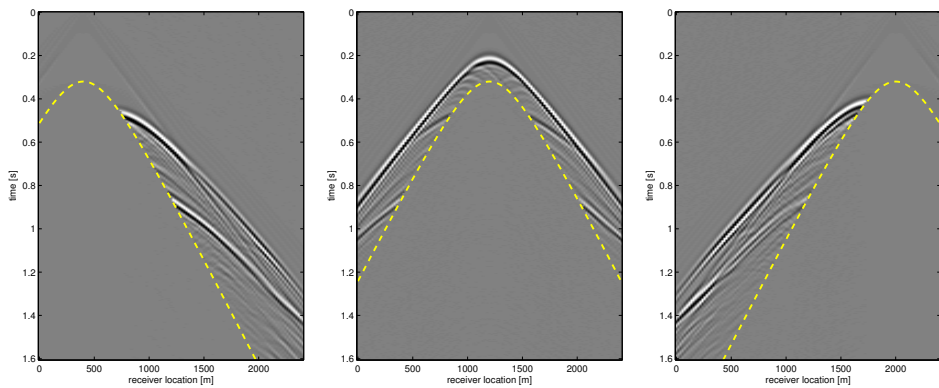
expected. Therefore, these results demonstrate that OWM can utilize diving waves through its horizontal propagation process, although the refracted waves are not completely taken into account in this imaging condition.

Table 5.2: *The migration mode schedule.*

Iterations	Migration mode
1st-12th	Vertical imaging mode
13th-14th	Vertical imaging mode + Horizontal imaging mode



(a) Original shot gathers



(b) Shot gathers after inner mute

Figure 5.15: *Original (a) and inner muted (b) synthetic shot gathers. Yellow dotted lines represent the boundary of the inner mute.*

5.4 Omni-directional joint migration inversion

Since an omni-directional extension of wavefield migration was derived in the previous section, we formulate an omni-directional propagation-based JMI by adding the slowness update function based on horizontal propagation.

■ 5.4.1 Slowness update based on horizontal propagation

In order to implement an OJMI method, the slowness gradient to update velocity based on horizontal propagation is formulated. The calculation of the slowness gradient based on vertical propagation and its scaling process is the same as the standard JMI (Berkhout and Verschuur, 2011; Berkhout, 2014b). In JMI, the slowness gradient obtained by vertical propagation is derived from two types of correlations: 1) a correlation between the forward propagated downgoing wavefield and the back propagated downgoing wavefield, 2) a correlation between the forward propagated upgoing wavefield and the back propagated upgoing wavefield.

Using a similar formulation, we can derive the slowness gradient based on horizontal propagation by calculating two types of correlations: 1) a correlation between the forward propagated leftgoing wavefield $\vec{Q}_h^-(x_m)$ and the back propagated leftgoing wavefield $\vec{F}_h^-(x_m)$, 2) a correlation between the forward propagated rightgoing wavefield $\vec{Q}_h^+(x_m)$ and the back propagated rightgoing wavefield $\vec{F}_h^+(x_m)$.

In this process, an operator $\mathbf{L}(x_m; x_n)$, which is similar to the vertical component shown in equation (A.2.13), is defined by:

$$\vec{L}_j(x_m; x_n) = \mathcal{F}_z^{-1} \left[-j\omega \Delta \tilde{x} \left[\frac{k_x^* k}{|k_x|^2 + \epsilon} \right]_{\sigma_{old}} e^{-jk_x \Delta \tilde{x}} e^{-jk_z z_j} \right], \quad (5.4.24)$$

with

$$\Delta \tilde{x} \equiv |x_n - x_m|. \quad (5.4.25)$$

Algorithm 8 Calculation of the slowness gradient for horizontal propagation.

Input: $\vec{\eta}(z_0)$, $\vec{Q}_h^\pm(x_m)$, $\mathbf{T}^\pm(x_m)$, ($m = 0, 1, \dots, N_r$), $\mathbf{W}^+(x_{m+1}; x_m)$, $\mathbf{W}^+(x_{m+\frac{1}{2}}; x_m)$, $\mathbf{L}^+(x_{m+1}; x_m)$, ($m = 0, 1, \dots, N_r - 1$), $\mathbf{W}^-(x_{m-1}; x_m)$, $\mathbf{W}^-(x_{m-\frac{1}{2}}; x_m)$, $\mathbf{L}^-(x_{m-1}; x_m)$, ($m = 1, 2, \dots, N_r$)

Output: $[\nabla \vec{J}_{r,h}(x_0), \dots, \nabla \vec{J}_{r,h}(x_{N_r})]$

- 1: $\vec{B}_h^-(x_0) = 0$, $\vec{B}_h^+(x_{N_r}) = 0$, $\nabla \vec{J}_{r,h}(x_0) = 0$, $\nabla \vec{J}_{r,h}(x_{N_r}) = 0$
 - 2: **for** $m = 0 \rightarrow N_r - 1$ **do**
 - 3: $\vec{\zeta}(x_{m+\frac{1}{2}}) = [\eta(x_{m+\frac{1}{2}}), 0, \dots, 0]^T \in \mathbb{C}^{N_z}$, where $\vec{\eta} \equiv [\eta(x_{\frac{1}{2}}), \dots, \eta(x_{N_r-\frac{1}{2}})]$
 - 4: $\vec{F}_h^-(x_{m+1}) = \mathbf{L}^-(x_{m+1}; x_m)^H \vec{B}_h^-(x_m)$
 - 5: $\vec{B}_h^-(x_{m+1}) = \mathbf{W}^-(x_{m+1}; x_{m+\frac{1}{2}})^H \vec{\zeta}(x_{m+\frac{1}{2}}) + \mathbf{W}^-(x_{m+1}; x_m)^H \mathbf{T}^-(x_m)^H \vec{B}_h^-(x_m)$
 - 6: $\nabla \vec{J}_{\sigma,h}(x_{m+1}) = \sum^{N_s} \sum^{N_\omega} \Re\{\vec{F}_h^-(x_{m+1}) \circ [\vec{Q}_h^-(x_{m+1})]^*\}$
 - 7: **end for**
 - 8: **for** $m = N_r - 1 \rightarrow 0$ **do**
 - 9: $\vec{F}_h^+(x_m) = \mathbf{L}^+(x_m; x_{m+1})^H \vec{B}_h^+(x_{m+1})$
 - 10: $\vec{B}_h^+(x_m) = \mathbf{W}^+(x_m; x_{m+\frac{1}{2}})^H \vec{\zeta}(x_{m+\frac{1}{2}}) + \mathbf{W}^+(x_m; x_{m+1})^H \mathbf{T}^+(x_{m+1})^H \vec{B}_h^+(x_{m+1})$
 - 11: $\nabla \vec{J}_{\sigma,h}(x_m) \leftarrow \nabla \vec{J}_{\sigma,h}(x_m) + \sum^{N_s} \sum^{N_\omega} \Re\{\vec{F}_h^+(x_m) \circ [\vec{Q}_h^+(x_m)]^*\}$
 - 12: **end for**
-

Therefore, the calculation of the slowness gradient from horizontal propagation in OJMI is summarized in algorithm 8.

A scaling factor for the horizontal effect of slowness gradient $\nabla J_{\sigma,h}$ assumes to be computed by the vertical effect of slowness gradient $\nabla J_{\sigma,v}$ and its scaling factor $\alpha_{\sigma,v}$. Then, we define the following update rule for the slowness model σ_h computed by horizontal migration:

$$\sigma_h(x, z) \leftarrow \sigma_h(x, z) + \frac{\sqrt{\frac{1}{N_z} \frac{1}{N_r} \sum^{N_z} \sum^{N_r} (\alpha_{\sigma,v} \nabla J_{\sigma,v,xz})^2}}{\sqrt{\frac{1}{N_z} \frac{1}{N_r} \sum^{N_z} \sum^{N_r} (\nabla J_{\sigma,h,xz})^2}} \nabla J_{\sigma,h}(x, z), \quad (5.4.26)$$

where $\nabla J_{\sigma,v,xz}$ and $\nabla J_{\sigma,h,xz}$ represent the components of the matrix

which consists of $\nabla J_{\sigma,v}(x, z)$ and $\nabla J_{\sigma,h}(x, z)$, respectively. This scaling method indicates that the root-mean-square value of the slowness gradient for vertical propagation is scaled by that for horizontal propagation.

■ 5.4.2 Velocity update based on horizontal reflectivity constraint

To further improve the accuracy of velocity estimation, we introduce a horizontal reflectivity-constrained velocity estimation, which is almost the same as the mentioned derivation of vertical reflectivity-constrained velocity estimation. In the horizontal reflectivity constraint, the summation of two directional constraints is utilized to suppress the artifacts caused by the calculation of the numerical integrals.

We derive a horizontal reflectivity approximation calculated from the estimated velocity by the same procedure as the vertical reflectivity approximation. Two horizontal reflectivities calculated from right and left side are defined by:

$$r_{right}(x_{m+1}, z) = \frac{\rho(x_{m+1}, z)c(x_{m+1}, z) - \rho(x_m, z)c(x_m, z)}{\rho(x_{m+1}, z)c(x_{m+1}, z) + \rho(x_m, z)c(x_m, z)}, \quad (5.4.27)$$

$$r_{left}(x_{m+1}, z) = \frac{\rho(x_m, z)c(x_m, z) - \rho(x_{m+1}, z)c(x_{m+1}, z)}{\rho(x_m, z)c(x_m, z) + \rho(x_{m+1}, z)c(x_{m+1}, z)}. \quad (5.4.28)$$

Next, we assume that the density model ρ is also constant in the constraints. Then, the reflectivities are approximately calculated by:

$$r_{right}(x_{m+1}, z) \simeq \frac{c(x_{m+1}, z) - c(x_m, z)}{c(x_{m+1}, z) + c(x_m, z)}, \quad (5.4.29)$$

$$r_{left}(x_{m+1}, z) \simeq \frac{c(x_m, z) - c(x_{m+1}, z)}{c(x_m, z) + c(x_{m+1}, z)}. \quad (5.4.30)$$

We additionally assume that the vertical variation of velocity models is much smaller than the horizontal variation. Then, numerical approximations can be obtained from equation (5.4.29) and (5.4.30):

$$r_{right}(x_{m+1}, z) \sim \frac{\Delta c_{right}}{\Delta x} \times \text{const.}, \quad (5.4.31)$$

$$r_{left}(x_{m+1}, z) \sim \frac{\Delta c_{left}}{\Delta x} \times \text{const.}, \quad (5.4.32)$$

where $\Delta c_{right} \equiv c(x_{m+1}, z) - c(x_m, z)$, $\Delta c_{left} \equiv c(x_m, z) - c(x_{m+1}, z)$ and $\Delta x \equiv |x_{m+1} - x_m|$. Therefore, the estimated reflectivities derived from the velocity model are defined by:

$$r_{right,constr} \equiv \frac{\partial c_{right}}{\partial x}, \quad (5.4.33)$$

$$r_{left,constr} \equiv \frac{\partial c_{left}}{\partial x}. \quad (5.4.34)$$

The horizontal reflectivity residual between the reflectivity obtained from horizontal migration $r_h(x, z)$ and the horizontal reflectivity approximated by the velocity model is computed via least-squares fitting:

$$r_{right,res}(x, z) \equiv r_h(x, z) - \Lambda_{right} r_{right,constr}(x, z), \quad (5.4.35)$$

$$\Lambda_{right} = \arg \min_{\Lambda_{right}} \|r_{right}(x, z) - \Lambda_{right} r_{right,constr}(x, z)\|_2^2, \quad (5.4.36)$$

and

$$r_{left,res}(x, z) \equiv r_h(x, z) + \Lambda_{left} r_{left,constr}(x, z), \quad (5.4.37)$$

$$\Lambda_{left} = \arg \min_{\Lambda_{left}} \|r_{left}(x, z) + \Lambda_{left} r_{left,constr}(x, z)\|_2^2. \quad (5.4.38)$$

To calculate the gradient for the velocity update, we take the numerical integrals of the reflectivity residual along x :

$$\nabla J_{c,right}(x, z) = \lambda_h \int_{x_{\min}}^x r_{right,res}(x', z) dx', \quad (5.4.39)$$

$$\nabla J_{c,left}(x, z) = \lambda_h \int_x^{x_{\max}} r_{left,res}(x', z) dx', \quad (5.4.40)$$

where $\lambda_h \in \mathbb{R}^+$ represents an weight factor. Scale factors for the velocity update of these constraints are given by:

$$\alpha_{c,right} = \frac{\sum_x \sum_z \left| \int_{x_{\min}}^x r_{right,res}(x', z) dx' \right|^2}{\sum_x \sum_z \left| \int_{x_{\min}}^x r_h(x', z) dx' \right|^2}. \quad (5.4.41)$$

$$\alpha_{c,left} = \frac{\sum_x \sum_z \left| \int_x^{x_{\max}} r_{left,res}(x', z) dx' \right|^2}{\sum_x \sum_z \left| \int_x^{x_{\max}} r_h(x', z) dx' \right|^2}. \quad (5.4.42)$$

Therefore, we can update the velocity model as follows:

$$c^{(k+1)}(x, z) = c^{(k)}(x, z) + \alpha_{c,right} \nabla J_{c,right}(x, z) - \alpha_{c,left} \nabla J_{c,left}(x, z). \quad (5.4.43)$$

Note again that the summation of right and left directional constraints is taken to suppress the artifacts caused by the calculation of the numerical integrals in the horizontal reflectivity constraints.

■ 5.4.3 Numerical example

A numerical example is a 2D model including a salt flank-shaped anomaly with strong dips at the central part, as shown in Fig. 5.16. The receiver and source intervals are 20 m and 80 m, respectively. Shot data for this example is produced by acoustic FD modeling with a Ricker source wavelet centered at 20 Hz. Note again that this FD modeling also includes the effects of refracted/diving waves. We test standard JMI, RCJMI and OJMI for this shot data with a 1D initial model illustrated in Fig. 5.17 (a). The frequency range of 5-40 Hz and full offset of 2.0 km in the measured seismic shot data are utilized for these inversion algorithms. As shown in table 5.3, which represents the schedule for vertical and horizontal propagation in OJMI, the 13th-60th iteration in OJMI involves both vertical and horizontal propagation mode.

Figure 5.17 (b)-(d) represent the results of JMI, RCJMI and OJMI, respectively. Note that RCJMI includes only vertical reflectivity-constrained velocity estimation and OJMI includes vertical and horizontal reflectivity-constrained velocity estimation. It can be seen that OJMI provides an accurate velocity of the high velocity anomaly compared to JMI and RCJMI. On the basis of the estimated velocity, OJMI is capable of reconstructing the reflectivity of the salt flank shown in Fig. 5.18, although the reflectivity image needs to be further improved.

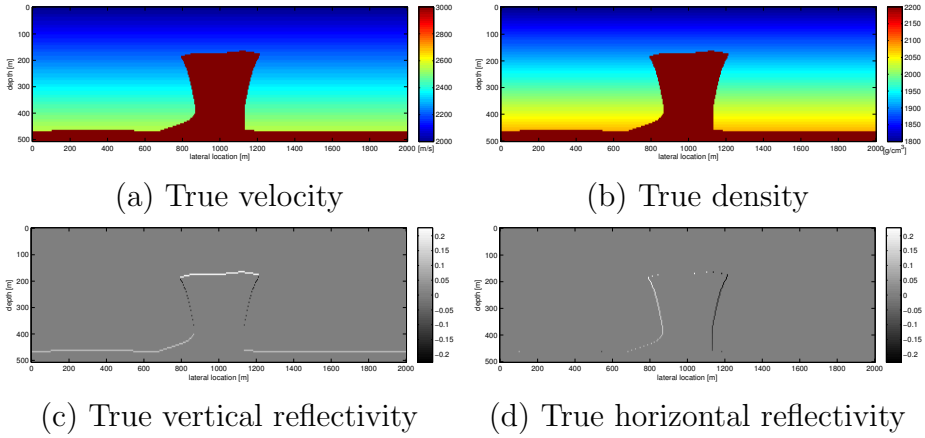


Figure 5.16: True velocity, density and reflectivity models in the salt flank-shaped example.

Table 5.3: The vertical and horizontal propagation schedule in OJMI.

Iterations	Propagation mode
1st-12th	Vertical propagation
13th-60th	Vertical propagation + Horizontal propagation

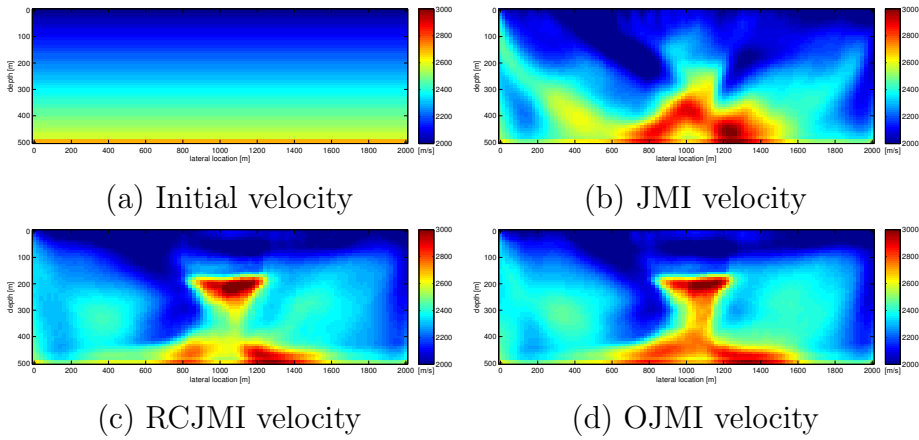


Figure 5.17: Estimated velocity models by JMI, RCJMI and OJMI. Here, RCJMI includes only vertical reflectivity-constrained velocity estimation and OJMI includes vertical and horizontal reflectivity-constrained velocity estimation. The number of iterations is 60 iterations.

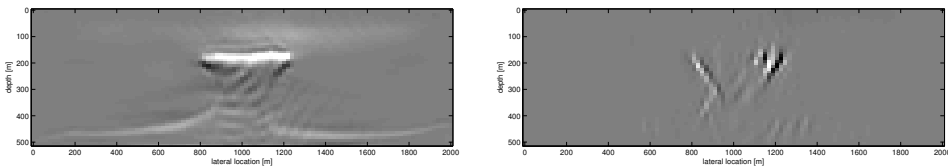


Figure 5.18: Estimated reflectivity models by OJMI. The number of iterations is 60 iterations.

5.5 Discussion

■ 5.5.1 Misfit function

In the current implementation for OWM and OJMI, a misfit function is defined for vertical and horizontal propagation, as described in equation (5.3.17). This single misfit function is based on the least-squares fitting for an observed term and two simulated terms, which represent vertically and horizontally propagated wavefields. The use of two misfit functions for vertical and horizontal propagation can be also discussed. When two observed terms for vertical wavefields $p_{obs,v}^-(x, t)$ and horizontal wavefields $p_{obs,h}^-(x, t)$ are considered, we can define two misfit functions for each propagation mode:

$$\Delta p_v(x, t) \equiv p_{obs,v}^-(x, t) - \alpha_v(x)p_v^-(x, t), \quad (5.5.44)$$

$$\Delta p_h(x, t) \equiv p_{obs,h}^-(x, t) - \alpha_h(x)p_h^-(x, t), \quad (5.5.45)$$

with

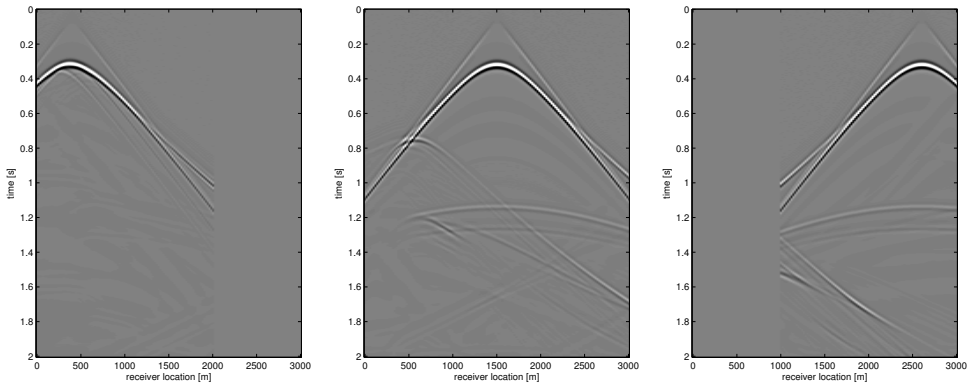
$$\alpha_v(x) = \arg \min_{\alpha_v} \|p_{obs,v}^-(x, t) - \alpha_v(x)p_v^-(x, t)\|, \quad (5.5.46)$$

$$\alpha_h(x) = \arg \min_{\alpha_h} \|p_{obs,h}^-(x, t) - \alpha_h(x)p_h^-(x, t)\|, \quad (5.5.47)$$

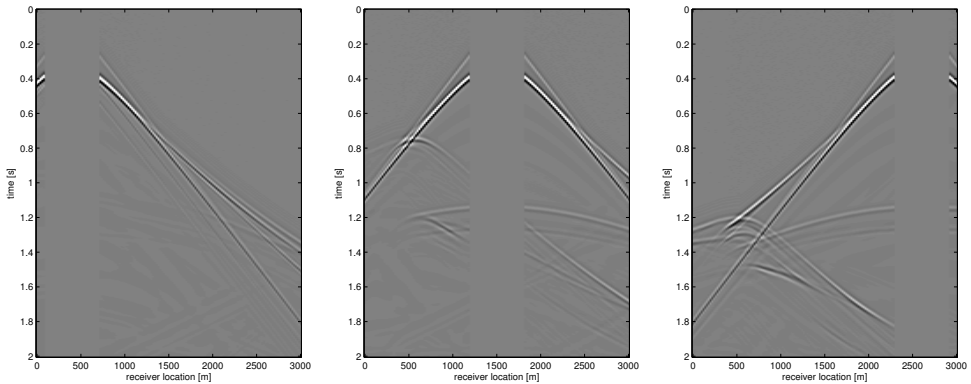
where these misfit functions are also based on least-squares fitting. The potential advantage of this approach in OWM and OJMI is to effectively enhance the dominant waves and suppress noise in each propagation by applying the offset limitation and/or mute for the seismic data.

We test this approach for OWM through the previous salt flank-shaped model which was shown in section 5.3. As illustrated in Fig. 5.19, two offset-limited shot datasets are prepared as two observed datasets for OWM. While the far-offset part is removed in the observed data for the vertical propagation mode $p_{obs,v}^-(x, t)$ to reduce AVO effects, the near-offset part is removed in the observed data for the horizontal propagation mode $p_{obs,h}^-(x, t)$ because the near-offset part of the shot data is not accurately calculated in the horizontal propagation mode. Figure 5.20 indicates the comparison between the previous OWM results (Fig. 5.20 (a)) for the full offset data with the single misfit function

and the OWM results for the limited-offset data with the double misfit functions. It is found that OWM for the limited-offset data with the double misfit functions can also produce almost the same reflectivity images as the previous images in this example. Therefore, the optimum selection of the misfit functions in OWM and OJMI is still an open issue.



(a) Far-offset limited data for vertical propagation $p_{obs,v}^-(x, t)$



(b) Near-offset limited data for horizontal propagation $p_{obs,h}^-(x, t)$

Figure 5.19: Examples of far-offset limited (a) and near-offset limited (b) synthetic shot gathers.

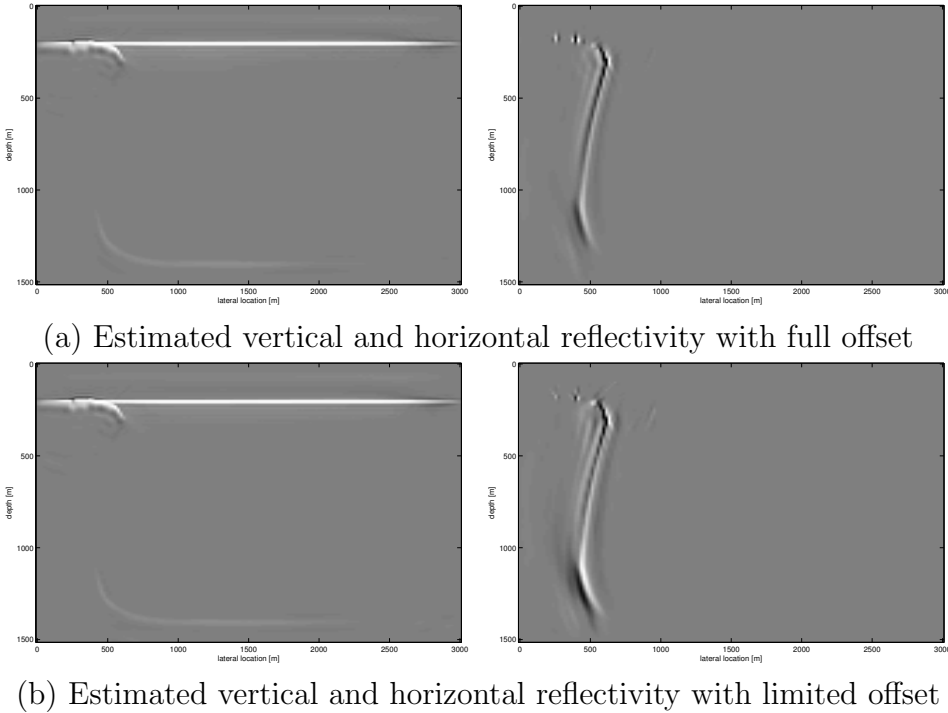


Figure 5.20: The comparison of the estimated reflectivity models by two approaches of OWM: (a) full offset data with the single objective function, (b) limited offset data with the double objective functions for vertical and horizontal propagation.

■ 5.5.2 Waves utilized for reflectivity and slowness update

The proposed omni-directional wavefield modeling algorithm enables us to generate diving waves and refracted waves. On the other hand, refracted waves are not completely taken into account for the reflectivity and slowness update in OWM and OJMI, although diving waves are exploited in the updates. More accurate refracted waves could be theoretically utilized for the update by imposing the condition to calculate upgoing wavefields in the back propagation process before rightgoing and leftgoing wavefields are computed.

■ 5.5.3 Iteration strategy for horizontal propagation

As stated previously, a horizontal propagation mode in OWM and OJMI is added only after a certain number of iterations for the reason of avoiding the computational instability. The iteration timing of adding the horizontal mode is determined by our empirical knowledge. However, this iteration strategy should be optimized as future work.

5.6 Conclusions

In this chapter, we present an omni-directional extension for wavefield modeling, wavefield migration and joint migration inversion in order to handle refracted/diving waves and reflected waves including internal multiples via both vertical and horizontal propagation. Numerical examples demonstrated the validity of these algorithms.

Conclusions and recommendations

This thesis discusses novel approaches for pre-processing, seismic forward modeling, migration and velocity inversion in order to accurately obtain land and marine seismic images without the low frequencies of the observed data through extending the concept of JMI and adding new ideas. In this chapter, the main conclusions and future recommendations are described.

6.1 Conclusions

In this thesis, two directions are presented to enhance the accuracy of seismic imaging based on JMI. One direction is to improve the performance of JMI by introducing interactive reflectivity-constrained velocity estimation in the inversion process and employing a surface-consistent amplitude correction via learning from synthetic models in the pre-processing. Another direction is to correctly incorporate the effect of refracted/diving waves into JMI via an omnidirectional extension. These algorithms have been tested on numerical examples and field data examples. The main conclusions from this work are as follows:

- The iterative reflectivity-constrained velocity estimation improves the accuracy of the estimated velocity model without the low frequencies of seismic data.
- The learning-based surface-amplitude correction method is effective to apply JMI to land seismic data and improve the obtained image quality.
- The omnidirectional extension of JMI handles refracted/diving waves and reflected waves including internal multiples.

As discussed in chapter 3 and 4, the validity of the reflectivity-constrained velocity estimation is demonstrated for marine and land seismic data without low frequencies. In the land seismic data application, the learning-based surface-amplitude correction method is also helpful to enhance the effect of the reflectivity-constrained velocity estimation, because the improvement of the migration image via the amplitude correction also contributes to the velocity estimation.

An important feature of the reflectivity-constrained velocity estimation process is that it gives a high-resolution velocity model that is comparable to the migration image, although the resolution of the velocity estimated by most of current velocity estimation methods is lower than that of the migration image. This fact would mean that the value of the velocity model also increases in terms of its use for direct seismic interpretation.

Finally, as shown in chapter 5, introducing vertical and horizontal reflectivity grids and extending the forward/back propagation process via the omni-directional approach, we can overcome the limitation caused by the one-way propagator used in JMI: generating refracted and diving waves. In addition, the accuracy of velocity estimation can be improved by adding a constraint based on horizontal migration in horizontal reflectivity grids. This method would give a new value in the seismic imaging based on JMI and other one-way propagator-based approaches.

6.2 Recommendations for further research

■ 6.2.1 Reflectivity-constrained velocity estimation

In this thesis, the effectiveness of reflectivity-constrained velocity estimation is demonstrated via including it within the framework of JMI. This constraint could be theoretically applied to not only JMI, but also to FWI by simultaneously carrying out some migration process like least-squares RTM in each FWI iteration. Therefore, the reflectivity constraint for velocity inversion would be also helpful to improve the accuracy of the velocity estimation by FWI.

■ 6.2.2 JMI including more accurate physical phenomena

The implementation of the JMI method employed in this thesis assumes that only reflected waves including internal multiples in isotropic media are regarded as signals. However, real data includes other physical phenomena. In this thesis, an omni-directional extension to correctly exploit the effect of refracted waves and diving waves in the framework of JMI is discussed.

For further improving JMI some other extensions can be considered. For example, the current implementation does not include the effects of AVO, anisotropy and anelastic attenuation. Incorporating the AVO and anisotropic effects into JMI process has been already discussed in Davydenko and Verschuur (2017a) and Alshuhail and Verschuur (2015), respectively. Moreover, other wave modes such as surface waves and converted waves and can be also measured in real data. Therefore, correctly handling these wave modes and physical effects in the JMI process are open research topics. The challenge in such research topics is that the relationship between taking into account accurate physics in modeling and the nonlinearity in its inversion would be generally a trade-off. On such research, it should be noted that local minima are difficult to avoid when dealing with a highly non-linear inverse problem, based on complex seismic modeling algorithms.

■ 6.2.3 Machine learning

Another approach to improve seismic imaging would be to utilize machine learning algorithms, as a learning process for surface consistent amplitude correction is also introduced in this thesis. Nowadays, machine learning technologies, especially so-called deep learning (e.g. LeCun et al., 2015), provide a major breakthrough in image processing and audio/speech signal processing, and these trends are more and more penetrating in other application fields, such as wireless communication, radar and tomography. These technologies are expected to have large impact on the improvement of many fields, although the extra computational cost might be a challenge in some case.

It would be relatively easy to apply machine learning to the pre-processing in seismic imaging, because the techniques developed in image processing and audio/speech signal processing can be almost directly transferred to the field of the seismic pre-processing processing. For example, machine learning processes would be effective in background noise attenuation on the measured data. If we measure the data without seismic signals, the data can be exploited as training data for learning the background noise.

As discussed in this thesis, the approaches that combine some learning algorithm with seismic forward modeling process also have potential for seismic imaging or its pre-processing. For instance, the missing low frequency components of field data might be estimated by learning the relationship between low frequencies and high frequencies via training.

More direct seismic imaging method based on machine learning is also a new potential study. Araya-Polo et al. (2018) recently proposed a deep learning tomography, which is a velocity estimation method by deep neural network via automatically learning the features of NMO analysis. These kind of concepts have enormous potential for future research.

Since both physics modeling-based approach and machine learning-based approach have advantages and disadvantages, it is desirable to effectively combine the two approaches in future seismic imaging.

A

Reflectivity and velocity updates by JMI

This section derives the update rules for JMI. If we assume that reflection coefficients are angle and frequency independent and the subsurface wave conversion is small, we can obtain the following approximations:

$$\mathbf{R}(z_n) = \mathbf{R}^{\cup}(z_n) = -\mathbf{R}^{\cap}(z_n), \quad (\text{A.0.1})$$

$$\delta\mathbf{T}^+(z_n) = \mathbf{R}(z_n), \quad (\text{A.0.2})$$

$$\delta\mathbf{T}^-(z_n) = -\mathbf{R}(z_n), \quad (\text{A.0.3})$$

where $\mathbf{R}(z_n)$ and $\mathbf{T}(z_n)$ are diagonal matrices at depth level z_n with scalar reflectivity $r(x, z_n)$ and transmission $t(x, z_n)$, respectively, along their diagonals.

A.1 Reflectivity update

Calculation of their gradients is required to update the reflectivity and velocity models by a gradient descent scheme. We can derive the gra-

dient for the reflectivity update:

$$\begin{aligned} \nabla \vec{J}_r(z_n) = & \sum_{\xi}^{N_s} \sum_f^{N_{\omega}} \Re \left\{ \left(\underline{\mathbf{W}}_i^-(z_0; z_n, \omega_f)^H \vec{E}_i(z_0, x_{s,\xi}, \omega_f) \right) \circ \right. \\ & \left. \vec{P}_i^+(z_n, x_{s,\xi}, \omega_f)^* \right\} - \sum_{\xi}^{N_s} \sum_f^{N_{\omega}} \Re \left[\left\{ \left(\sum_{m=n+1}^{N_z} \right. \right. \right. \\ & \left. \left. \underline{\mathbf{W}}_i^+(z_m; z_n, \omega_f)^H \mathbf{R}(z_m) \underline{\mathbf{W}}_i^-(z_0; z_m, \omega_f) \right)^H \right. \\ & \left. \left. \vec{E}_i(z_0, x_{s,\xi}, \omega_f) \right\} \circ \vec{P}_{i-1}^-(z_n, x_{s,\xi}, \omega_f)^* \right], \end{aligned} \quad (\text{A.1.4})$$

with

$$\vec{E}_i(z_0, x_{s,\xi}, \omega_f) \equiv \vec{P}_{obs}^-(z_0, x_{s,\xi}, \omega_f) - \vec{P}_{mod,i}^-(z_0, x_{s,\xi}, \omega_f), \quad (\text{A.1.5})$$

where $\vec{E}_i(z_0, x_{s,\xi}, \omega_f)$ represents the residual between the observed and the modeled shot data at the i th roundtrip and H indicates the Hermitian conjugate. Note that the first term of the RHS in equation (A.1.4) means the cross-correlation between the back-propagated upgoing wavefield for the residual and the forward modeled downgoing wavefield. The second term indicates the cross-correlation between the back-propagated downgoing wavefield for the residual and the forward modeled upgoing wavefield. Thus, equation (A.1.4) can be interpreted as the reflectivity image of the residual data. The wavefield perturbation can be obtained from the gradient as follows:

$$\begin{aligned} \Delta \vec{P}_{J,r}^-(z_0, x_{s,\xi}, \omega_f) = & \sum_{n=1}^{N_z} \underline{\mathbf{W}}_i^-(z_0; z_n, \omega_f) \nabla \mathbf{J}_r(z_n) \\ & \vec{P}_i^+(z_n, x_{s,\xi}, \omega_f), \end{aligned} \quad (\text{A.1.6})$$

where $\nabla \mathbf{J}_r(z_n)$ is a square matrix with the gradient $\nabla \vec{J}_r(z_n)$ along its diagonal. A scale factor to adjust the reflectivity update in each iteration is defined by:

$$\alpha_r = \frac{\sum_{\xi}^{N_s} \sum_f^{N_{\omega}} [\Delta \vec{P}_{J,r}^-(z_0, x_{s,\xi}, \omega_f)]^H \vec{E}_i(z_0, x_{s,\xi}, \omega_f)}{\sum_{\xi}^{N_s} \sum_f^{N_{\omega}} \|\Delta \vec{P}_{J,r}^-(z_0, x_{s,\xi}, \omega_f)\|^2}. \quad (\text{A.1.7})$$

Finally, we can update the reflectivity model as follows:

$$r^{(k+1)}(x, z) = r^{(k)}(x, z) + \alpha_r \nabla J_r(x, z), \quad (\text{A.1.8})$$

where $\nabla J_r(x, z)$ are the diagonal elements of $\nabla \mathbf{J}_r(z_n)$. Note that in the above description, unlike the formulation of Berkhout (2014c), the transmission operators have been included in the \mathbf{W} 's, yielding the $\underline{\mathbf{W}}$'s, providing a somewhat more accurate gradient.

A.2 Slowness update

The velocity updating procedure is similar to the reflectivity update. To keep the notation similar, we describe the procedure to update the slowness ($\sigma = 1/c$) model instead of the velocity model (Staal, 2015).

First, we derive a linearized relationship between the propagation operators and the slowness model by introducing their perturbations. The propagation operators are based on the phase-shift operator in the wavenumber domain:

$$\tilde{w}(k_x, \omega) = e^{-jk_z \Delta \tilde{z}}, \quad (\text{A.2.9})$$

with

$$k_z(\sigma) = \sqrt{\omega^2 \sigma^2 - k_x^2}, \quad (\text{A.2.10})$$

$$\Delta \tilde{z} \equiv |z_n - z_m|. \quad (\text{A.2.11})$$

Using their perturbations, we can obtain the following linearized equation:

$$\begin{aligned} \Delta \tilde{w} &= \tilde{w}_{new} - \tilde{w}_{old} \approx \left[\frac{\partial \tilde{w}}{\partial \sigma} \right]_{\sigma_{old}} \Delta \sigma \\ &= -j\omega \left[\frac{k}{k_z} \right]_{\sigma_{old}} \tilde{w}_{old} \Delta \sigma, \end{aligned} \quad (\text{A.2.12})$$

where \tilde{w}_{new} is the operator in an updated slowness model σ_{new} and \tilde{w}_{old} is the operator in the current slowness model σ_{old} . Then, an operator

\mathbf{L} , which is similar to the propagation operators in equation (2.1.10), is defined by:

$$\vec{L}_j(z_m; z_n) = \mathcal{F}_x^{-1} \left[-j\omega\Delta\tilde{z} \left[\frac{k_z^*k}{|k_z|^2 + \epsilon} \right]_{\sigma_{old}} e^{-jk_z\Delta\tilde{z}} e^{-jk_x x_j} \right], \quad (\text{A.2.13})$$

where ϵ is a small stabilization parameter and $*$ indicates complex conjugate. Therefore, we can derive a linearized relationship between the propagation operators and the slowness model:

$$\Delta\mathbf{W}^-(z_{n+1}; z_n) \approx \mathbf{L}^+(z_{n+1}; z_n)\Delta\boldsymbol{\sigma}(z_n), \quad (\text{A.2.14})$$

$$\Delta\mathbf{W}^+(z_n; z_{n+1}) \approx \Delta\boldsymbol{\sigma}(z_n)\mathbf{L}^-(z_n; z_{n+1}), \quad (\text{A.2.15})$$

where $\Delta\boldsymbol{\sigma}(z_n)$ is a diagonal matrix with the slowness updates $\Delta\sigma(x, z_n)$ along its diagonal. An operator $\mathbf{L}^+(z_{n+1}; z_n)$ is defined as $\mathbf{L}^+(z_{n+1}; z_n) = [\mathbf{L}^-(z_n; z_{n+1})]^T$.

We calculate the update direction for the propagation operators:

$$\begin{aligned} \Delta\mathbf{W}^-(z_n; z_{n+1}, \omega_f) &= \sum_{\xi}^{N_s} [\mathbf{V}_i^-(z_0; z_n, \omega_f)]^H \\ &\quad \vec{E}_i(z_0, x_{s,\xi}, \omega_f) [\vec{Q}_i^-(z_{n+1}, x_{s,\xi}, \omega_f)]^H, \end{aligned} \quad (\text{A.2.16})$$

$$\begin{aligned} \Delta\mathbf{W}^+(z_{n+1}; z_n, \omega_f) &= \sum_{\xi}^{N_s} [\mathbf{V}_i^{\cup}(z_0; z_{n+1}, \omega_f)]^H \\ &\quad \vec{E}_i(z_0, x_{s,\xi}, \omega_f) [\vec{Q}_i^+(z_n, x_{s,\xi}, \omega_f)]^H, \end{aligned} \quad (\text{A.2.17})$$

with

$$\begin{aligned} \mathbf{V}_i^-(z_0; z_n, \omega_f) &\equiv \underline{\mathbf{W}}_i^-(z_0; z_n, \omega_f) [\mathbf{I} - \mathbf{R}_i(z_n)], \quad (\text{A.2.18}) \\ \mathbf{V}_i^{\cup}(z_0; z_{n+1}, \omega_f) &\equiv \underline{\mathbf{W}}_i^-(z_0; z_n, \omega_f) \mathbf{R}_i(z_n) \\ &\quad + \sum_{m=n+1}^{N_z} \underline{\mathbf{W}}_i^-(z_0; z_m, \omega_f) \mathbf{R}_i(z_m) \\ &\quad \underline{\mathbf{W}}_i^+(z_m; z_n, \omega_f) [\mathbf{I} + \mathbf{R}_i(z_n)], \end{aligned} \quad (\text{A.2.19})$$

and

$$\vec{Q}_i^+(z_n) = [\mathbf{I} + \mathbf{R}_i(z_n)] \vec{P}_i^+(z_n) - \mathbf{R}_i(z_n) \vec{P}_{i-1}^-(z_n), \quad (\text{A.2.20})$$

$$\vec{Q}_i^-(z_n) = [\mathbf{I} - \mathbf{R}_i(z_n)] \vec{P}_i^-(z_n) + \mathbf{R}_i(z_n) \vec{P}_i^+(z_n), \quad (\text{A.2.21})$$

where i represents the number of roundtrips. Hence, we can calculate the gradient for the slowness update:

$$\begin{aligned} \nabla \vec{J}_\sigma(z_n) = & \text{diag} \left\{ \sum_f^{N_\omega} \Delta \mathbf{W}^-(z_n; z_{n+1}, \omega_f) \right. \\ & \left. [\mathbf{L}^-(z_n; z_{n+1}, \omega_f)]^H \right\} + \text{diag} \left\{ \sum_f^{N_\omega} \right. \\ & \left. [\mathbf{L}^+(z_{n+1}; z_n, \omega_f)]^H \Delta \mathbf{W}^+(z_{n+1}; z_n, \omega_f) \right\}. \end{aligned} \quad (\text{A.2.22})$$

The wavefield perturbation can be obtained from the gradient as follows:

$$\begin{aligned} \Delta \vec{P}_{J,\sigma}^-(z_0, x_{s,\xi}, \omega_f) = & \sum_{n=1}^{N_z} \mathbf{V}_i^-(z_0; z_n, \omega_f) \nabla \mathbf{J}_\sigma(z_n) \\ & \mathbf{L}^-(z_n; z_{n+1}, \omega_f) \vec{Q}_i^-(z_{n+1}, x_{s,\xi}, \omega_f) \\ & + \sum_{n=1}^{N_z} \mathbf{V}_i^\cup(z_0; z_{n+1}, \omega_f) \mathbf{L}^+(z_{n+1}; z_n, \omega_f) \\ & \nabla \mathbf{J}_\sigma(z_n) \vec{Q}_i^+(z_n, x_{s,\xi}, \omega_f), \end{aligned} \quad (\text{A.2.23})$$

where $\nabla \mathbf{J}_\sigma(z_n)$ indicates a square matrix with the gradient $\nabla \vec{J}_\sigma(z_n)$ along its diagonal. On the basis of the wavefield perturbation, a scale factor for the slowness update in each iteration is defined by:

$$\alpha_\sigma = \frac{\sum_\xi^{N_s} \sum_f^{N_\omega} [\Delta \vec{P}_{J,\sigma}^-(z_0, x_{s,\xi}, \omega_f)]^H \vec{E}(z_0, x_{s,\xi}, \omega_f)}{\sum_\xi^{N_s} \sum_f^{N_\omega} \|\Delta \vec{P}_{J,\sigma}^-(z_0, x_{s,\xi}, \omega_f)\|^2}. \quad (\text{A.2.24})$$

Finally, we can update the slowness model:

$$\sigma^{(k+1)}(x, z) = \sigma^{(k)}(x, z) + \alpha_\sigma \nabla J_\sigma(x, z). \quad (\text{A.2.25})$$

Bibliography

- Adamczyk, A., Malinowski, M., and Malehmir, A., 2014, High-resolution near-surface velocity model building using full-waveform inversion - a case study from southwest sweden: *Geophysical Journal International*, **197**, 1693–1704.
- Adamczyk, A., Malinowski, M., and Gorszczyk, A., 2015, Full-waveform inversion of conventional vibroseis data recorded along a regional profile from southeast poland: *Geophysical Journal International*, **203**, 351–365.
- Aki, K., and Richards, P. G., 1980, *Quantative seismology*: W. H. Freeman and Co.
- Al-Ali, M. N., and Verschuur, D. J., 2006, An integrated method for resolving the seismic complex near surface problem: *Geophys. Prosp.*, **54**, no. 6, 739–750.
- Al-Yahya, K. M., 1989, Velocity analysis by iterative profile migraton: *Geophysics*, **54**, no. 6, 718–729.
- Alshuhail, A., and Verschuur, D. J., 2015, Robust anisotropy estimation using joint migration inversion: 85th Ann. Internat. Mtg., Soc. Expl. Geophys., Expanded abstracts, 472–477.

- Alterman, Z., and Karal, F. C., 1968, Propagation of elastic waves in layered media by finite-difference methods: *Bull., Seism. Soc. Am.*, **58**, 367–398.
- Araya-Polo, M., Jennings, J., Adler, A., and Dahlke, T., 2018, Deep learning tomography: *The Leading Edge*, **37**, no. 1, 58–66.
- Avseth, P., Mukerji, T., and Mavko, G., 2005, *Quantitative seismic interpretation*: Cambridge University Press.
- Baysal, E., Kosloff, D. D., and Sherwood, J. W. C., 1983, Reverse time migration: *Geophysics*, **48**, 1514–1524.
- Berkhout, A. J., and Verschuur, D. J., 2011, Full wavefield migration, utilizing surface and internal multiple scattering: 81th Ann. Internat. Mtg., Soc. Expl. Geophys., Expanded abstracts, 3212–3216.
- Berkhout, A. J., 1982, *Seismic migration, imaging of acoustic energy by wave field extrapolation, A: theoretical aspects*: Elsevier (second edition).
- Berkhout, A. J., 1997, Pushing the limits of seismic imaging, part I: prestack migration in terms of double dynamic focusing: *Geophysics*, **62**, no. 3, 937–953.
- Berkhout, A. J., 2012, Combining full wavefield migration and full waveform inversion, a glance into the future of seismic processing: *Geophysics*, **77**, S43–S50.
- Berkhout, A. J., 2014a, Review paper: An outlook on the future of seismic imaging, part I: forward and reverse modelling: *Geophysical Prospecting*, **62**, 911–930.
- 2014b, Review paper: An outlook on the future of seismic imaging, part II: Full wavefield migration: *Geophysical Prospecting*, **62**, 931–949.
- 2014c, Review paper: An outlook on the future of seismic imaging, part III: Joint migration inversion: *Geophysical Prospecting*, **62**, 950–971.

- Biondi, B., and Almomin, A., 2012, Tomographic full waveform inversion (TFWI) by combining full waveform inversion with wave equation velocity analysis: 82nd Ann. Internat. Mtg., Soc. Expl. Geophys., Expanded abstracts, S19.5.
- Biondi, B., and Symes, W., 2004, Angle domain common-image gathers for migration velocity analysis by wavefield continuation imaging: *Geophysics*, **69**, 1283–1298.
- Boore, D. M., 1972, Finite difference methods for seismic wave propagation in heterogeneous materials: *Methods in Computational Physics*, **11**, 1–37.
- Born, M., and Wolf, E., 1980, Principles of optics electromagnetic theory of propagation interference and diffraction of light: 6th Edition, Pergamon Press, Inc.
- Bremmer, H., 1951, The W.K.B. approximation as the first term of a geometric-optical series: *Commun. Pure Appl. Math*, **4**, no. 1, 105–115.
- Chavent, G., and Plessix, R., 1999, An optimal true-amplitude least-squares prestack depth-migration operator: *Geophysics*, **64**, 508–515.
- Chavent, G., Clément, F., and Gómez, S., 1994, Automatic determination of velocities via migration-based travelttime waveform inversion: A synthetic data example: 64th Ann. Internat. Mtg., Soc. Expl. Geophys., Expanded abstracts, 1179–1182.
- Claerbout, J. F., and Doherty, S. M., 1972, Downward continuation of moveout-corrected seismograms: *Geophysics*, **37**, 741–768.
- Claerbout, J. F., 1971, Toward a unified theory of reflector mapping: *Geophysics*, **36**, no. 3, 467–481.
- Clément, F., Chavent, G., and Gómez, S., 2001, Migration-based travelttime waveform inversion of 2-D simple structures: A synthetic example: *Geophysics*, **66**, no. 3, 845–860.

- Cox, M., 1999, Static corrections for seismic reflection surveys: Society of Exploration Geophysicists.
- Dai, W., and Schuster, G. T., 2013, Plane-wave least-squares reverse-time migration: *Geophysics*, **78**, no. 4, S165–S177.
- Davydenko, M., and Verschuur, D. J., 2013, Full wavefield migration without dip limitation - using duplex waves in the imaging with multiples: 75th Ann. Internat. Mtg., Eur. Assoc. Expl Geophys., Expanded abstracts, We P02 09.
- Davydenko, M., and Verschuur, D. J., 2017a, Full-wavefield estimation of angle-dependent reflectivity and migration velocity: 87th Ann. Internat. Mtg., Soc. Expl. Geophys., Expanded abstracts, 5631–5635.
- 2017b, Full-wavefield migration: using surface and internal multiples in imaging: *Geophys. Prosp.*, **65**, 7–21.
- Davydenko, M., Verschuur, D. J., and Berkhout, A. J., 2014, Omnidirectional extension of full wavefield migration: 76th Ann. Internat. Mtg., Eur. Assoc. Expl Geophys., Expanded abstracts, Tu G103 06.
- de Bruin, C. G. M., Wapenaar, C. P. A., and Berkhout, A. J., 1990, Angle-dependent reflectivity by means of prestack migration: *Geophysics*, **55**, no. 9, 1223–1234.
- Dong, S., Cai, J., Guo, M., Suh, S., Zhang, Z., Wang, B., and Li, Z., 2012, Least-squares reverse time migration: Towards true amplitude imaging and improving the resolution: 82nd Ann. Internat. Mtg., Soc. Expl. Geophys., Expanded abstracts, 1–5.
- Duan, Y., Guitton, A., and Sava, P., 2017, Elastic least-squares reverse time migration: *Geophysics*, **82**, no. 4, S315–S325.
- El-Marhfoul, B., Al-Momin, A., and Verschuur, D. J., 2009, Practical application of CFP technology to resolve complex near surface problems and to estimate a velocity-depth model: 71th Ann. Internat. Mtg., Eur. Ass. of Geosc. and Eng., Expanded abstracts, T013.

- Ernst, F., 2013, Modal elastic inversion: 75th Ann. Internat. Mtg., Eur. Ass. of Geosc. and Eng., Expanded abstracts, Th 01 01.
- Esser, E., Guasch, L., van Leeuwen, T., Aravkin, A. Y., and Herrmann, F. J., 2015, Total variation regularization strategies in full waveform inversion for improving robustness to noise, limited data and poor initializations: Technical Report, **TR-EOAS-2015-5**.
- Esser, E., Guasch, L., van Leeuwen, T., Aravkin, A. Y., and Herrmann, F. J., 2018, Total-variation regularization strategies in full-waveform inversion: *SIAM J. Imaging Sciences*, **11**, no. 1, 376–406.
- Feng, Z., and Schuster, G. T., 2017, Elastic least-squares reverse time migration: *Geophysics*, **82**, no. 2, S143–S155.
- Gardner, G. H. F., Gardner, L. W., and Gregory, A. R., 1974, Formation velocity and density - the diagnostic basis for stratigraphic traps: *Geophysics*, **39**, 770–780.
- Gazdag, J., 1978, Wave equation migration with the phase-shift method: *Geophysics*, **43**, no. 7, 1342–1351.
- Goldstein, T., and Osher, S., 2009, The split bregman method for L1-regularized problems: *SIAM J. Imaging Sciences*, **2**, 323–343.
- Gray, S. H., Etgen, J., Dellinger, J., and Whitmore, D., 2001, Seismic migration problems and solutions: *Geophysics*, **66**, no. 5, 1622–1640.
- Haffinger, P. R., and Verschuur, D. J., 2010, Estimation and application of full-waveform redatuming operators: 72nd Ann. Internat. Mtg., Eur. Ass. of Geosc. and Eng., Expanded abstracts, M043.
- Hagedoorn, J. G., 1954, A process of seismic reflection interpretation: *Geophys. Prosp.*, **2**, no. 2, 85–127.
- Hindriks, C. O. H., and Verschuur, D. J., 2001, CFP approach to the complex near surface: 71st Ann. Internat. Mtg., Soc. Expl. Geophys., Expanded abstracts, 1863 – 1866.

- Irabor, K., and Warner, M., 2016, Reflection FWI: 86th Ann. Internat. Mtg., Soc. Expl. Geophys., Expanded abstracts, 1136–1140.
- Jervis, M., Sen, M. K., and Stoffa, P. L., 1996, Prestack migration velocity estimation using nonlinear methods: *Geophysics*, **61**, no. 1, 138–150.
- Ji, S., Huang, T., Fu, K., and Li, Z., 2011, Dirty salt velocity inversion: The road to a clearer subsalt image: *Geophysics*, **76**, no. 5, WB169–WB174.
- Jia, X., and Wu, R., 2009, Superwide-angle one-way wave propagator and its application in imaging steep salt flanks: *Geophysics*, **74**, no. 4, S75–S83.
- Julian, B. R., and Gubbins, D., 1977, Three dimensional seismic ray tracing: *Journal of Geophysics*, **43**, 95–119.
- Kaplan, S. T., Routh, P. S., and Sacchi, M. D., 2010, Derivation of forward and adjoint operators for least-squares shot-profile split-step migration: *Geophysics*, **75**, no. 6, S225–S235.
- Kelamis, P. G., Erickson, K. E., Verschuur, D. J., and Berkhout, A. J., 2002, Velocity-independent redatuming: a new approach to the near-surface problem in land seismic data processing: *The Leading Edge*, **21**, no. 8, 730–735.
- Keys, R. G., and Weglein, A. B., 1983, Generalized linear inversion and the first born theory for acoustic media: *Journal of Mathematical Physics*, **24**, no. 6, 1444–1449.
- Kinneying, N. K., Budejicky, V., Wapenaar, C. P. A., and Berkhout, A. J., 1989, Efficient 2D and 3D shot record redatuming: *Geophys. Prosp.*, **37**, no. 5, 493–530.
- Kosloff, D., and Baysal, E., 1982, Forward modeling by a Fourier method: *Geophysics*, **47**, 1402–1412.

- Kosloff, D., Kessler, D., Filho, A. Q., Tessmer, E., Behle, A., and Strahilevitz, R., 1990, Solution of the equations of dynamic elasticity by a Chebychev spectral method: *Geophysics*, **55**, 464–473.
- Kühl, H., and Sacchi, M. D., 2003, Least-squares wave-equation migration for AVP/AVA inversion: *Geophysics*, **68**, no. 1, 262–273.
- LeCun, Y., Bengio, Y., and Hinton, G., 2015, Deep learning: *Nature*, **521**, 436–444.
- Liu, Z., and Bleistein, N., 1995, Migration velocity analysis: theory and an iterative algorithm: *Geophysics*, **60**, 142–153.
- Lysmer, J., and Drake, L. A., 1972, A finite element method for seismology: *Methods in Computational Physics*, **11**, 181–216.
- Maciel, J. S., Costa, J. C., and Verschuur, D. J., 2015, Enhancing resolution in imaging-based velocity estimation using morphological operators: 85th Ann. Internat. Mtg., Soc. Expl. Geophys., Expanded abstracts, 5228–5232.
- MacKay, S., and Abma, R., 1992, Imaging and velocity estimation with depth-focusing analysis: *Geophysics*, **57**, 1608–1622.
- Mahrooqi, S., Rawahi, S., Yarubi, S., Abri, S., Yahyai, A., Jahdhami, M., Hunt, K., and Shorter, J., 2012, Land seismic low frequencies: acquisition, processing and full wave inversion of 1.5 - 86 hz: 82th Ann. Internat. Mtg., Soc. Expl. Geophys., Expanded abstracts, 1–5.
- Marmalyevskyy, N., Roganov, Y., Gornyak, Z., Kostyukevych, A., and Mershchiy, V., 2005, Migration of duplex waves: 75th Ann. Internat. Mtg., Soc. Expl. Geophys., Expanded abstracts, 2025–2028.
- Masaya, S., and Verschuur, D. J., 2016a, Full wavefield imaging of the near surface by joint migration inversion: 78th Ann. Internat. Mtg., Eur. Ass. of Geosc. and Eng., Expanded abstracts, We SBT4 01.
- 2016b, Joint migration inversion based on reflectivity-constrained velocity estimation: 86th Ann. Internat. Mtg., Soc. Expl. Geophys., Expanded abstracts, 5379–5383.

- Masaya, S., and Verschuur, D. J., 2017a, Near-surface imaging by enhancing the effect of internal multiples: 79th Ann. Internat. Mtg., Eur. Ass. of Geosc. and Eng., Expanded abstracts, Tu C3 09.
- 2017b, Seismic modeling refracted and reflected waves including internal multiples by one-way propagators: 87th Ann. Internat. Mtg., Soc. Expl. Geophys., Expanded abstracts, 4138–4142.
- Masaya, S., and Verschuur, D. J., 2018a, Iterative reflectivity-constrained velocity estimation for seismic imaging: *Geophysical Journal International*, **214**, 1–13.
- 2018b, Surface-consistent seismic data amplitude correction via learning from synthetic models based on waveform modeling: 80th Ann. Internat. Mtg., Eur. Ass. of Geosc. and Eng., Expanded abstracts, We E 11.
- Mathewson, J. C., Evans, D., Leone, C., Leathard, M., Dangerfield, J., and Tinning, S. A., 2012, Improved imaging and resolution of overburden heterogeneity by combining amplitude inversion with tomography: 82th Ann. Internat. Mtg., Soc. Expl. Geophys., Expanded abstracts, 1–5.
- Maurer, H., Greenhalgh, S. A., Manukyan, ., Marelli, S., and Green, A. G., 2012, Receiver-coupling effects in seismic waveform inversions: *Geophysics*, **77**, no. 1, V19–V30.
- McMechan, G. A., 1983, Migration by extrapolation of time-dependent boundary values: *Geophys. Prosp.*, **31**, 413–420.
- Mulder, W. A., and Plessix, R.-E., 2004, A comparison between one-way and two-way wave-equation migration: *Geophysics*, **69**, no. 6, 1491–1504.
- Nemeth, T., Wu, C., and Schuster, G. T., 1999, Least-squares migration of incomplete reflection data: *Geophysics*, **64**, no. 1, 208–221.
- Plessix, R.-E., De Roeck, Y.-H., and Chavent, G., 1999, Waveform inversion of reflection seismic data for kinematic parameters by local optimization: *SIAM J. Sci. Comput.*, **20**, 1033–1052.

- Plessix, R.-E., Baeten, G., de Maag, J. W., Klaassen, M., Rujie, Z., and Zhifei, T., 2010, Application of acoustic full waveform inversion to a low-frequency large-offset land data set: 80th Ann. Internat. Mtg., Soc. Expl. Geophys., Expanded abstracts, 930–934.
- Qiu, L., Zou, K., Valenciano, A., and Chemingui, N., 2016, Full waveform inversion with steerable variation regularization: 86th Ann. Internat. Mtg., Soc. Expl. Geophys., Expanded abstracts, 1174–1178.
- Ravaut, C., Operto, S., Imbrota, L., Herrero, A., and Dell'Aversana, P., 2004, Multiscale imaging of complex structures from multifold wide-aperture seismic data by frequency-domain full-waveform tomography: application to a thrust belt: *Geophysical Journal International*, **159**, 1032–1056.
- Reust, D. K., Force, S., Johnston, O. A., Giles, J. A., and Ballinger, S., 2015, Very low frequency seismic source: 85th Ann. Internat. Mtg., Soc. Expl. Geophys., Expanded abstracts, 221–225.
- Routh, P., Neelamani, R., Lu, R., Lazaratos, S., Braaksma, H., Hughes, S., Saltzer, R., Stewart, J., Naidu, K., Averill, H., Gottumukkula, V., Homonko, P., Reilly, J., and Leslie, D., 2017, Impact of high-resolution FWI in the Western Black Sea: Revealing overburden and reservoir complexity: *The Leading Edge*, **36**, no. 1, 60–66.
- Sacchi, M. D., Ulrych, T. J., and Walker, C. J., 1998, Interpolation and extrapolation using a high-resolution discrete fourier transform: *IEEE Trans. Signal Processing*, **46**, 31–38.
- Sava, P., and Biondi, B., 2004, Wave equation migration velocity analysis. I. theory: *Geophys. Prosp.*, **52**, 593–606.
- Schneider, W. A., 1978, Integral formulation for migration in two and three dimensions: *Geophysics*, **43**, no. 1, 49–76.
- Sedova, A., Royle, G. T., Hermant, O., Retailleau, M., and Lambaré, G., 2017, High-resolution land full waveform inversion - a case study on a data set from the sultanate of Oman: 79th Ann. Internat. Mtg., Eur. Ass. of Expl. Geophys., Expanded abstracts, We A3 07.

- Sheriff, R. E., and Geldart, L. P., 1995, *Exploration seismology*: Cambridge University Press, 2nd edition.
- Shtivelman, V., and Canning, A., 1988, Datum correction by wave equation extrapolation: *Geophysics*, **53**, no. 10, 1311–1322.
- Smith, W. D., 1975, The application of finite element analysis to body wave propagation problems: *Geophys. J. Roy. Astr. Soc.*, **42**, 747–768.
- Smithyman, B. R., and Clowes, R. M., 2013, Waveform tomography in 2.5D: Parameterization for crooked-line acquisition geometry: *Journal of Geophysical Research*, **118**, 2119–2135.
- Soubaras, R., 2010, Deghosting by joint deconvolution of a migration and a mirror migration: 80th Ann. Internat. Mtg., Soc. Expl. Geophys., Expanded abstracts, 3406–3410.
- Staal, X. R., and Verschuur, D. J., 2012, Velocity estimation using internal multiples: 82nd Ann. Internat. Mtg., Soc. Expl. Geophys., Expanded abstracts, 1–5.
- Staal, X. R., and Verschuur, D. J., 2013, Joint migration inversion, imaging including all multiples with automatic velocity update: 75th Ann. Internat. Mtg., Eur. Ass. of Geosc. and Eng., Expanded abstracts, Tu-02-16, 4pp.
- Staal, X. R., Verschuur, D. J., and Berkhout, A. J., 2014, Robust velocity estimation by Joint Migration Inversion: 76th Ann. Internat. Mtg., Eur. Ass. of Geosc. and Eng., Expanded abstracts, 4290–4295.
- Staal, X. R., 2015, Combined imaging and velocity estimation by Joint Migration Inversion: Ph.D. thesis, Delft University of Technology.
- Stolt, R. H., 1978, Migration by Fourier transform: *Geophysics*, **43**, no. 1, 23–48.
- Sun, D., Jiao, K., Cheng, X., and Vigh, D., 2016, Reflection based waveform inversion: 86th Ann. Internat. Mtg., Soc. Expl. Geophys., Expanded abstracts, 1151–1156.

- Sun, D., Jiao, K., Cheng, X., Xu, Z., Zhang, L., and Vigh, D., 2017, Born modeling based adjustive reflection full waveform inversion: 87th Ann. Internat. Mtg., Soc. Expl. Geophys., Expanded abstracts, 1460–1465.
- Tal-Ezer, H., Carcione, J. M., and Kosloff, D., 1990, An accurate and efficient scheme for wave propagation in linear viscoelastic media: *Geophysics*, **55**, 1366–1379.
- Taner, M. T., and Koehler, F., 1969, Velocity spectra - digital computer derivation applications of velocity functions: *Geophysics*, **34**, no. 6, 859–881.
- Taner, M. T., and Koehler, F., 1981, Surface consistent corrections: *Geophysics*, **46**, no. 1, 17–22.
- Tarantola, A., 1984, Inversion of seismic reflection data in the acoustic approximation: *Geophysics*, **49**, 1259–1266.
- Thorbecke, J. W., 1997, Common focus point technology: Ph.D. thesis, Delft University of Technology.
- van Groenestijn, G. C. A., and Verschuur, D. J., 2009, Estimating primaries by sparse inversion and application to near-offset data reconstruction: *Geophysics*, **74**, A23–A28.
- van Leeuwen, T., and Herrmann, F. J., 2013, Mitigating local minima in full-waveform inversion by expanding the search space: *Geophysical Journal International*, **195**, 661–667.
- van Leeuwen, T., and Herrmann, F. J., 2016, A penalty method for PDE-constrained optimization in inverse problems: *Inverse Problems*, **32**, 1–26.
- van Vossen, R., Curtis, A., Laake, A., and Trampert, J., 2006, Surface-consistent deconvolution using reciprocity and waveform inversion: *Geophysics*, **71**, no. 2, V19–V30.

- Verschuur, D. J., and El-Marhfoul, B., 2005, Estimation of complex near surface focusing operators by global optimization: 67th Ann. Internat. Mtg., Eur. Ass. of Geosc. and Eng., Expanded abstracts, A035.
- Verschuur, D. J., Staal, X. R., and Berkhout, A. J., 2016, Joint migration inversion: Simultaneous determination of velocity fields and depth images using all orders of scattering: *The Leading Edge*, **35**, no. 12, 1037–1046.
- Virieux, J., and Operto, S., 2009, An overview of full-waveform inversion in exploration geophysics: *Geophysics*, **74**, WCC127–WCC152.
- Virieux, J., 1986, P-SV wave propagation in heterogeneous media: Velocity-stress finite-difference method: *Geophysics*, **51**, 888–901.
- Vrolijk, J. W., Haffinger, P. R., and Verschuur, D. J., 2012, Multi-datum based estimation of near-surface full-waveform redatuming operators: *J. of Appl. Geoph.*, **82**, 30–45.
- Wang, P., and Peng, C., 2012, Premigration deghosting for marine towed streamer data using a bootstrap approach: 82nd Ann. Internat. Mtg., Soc. Expl. Geophys., Expanded abstracts, 1–5.
- Wapenaar, C. P. A., and Berkhout, A. J., 1989, Elastic wave field extrapolation: redatuming of single- and multi-component seismic data: Elsevier Science Publ. Co., Inc.
- Warner, M., and Guasch, L., 2016, Adaptive waveform inversion: Theory: *Geophysics*, **81**, R429–R445.
- Whitmore, N. D., 1983, Iterative depth migration by backward time propagation: 53rd Ann. Internat. Mtg., Soc. Expl. Geophys., Expanded abstracts.
- Williamson, P. R., and Pratt, R. G., 1995, A critical review of acoustic wave modeling procedures in 2.5 dimensions: *Geophysics*, **60**, no. 2, 591–595.

- Wong, M., Biondi, B. L., and Ronen, S., 2015, Imaging with primaries and free-surface multiples by joint least-squares reverse time migration: *Geophysics*, **80**, no. 6, U9–U17.
- Yilmaz, O., 2001, *Seismic data analysis*: Society of Exploration Geophysicists.
- Yoon, K., and Marfurt, K., 2004, Challenges in reverse-time migration: 74th Ann. Internat. Mtg., Soc. Expl. Geophys., Expanded abstracts, 1057–1060.
- Zhang, J., and Toksöz, M. N., 1998, Nonlinear refraction traveltime tomography: *Geophysics*, **63**, 1726–1737.
- Zhu, X., Sixta, D. P., and Angstman, B. G., 1992, Tomostatics: turning-ray tomography + static corrections: *The Leading Edge*, **11**, 15–23.

Summary

Seismic imaging is a significant technology to provide the image of the subsurface in several fields such as hydrocarbon exploration/production and civil engineering. A fundamental problem in seismic imaging is that both the depth reflectivity and velocity distribution of the subsurface have to be predicted by only seismic events observed at the surface, and it still remains a challenging research topic. Joint migration inversion (JMI) is one of the seismic waveform imaging algorithms that were recently proposed. JMI is capable of simultaneously estimating velocity and reflectivity models of the subsurface by exploiting reflected waves including internal multiples. The seismic modeling algorithm in the JMI process is a method termed full wavefield modeling (FWMod), which is a one-way propagator-based reflection modeling algorithm, including higher-order scattering and transmission effects.

In this thesis, two directions to improve the accuracy of seismic imaging based on JMI are discussed. On one hand, an extension of FWMod is proposed to correctly deal with not only reflected waves but refracted/diving waves via one-way propagators in the horizontal direction, and this method is extended to a new JMI algorithm. On the other hand, we assume that only reflected waves including internal multiples are utilized in the imaging based on JMI and present two novel methods for the inversion and pre-processing: 1) iterative reflectivity-constrained velocity estimation, 2) surface amplitude correction via learning from synthetic models for land seismic data.

The reflectivity-constrained velocity estimation is employed to improve

the accuracy of the estimated velocity by exploiting the estimated reflectivity in the JMI process. The surface amplitude correction process is introduced to mitigate the influence of the amplitude variations caused by source/receiver response sensitivities and the difference of the features between observed land seismic data and the simulated data by the used imaging scheme.

The numerical and field data examples for both land and marine cases demonstrate that the proposed approach is capable of effectively estimating reflectivity and velocity model, even though the low frequency components of the observed data are absent.

Samenvatting

De seismische methode is een belangrijke technologie die gebruikt kan worden om een beeld van de ondergrond te verkrijgen. Deze methode wordt toegepast in verschillende velden zoals exploratie en productie binnen de gas/olieindustrie en civiele technieken. Een fundamenteel probleem in het seismische afbeelden (ook wel “migratie” genoemd) is dat de distributie van zowel reflectiviteit als propagatiesnelheids in de ondergrond geschat moeten worden op basis van seismische meting aan het oppervlak. Dit blijft een uitdagend onderzoeksonderwerp. De zogenaamde Joint Migration Inversion (JMI), oftewel gecombineerde migratie en inversie, is één van de seismische algoritmes die zijn voorgesteld om het bovengenoemde probleem op te lossen. JMI is in staat om de migratiesnelheid en de reflectiviteit van de ondergrond tegelijkertijd te schatten door gebruik te maken van gereflecteerde golfvelden, inclusief de zogenaamde interne multiples. De seismische modellering in het JMI algoritme is gebaseerd op een methode genaamd full wavefield modeling (FWMod). Dat is een algoritme gebaseerd op één-weg propagatie van gereflecteerde energie, maar door recursieve toepassing worden de hogere orde scattering en transmissieeffecten meegenomen.

In deze thesis worden twee methodes besproken om de nauwkeurigheid van seismische afbeelden op basis van JMI te verbeteren. Ten eerste is een uitbreiding van FWMod voorgesteld om niet alleen gereflecteerde maar ook gerefracteerde golven op de juiste manier te behandelen. Dit wordt mogelijk gemaakt door één-weg propagatie operatoren in de horizontale richting te introduceren. Bovendien is deze methode ook uit-

gebreed naar een nieuw JMI algoritme. Ten tweede, presenteren we twee nieuwe methodes voor de inversie en pre-processing van de seismische metingen, ervan uitgaande dat alleen gereflecteerde golven, inclusief interne multiples, worden gebruikt in het JMI afbeeldingsproces: 1) iteratieve snelheid schatting met de reflectiviteit als randvoorwaarde, 2) oppervlakte amplitudecorrectie door het kalibreren en aanleren via synthetische modellen voor land seismische data. Door de reflectiviteit als randvoorwaarden te gebruiken wordt de schatting van de propagatiesnelheden nauwkeuriger en consistent met de schatting van de reflectiviteit zelf. Het oppervlakte amplitudecorrectie proces is geïntroduceerd om het effect van amplitudevariëaties te onderdrukken. Deze amplitudevariëaties worden veroorzaakt door de koppelingen verschillen met betrekking tot bronnen en ontvangers en het verschil tussen de karakteristieken van de gemeten seismische data en de data die gesimuleerd wordt door het gebruikte afbeeldingsschema.

De gepresenteerde numerieke en velddata voorbeelden, zowel voor het geval van land als marine, laten zien dat de voorgestelde methode in staat is om op een effectieve wijze de reflectiviteit en het snelheidsmodel te schatten zelfs wanneer de lage frequentiecomponenten niet beschikbaar zijn in de gemeten data.

Acknowledgments

I am very grateful to many people who have influenced and helped me for this study.

First and foremost, I am grateful to my supervisor Dr. Eric Verschuur. I could smoothly conduct this study for three years, owing to his kind guidance. His constructive feedbacks for my ideas were very effective to enhance the quality and progress of my study. Moreover, I learned how to improve my manuscripts via his detailed review for my written papers, conference proceedings, book chapters and thesis. I am very grateful for them.

I would like to thank Prof. Nico de Jong, Dr. Martin Verweij and Dr. Koen van Dongen in the group of Acoustic Wavefield Imaging for providing the opportunities to touch medical imaging via AWI seminars. Additionally, I would like to thank Dr. Gerrit Blacquièrè and Dr. Femke Vossepoel for the intriguing presentations in the Delphi sponsor meeting.

I am grateful to my committee members for reviewing my thesis. Especially, Prof. Andrew Curtis of the University of Edinburgh and Dr. Rob Hegge of Aramco Overseas Company B.V. provided many helpful comments to improve my thesis. I really appreciate their review.

I would like to express my thanks to all the colleagues in the Delphi group. Firstly, thanks 4 colleagues for sharing the same office with me. Thanks Abdulrahman Alshuhail for lots of technical and nontechnical helps, especially in my early days of PhD. Thanks Shan Qu for sharing the office for around 3 years. I hope her neck pain will get well. Thanks

for Bouchaib El Marhfoul for the translation of my summary in Dutch. Thanks Halah Alasmri for many interesting talks in my last half year of PhD. Many thanks are also due to other current and past colleagues of the group - Mikhail Davydenko, Aayush Garg, Hussain Hammad, Junhai Cao, Apostolos Kontakis, Aparajita Nath, Dong Zhang, Gabriel Lopez, Nick Luiken, Runhai Feng, Siddarth Sharma, Sixue Wu, Matteo Caporal, Jan-Willem Vrolijk, Shotaro Nakayama, Özkan Sertlek, Amarjeet Kumar. I would also like to thank the guys in Aramco Overseas Company B.V. which is close to our group: Dr. Yimin Sun, Dr. Hannes Kutscha, Dr. Jewoo Woo and Dr. Mikhail Belonosov.

I would like to thank our previous secretary Margaret van Fessem and current secretary Angela van der Sande for arranging our business trips and organizing outdoor events. I am also grateful to Edo Bergsma and Henry den Bok for the help to construct optimum IT environment.

I am also deeply grateful to Dr. Yohei Nishitsuji, who also obtained a PhD at TU Delft last year. We often discussed our country and the prospects of the oil industry.

I would like to acknowledge my former supervisor in Kyoto university Prof. Yasuaki Kishimoto. Although I had engaged in the job that was not R&D for 7 years since my graduation of Kyoto university, I did not have any anxiety for starting this PhD study, owing to my 'savings' obtained from his supervision.

I am grateful to INPEX for funding my PhD study. I would like to thank its senior executive vice president Mr. Masaharu Sano for signing my contract of this study. Moreover, I thank Mr. Kuniaki Takayama, Mr. Katsumi Nakasuka, Dr. Tomohide Ishiyama and Dr. Ryohei Tada for approving and/or supporting my starting this study.

I would like to thank the sponsors of the Delphi consortium for their support for my research. Especially, I would like to acknowledge Saudi Aramco for providing a land field dataset and a synthetic model, and I am grateful to Dr. Mustafa N. Al-Ali of Saudi Aramco for initial pre-processing and providing the velocity for the field data. I also appreciate Statoil for providing a North sea field dataset. These datasets and model were very helpful to investigate the validity of our proposed methods

and give me new ideas.

Finally, I would like to record my deep gratitude to my parents for their endless support.

Shogo Masaya
March 19th, 2018

Curriculum Vitae

Shogo Masaya was born in Tokyo, Japan. He obtained a Master in plasma physics from Kyoto University in 2008, and he worked in INPEX as a geophysicist from 2008 to 2015. Then, he joined Delft University of Technology and Delphi consortium as a PhD candidate in July 2015.

Recent publications

■ Peer-reviewed journal papers

- **S. Masaya** and D.J. Verschuur, “Surface amplitude correction framework based on learning from synthetic subsurface models”, *Geophysics*, submitted.
- **S. Masaya** and D.J. Verschuur, “Iterative reflectivity-constrained velocity estimation for seismic imaging”, *Geophysical Journal International*, 214, 1-13, 2018.
- **S. Masaya**, “Audio signal separation through complex tensor factorization: utilizing modulation frequency and phase information”, *Signal Processing (Elsevier)*, 142C, 137-148, 2018.
- R. Kamei, T. Miyoshi, G. Pratt, M. Takanashi and **S. Masaya**, “Application of waveform tomography to a crooked-line 2D land seismic data set”, *Geophysics*, 80(5), B115-B129, 2015.

■ Peer-reviewed conference papers

- **S. Masaya** and D. J. Verschuur, “Surface-consistent seismic data amplitude correction via learning from synthetic models based on waveform modeling”, 80th Conference and Exhibition, EAGE, Extended Abstracts, We E 11, 2018.
- **S. Masaya** and D. J. Verschuur, “Seismic modeling refracted and reflected waves including internal multiples by one-way propagators”, 87th Annual International Meeting, SEG, Expanded Abstracts, 4138-4142, 2017.
- **S. Masaya** and D. J. Verschuur, “Near-surface imaging by enhancing the effect of internal multiples”, 79th Conference and Exhibition, EAGE, Extended Abstracts, Tu C3 09, 2017.
- **S. Masaya** and D. J. Verschuur, “Joint migration inversion based on reflectivity-constrained velocity estimation”, 86th Annual International Meeting, SEG, Expanded Abstracts, 5379-5383, 2016.
- **S. Masaya** and D. J. Verschuur, “Full wavefield imaging of the near surface by Joint Migration Inversion”, 78th Conference and Exhibition, EAGE, Extended Abstracts, We SBT4 01, 2016.

■ Book chapters

- **S. Masaya** and D.J. Verschuur, “Reflectivity-Constrained JMI: Iterative reflectivity-constrained velocity estimation”, Delphi Multiple Removal and Structural Imaging, Volume XXIX, Chapter 9, pages 1-29, 2018.
- **S. Masaya** and D.J. Verschuur, “Horizontal wavefield migration: Towards incorporating refracted/diving waves in JMI”, Delphi Acquisition and Preprocessing, Volume XXII, Chapter 13, pages 1-20, 2018.

- **S. Masaya** and D.J. Verschuur, “Land JMI without low frequency components via learning from synthetic models”, *Delphi Acquisition and Preprocessing*, Volume XXII, Chapter 14, pages 1-22, 2018.
- **S. Masaya** and D.J. Verschuur, “Constrained JMI: reflectivity-constrained velocity estimation”, *Delphi Multiple Removal and Structural Imaging*, Volume XXVIII, ISBN978-90-73817-68-5, Chapter 14, pages 1-24, 2017.
- **S. Masaya** and D.J. Verschuur, “Enhancing the effect of internal multiples for near-surface imaging with JMI”, *Delphi Acquisition and Preprocessing*, Volume XXI, ISBN978-90-73817-66-1, Chapter 11, pages 1-17, 2017.
- **S. Masaya** and D.J. Verschuur, “Towards estimating refracted waves in JMI”, *Delphi Acquisition and Preprocessing*, Volume XXI, ISBN978-90-73817-66-1, Chapter 12, pages 1-17, 2017.
- **S. Masaya** and D. J. Verschuur, “JMI based on reflectivity-constrained velocity estimation”, *Delphi Multiple Removal and Structural Imaging*, Volume XXVII, ISBN978-90-73817-64-7, Chapter 11, pages 173-189, 2016.
- **S. Masaya** and D. J. Verschuur, “Full wavefield imaging of the near surface by JMI”, *Delphi Acquisition and Preprocessing*, Volume XX, ISBN978-90-73817-63-0, Chapter 8, pages 113-131, 2016.